

Meshfree Simulation of Problems in Soil Mechanics

Laboratory Tests · Shear Bands · Punching · Cone Penetration ·
Turbulence in Granular Solids · Ptygmatic Folds

Iman Bathaeian, MSc

Innsbruck, August 2018

Dissertation

eingereicht an der Leopold-Franzens-Universität Innsbruck, Fakultät für
Technische Wissenschaften zur Erlangung des akademischen Grades

Doktor der Technischen Wissenschaften

Erster Beurteiler:

em. o. Univ.-Prof. Dipl.-Ing. Dr. Dimitrios Kolymbas,
Universität Innsbruck, Institut für Infrastruktur,
Arbeitsbereich für Geotechnik und Tunnelbau

Zweiter Beurteiler:

Univ.-Prof. Dr.-Ing. habil. Christos Vrettos, Technische
Universität Kaiserslautern, Fachgebiet Bodenmechanik und
Grundbau

Hauptbetreuer: em. o. Univ.-Prof. Dipl.-Ing. Dr. Dimitrios Kolymbas,
Universität Innsbruck, Institut für Infrastruktur,
Arbeitsbereich für Geotechnik und Tunnelbau

Zweiter Betreuer: ao. Univ.-Prof. Dipl.-Ing. Dr. Wolfgang Fellin, Universität
Innsbruck, Institut für Infrastruktur, Arbeitsbereich für
Geotechnik und Tunnelbau

Acknowledgment

In March 2014, as I arrived in Innsbruck and met Professor Kolymbas, a new chapter began in my life. Though it was like a new, fresh starting point, I felt at home among my nice colleagues at University of Innsbruck. My new personal, social and scientific life in this city and the academic cooperation in a friendly and creative team have given me golden opportunities to learn and grow, which the present dissertation can only barely represent the extent of my priceless experiences in the past four years. This dissertation is a small contribution to the remarkable achievements, made by the scientific members of the unit of Geotechnical and Tunnel Engineering, University of Innsbruck over two decades of research and academic work under the supervision of Professor Kolymbas.

First and foremost, I wish to thank my eminent advisor, Professor Dimitrios Kolymbas, for his impartial decision on accepting my supervision in his last years stay at this University, and also for his patience in teaching me the fundamental parts of my work (particularly the concepts of soil mechanics, material modeling, continuum mechanics), and last but not least, his rational and straightforward scientific manner. I could benefit greatly as a researcher and as a person from his academic and emotional support through the rough road to finish this dissertation.

Moreover, I wish to thank my second advisor, Professor Wolfgang Fellin, for his supportive manner and readiness to help, as well as his interesting and worthwhile lectures on non-linear material models, ice, snow and avalanche mechanics and the memorable summer school, in which I learned a lot. His lectures on some seminal topics laid the preliminaries of this work.

I truthfully thank Professor Christos Vrettos for accepting to be the member of the committee of my rigorosum, the valuable suggestions and his generous hospitality during my visits in Kaiserslautern.

I would like to express my special thanks to Barbara Schneider- Muntau for always being there on the hard days and providing me with emotional and scientific support throughout these past four years. Her open-minded and flexible manner towards solving problems always promoted space for mutual and comfortable discussions.

I would also like to thank my former and present colleagues at the division of geotechnical and tunnel engineering, they were all sources of love, passion and energy. Gertraud Medicus' encouraging support has been always amazing, particularly in terms of the

mechanical behavior of material models. I thank Sarah-Jane Loretz-Theodorine for patiently taking care of administrative procedures, which were of great complexity in my case as a foreign student. I would also like to thank Fabian Schranz and Matthias Rauter, with whom I shared the office and benefited from their academic experiences and accompaniment which helped me to speak German more confidently and fluently. I also feel compelled to especially thank Chen Chien-Hsun and Iliana Polymerou, the pioneers of the Soft PARTicle Code (SPARC), whose efforts paved the way for completion of my dissertation. I express my gratitude towards, Professor Robert Hofmann, Manuel Bode, Anastasia Blioumi, Mrs. Neuwirt, Claudia Thurnwalder, Stefan Tilg and Franz Berger for their assistance and warm camaraderie.

I praise the help and teachings of Peter Gamnitzer, Jörg Kuhnert and Isabel Michel, from which I learned a lot throughout these years. Thanks to Daniel Aubram, who has generously been providing me with data of his experiments.

Special thanks to my friends here in Innsbruck and back home in Tehran: Hildegard Berger, Ferdinand Pospischil, Martin Wurzer, Werner Kollnig, Tobias Cordes, Mehdi Bathaeian, Mohammad Zarei, Saeedeh Taheri, Meysam Miresghi, Camelia Shahabi and Farshid Soltani for reminding me my strengths at critical points and helping me to stay confidently at times of challenge. I do also acknowledge the financial support from Austrian Science Fund (FWF): I 547-N13.

I finish my words of acknowledgment with expressing my gratitude to my parents, Mohammad Bathaeian and Fatemeh Yektaie, my significant other, Helena Rußegger, and my brother Amin, in whom the source of my motivation resides. The unconditional love of my parents made me who I am now and I could not be any more grateful for what they have gone through for me in all these years. The heart-warming presence of Helena was the last piece of the puzzle of my dissertation which fulfilled it.

Kurzfassung

Numerische Methoden beruhen meist auf netzbasierten Verfahren, sogenannten Finiten Elementen (FE). Neben experimentellen und theoretischen Verfahren spielen diese seit langem eine wichtige Rolle in der Analyse von Problemen der Mechanik. Eine Schwachstelle der klassischen netzbasierten Methoden liegt in der eingeschränkten Möglichkeit große Verformungen zu simulieren. Besonders im Bereich der Bodenmechanik treten bei vielen Fragestellungen große Verformungen auf. Im Gegensatz zu den netzbasierten Verfahren sind netzfreie Verfahren nicht auf feste Nachbarschaften zwischen den materiellen Punkten angewiesen und sollten sich daher besser zur Behandlung von großen Verformungen eignen. Im Zuge dieser Arbeit wird der Soft Particle Code (SPARC), eine netzfreie Methode, zur Simulation einer Vielzahl von numerischen Problemen der Bodenmechanik, herangezogen. Es werden unterschiedliche Laborversuche, Scherfugenbildungen, Fundamentbelastungen, Drucksondierungen, Turbulenzen in granularen Feststoffen und die Bildung ptygmatischer Faltungen simuliert. Die Beschreibung der Spannungs-Dehnungsbeziehung erfolgt dabei mit den nichtlinearen Entwicklungsgleichungen der Hypoplastizität und der Barodesie. Da numerische Ergebnisse ohne eine Validierung anhand von Experimenten und Theorien keine Aussagekraft haben, werden die durch SPARC erhaltenen Ergebnisse zusätzlich mit experimentellen Daten verglichen. Ein wesentlicher Fokus dieser Arbeit liegt auf den Verbesserungen vom Soft Particle Code, wie z.B. der Rekonditionierung der Lösung, der Definition glatter Randbedingungen und der Berücksichtigung der konvektiven Beschleunigung. Darüber hinaus werden auch eine Reihe von Verbesserungsversuchen vom SPARC ausgeführt. Die Darstellung sowie die ausführliche Erklärung dieser Versuche kann für die zukünftige Forschung nützlich sein.

Abstract

Numerical methods were first applied for solving engineering problems by introducing the mesh-based method of Finite Elements (FE). Since the emergence of FE methods, numerical approaches have been playing a supporting role along theory and experiment in analysis of mechanics problems. One of the deficiencies of standard mesh-based methods is their difficulty in simulating large deformations, which are the case for most problems in soil mechanics. Contrary to mesh-based methods, the meshfree approaches do not necessarily entail connectivities between the material points and should, therefore, be more appropriate for problems associated with large deformations. In this work, a straightforward meshfree method, the Soft Particle Code, is introduced and further developed for simulation of a number of problems in soil mechanics. The simulations comprise conventional laboratory tests, formation of shear bands, punching, cone penetration, turbulence in granular solids and formation of ptygmatic folds. The non-linear evolution equations of hypoplasticity and barodesy are employed for describing the stress-strain relationship. A number of code improvements, such as reconditioning the solution, defining smooth boundary condition and consideration of convective acceleration, which were achieved in the scope of this work played a key role in successful simulation of some of the above mentioned problems. In addition, several unsuccessful attempts were made to improve SPARC which are of practical value for future research. Therefore, an elaborate explanation of all the unsuccessful attempts is provided as well. Finally, since numerical results without validation against experiments and theories are blind and of little worth, the results delivered by SPARC are compared and validated against experimental data.

Contents

List of Figures	ix
List of Tables	xiii
List of Symbols and Abbreviations	xv
1 Soft PArTicle Code	1
1.1 Discretization	1
1.2 Coordinate system and plane strain condition	2
1.3 Governing equations	2
1.4 Neighbor search and interpolation	4
1.5 Procedure of SPARC	5
1.6 Newton solver	6
1.7 Tension control	7
1.8 Reconditioning the solution	8
1.9 Comparison of interpolation methods	8
2 Investigations with SPARC	19
2.1 Laboratory tests	19
2.2 Material model	21
2.3 Setup and evaluation	21
2.4 Oedometric test	22
2.5 Triaxial test	25
2.6 Discussion of results	28
2.7 Simulation of shear bands in clay	29
2.8 Simulation setup	30
2.9 Mohr-Coulomb vs. barodesy	31
2.10 Results	31
2.11 Discussion of results	35
3 Simulation of punching	37
3.1 General remarks	37
3.2 Experimental model test	39
3.3 Numerical simulation and validation	40
4 Cone and pile penetration	47
4.1 General remarks	47

4.2	Experimental analysis	47
4.3	Analytical methods	51
4.4	Numerical models	52
4.5	Simulation of cone penetration with SPARC	55
5	Turbulence in granular solids	69
5.1	Introduction	69
5.2	Element tests and their controllability	69
5.3	Uniqueness of response	70
5.4	Vortices observed in physical tests	71
5.5	Vortices obtained with DEM simulations	73
5.6	Numerical simulation of vortices with SPARC	73
5.7	Physical explanation of the vortices	78
5.8	Implications for element tests	78
5.9	Ptygmatic folds	78
6	Summary and outlook	85
6.1	Summary	85
6.2	Outlook	86
A	Material models	87
A.1	Basics of barodesy	87
A.2	Applied material models	89
B	Unsuccessful attempts	95
B.1	Axisymmetric SPARC	95
B.2	Predetermined velocities on the surface	98
B.3	Static boundary condition through eigenvalues	99
B.4	Rearrangement of particles	100
B.5	Regular arrays of interpolation points	101
B.6	Exclusion of boundary particles	102
B.7	Convective acceleration	103
B.8	Explicit solver	104
B.9	Moving average smoothing	105
B.10	Smoothing the spatial derivatives	105
	Bibliography	107

List of Figures

1.1	Discretization of continuum	1
1.2	Coordinate system and the plane strain condition	2
1.3	Demonstration of vectors for calculation of boundary conditions with prescribed pressure p (left) and smooth boundary condition (right)	3
1.4	Schematic demonstration of biaxial test apparatus	3
1.5	Schematic illustration of boundary conditions in a biaxial test	4
1.6	Neighbors of each particles are the particles lying within a circle of fixed radius r around the particle	4
1.7	Flow chart of SPARC	5
1.8	Illustration of function 1.20 over the calculation domain	9
1.9	Derivative of function f with respect to y along $y = -5$	10
1.10	Derivative of function f with respect to z along $y = -5$	10
1.11	Derivative of function f with respect to y along $z = -8$	11
1.12	Derivative of function f with respect to z along $z = -8$	11
1.13	Derivative of function f with respect to y along $y = 0$	12
1.14	Derivative of function f with respect to z along $y = 0$	12
1.15	Comparison of Euclidean norm of absolute error	14
1.16	Comparison of Chebyshev norm of absolute error	14
1.17	Irregular distribution of particles	15
1.18	Derivative of function f with respect to y along $y = -5$	15
1.19	Derivative of function f with respect to z along $y = 0$	16
1.20	Comparison of derivative of function f with respect to z along $y = 0$ for LP and smoothed LP	16
1.21	Effect of increasing radius of support size, r , on the Euclidean norm of absolute error	17
1.22	Effect of increasing radius of support size, r , on the Chebyshev norm of absolute error	18
2.1	Schematic illustration of the oedometric test	20
2.2	Schematic illustration of the triaxial test	20
2.3	<i>Dense oedometric test</i> – Comparison of element test and 3D simulations for simulation setup I	23
2.4	<i>Dense oedometric test</i> – Comparison of element test and 3D simulations for simulation setup II	23
2.5	<i>Loose oedometric test</i> – Comparison of element test and 3D simulations for simulation setup I	24

2.6	<i>Loose oedometric test</i> – Comparison of element test and 3D simulations for simulation setup II	24
2.7	Comparison of element test and 3D simulation for the <i>unconstrained</i> triaxial test with dense sand	26
2.8	<i>Dense triaxial test</i> – Comparison of element test and 3D simulations for simulation setup I	27
2.9	<i>Dense triaxial test</i> – Comparison of element test and 3D simulations for simulation setup II	27
2.10	<i>Loose triaxial test</i> – Comparison of element test and 3D simulations for simulation setup I	28
2.11	<i>Loose triaxial test</i> – Comparison of element test and 3D simulations for simulation setup II	29
2.12	Illustration of (a) boundary conditions and (b) particles representing the study domain	30
2.13	Element test with barodesy for clay, a) stress-strain curve b) volumetric behavior	31
2.14	Mohr-Coulomb criterion for determination of friction angle ϕ and cohesion c	32
2.15	Simulation with Mohr-Coulomb	32
2.16	Stress-strain curves ($T_{zz} - \epsilon_{zz}$) of all particles in SPARC	33
2.17	Stress-strain curves ($T_{zz} - \epsilon_{zz}$) of all particles in simulations with imperfection implemented in SPARC	34
2.18	Demonstration of shear band in form of void ratio	35
2.19	Demonstration of shear band in form of $ \mathbf{D} $	35
3.1	X-ray photograph of failure mechanism of dense sand	38
3.2	Assumed shape of failure of dense sand	38
3.3	Assumed load-settlement behavior - left: dense soil, right: loose soil	39
3.4	Initial geometry of the model	41
3.5	Demonstration of particle distribution and neighbors	41
3.6	Left: SPARC simulation of shallow penetration into sand at $d_p/B = 0.01$ - smoothed incremental displacement field. Right: PIV result of shallow penetration into sand for the corresponding d_p/B - incremental displacement	42
3.7	Left: SPARC simulation of shallow penetration into sand at $d_p/B = 0.01$ - smoothed maximum shear rate of deformation. Right: PIV result of shallow penetration into sand for the corresponding d_p/B - incremental maximum shear strain	43
3.8	Left: SPARC simulation of shallow penetration into sand at $d_p/B \approx 0.18$ - smoothed incremental displacement field. Right: PIV result of shallow penetration into sand for $d_p/B = 0.33$ - incremental displacement	44
3.9	Left: PIV results of shallow penetration into sand - incremental displacements. Right: ALE simulation of shallow penetration into sand - incremental displacements	44
3.10	Demonstration of void ratio field for $d_p/B = 0.18$, $e_0 = 0.545$	45
3.11	Left: SPARC simulation of shallow penetration into sand at $d_p/B \approx 0.18$ - smoothed maximum shear rate of deformation. Right: PIV result of shallow penetration into sand for the $d_p/B = 0.33$ - incremental maximum shear strain	45
3.12	Comparison of load-displacement behavior for SPARC and the experiment	46

3.13	Comparison of the shape of the shear band obtained for the analytical solution (see Fig. 3.2) with the results of SPARC	46
4.1	PIV results for pile penetration in dense sand	48
4.2	Velocity field close to advancing pile	49
4.3	Trajectory during pile installation	49
4.4	Demonstration of strains surrounding a pile during an increment of penetration	50
4.5	Effect of container size on cone penetration resistance	51
4.6	Comparison of displacement field for smooth cone, (left) and rough cone, (right)	52
4.7	Comparison of the measured and predicted load-displacement curves of pile penetration for pile with conical tip	54
4.8	Displacement vectors of particles obtained by discrete element method	55
4.9	Geometry of the model	57
4.10	Vectors for explanation of Boundary condition I	58
4.11	Obtained solution (velocity field) for increasing relative penetration depths - boundary condition I	60
4.12	Zoom of obtained solution (velocity field) around the cone for increasing relative penetration depths - boundary condition I	61
4.13	Vectors for explanation of Boundary condition II	62
4.14	Comparison of obtained velocities for smooth boundary conditions I and II	62
4.15	Obtained solution (velocity field) for increasing relative penetration depths - boundary condition II	63
4.16	Zoom of obtained solution (velocity field) around the cone for increasing relative penetration depths - boundary condition II	64
4.17	Obtained solution (velocity field) with adherence at the cone surface for increasing relative penetration depths	66
4.18	Zoom of obtained solution (velocity field) with adherence around the cone for increasing relative penetration depths	67
4.19	Changes in void ratio and norm of stress of a particle adherent to the shaft of the cone	68
5.1	Schematic illustration of the oedometric test	71
5.2	Velocity fluctuations obtained with Digital Image Correlation in the $1\gamma_2\varepsilon$ -apparatus	72
5.3	Post-peak (softening) sequence of velocity fluctuations within shear bands in biaxial tests with dense sand	72
5.4	Post-peak (residual or critical state) sequence of velocity fluctuations within shear bands in biaxial tests with dense sand	72
5.5	Velocity fluctuations in simple shear simulated with DEM	73
5.6	Vortex structures obtained with DEM simulation of a direct shear test	73
5.7	Velocities in a triaxial test sample with bender elements, numerical simulations with DEM	74
5.8	Comparison of vortices for three different material models in oedometric test	74
5.9	Stress-strain curves for oedometer (left), true biaxial (middle) and simple shear simulations (right), respectively	75

5.10	Development of vortices with increasing oedometric deformation, at the strains indicated in Fig. 5.9 - left, rough upper and lower plates	75
5.11	Zoom in of Fig. 5.10-f	75
5.12	Development of vortices with increasing oedometric deformation, at the strains indicated in Fig. 5.9 - with smooth upper and lower plates	76
5.13	Influence of the sample size, a) $h_0/B = 2.5$, b) $h_0/B = 1.25$ and c) $h_0/B = 0.5$ - rough upper and lower plates	76
5.14	Influence of the density of particles (initial spacing size d in the oedometric test simulation) a) $d = 50$ mm, b) $d = 25$ mm and c) $d = 12.5$ mm - rough upper and lower plates	77
5.15	Development of vortices with increasing biaxial deformation at the strains indicated in Fig. 5.9 - middle	77
5.16	Development of vortices with increasing simple shear deformation at the strains indicated in Fig. 5.9 - right	77
5.17	Effect of turbulences on the stress-strain relationship - development of difference in T_{zz} with increasing oedometric deformation	78
5.18	Ptygmatic folds in rock	79
5.19	Ptygmatic fold in modeling clay under simple shear deformation	80
5.20	Geometry of the model, the red particles in the middle of the model represent the "competent material line"	80
5.21	Deformation of material line ($y = 0.05$ m) in simple shear test for setup with competent material	81
5.22	Deformation of material line ($y = 0.05$ m) in simple shear test for homogeneous setup	81
5.23	Comparison of vortices for homogeneous setup (left) and setup with competent material line (right), $\varepsilon_{zy} = 0.7$	82
5.24	Fluctuation (\mathbf{v}') in dependence of void ratio of the competent material line	83
A.1	Illustration of the first rule of Goldscheider	88
A.2	Illustration of the second rule of Goldscheider	88
A.3	Mathematical interpretation of the second rule	89
A.4	Demonstration of state variables at peak and critical state for a dense sample	90
B.1	Vector \mathbf{p} in cylindrical coordinates $r\vartheta z$	96
B.2	Stress tensor \mathbf{T} in cylindrical coordinates	97
B.3	Determination of velocities on the surface in the first sub-step (left), determination of velocities for field particles in the second sub-step (right)	98
B.4	Rearrangement of particles	101
B.5	Demonstration of soft particles and interpolation points	102
B.6	Left: neighbors for interpolation of velocity gradient - Right: neighbors for interpolation of divergence of stress	103
B.7	Left: velocity field without application of moving average smoothing (oscillations in the velocities are apparent)-right: velocity field after application of moving average smoothing	106

List of Tables

2.1	Setup for oedometric tests	21
2.2	Setup for triaxial tests	21
2.3	Simulation parameters for the oedometric test	22
2.4	SPARC simulation parameters for the triaxial test	26
2.5	Summary of simulations	31
3.1	Granulometric and mechanical properties of the model sand	40
4.1	Description of kinematic boundary conditions for rough and smooth cone	52
A.1	Calibration of barodesy for sand (2011) for Hostun sand	90
A.2	Calibration of barodesy for sand (2015) for Hostun sand	91
A.3	Calibration of hypoplastic material model after von Wolffersdorff for model test sand in Aubram’s experiments and Hostun sand	92
A.4	Calibration of barodesy for clay for Dresden clay	93

List of Symbols and Abbreviations

A list of more common symbols, abbreviations and operators in the text is offered here. All symbols (whether listed here or not) are also well defined in the text.

\mathbf{b}	acceleration vector
B	width of foundation
C_c	curvature of grain size distribution curve
C_u	coefficient of non-uniformity
d	grid space (average distance between two particles)
d_p	penetration depth
d_{50}	mean grain size (characteristic grain size)
d_{10}, d_{30}, d_{60}	characteristic grain size
D	maximum diameter of the cone
\mathbf{D}	stretching tensor
D_f	embedment depth of foundation
$\Delta\gamma_s$	maximum incremental shear strain
Δt	time increment
e	void ratio
\dot{e}	time derivative of void ratio
e_0	initial void ratio
e_c	critical state void ratio (pressure dependent)
e_{\max}	maximum void ratio
e_{\min}	minimum void ratio, e_{\min} in Tab. A.2 is a material constant
\mathbf{e}_n	unit normal vector to the surface
\mathbf{e}_r	unit vector in r direction
\mathbf{e}_t	unit tangential vector of the surface

\mathbf{e}_x	unit vector in x -direction
\mathbf{e}_z	unit vector in z -direction
ε	accepted tolerance (error)
$\boldsymbol{\varepsilon}$	strain tensor
$\varepsilon_1, \varepsilon_2, \varepsilon_3$	first, second and third principal strains, respectively
ε_v	volumetric strain
$\ \varepsilon\ _2$	Euclidean (2-Norm) of absolute error
$\ \varepsilon\ _\infty$	Chebyshev (∞ -Norm) of absolute error
\mathbf{g}	gravitational acceleration vector
γ	unit weight of soil
$\dot{\gamma}_s$	maximum shear rate
k	Newton solver iteration number
\mathbf{K}	Jacobian matrix
K_0	lateral earth pressure coefficient at rest
κ^*	slope of the unloading line under isotropic normal compression in logarithmic demonstration
λ^*	slope of the isotropic normal compression line in logarithmic demonstration
LP	linear polynomial interpolation without a constant term
LPC	linear polynomial interpolation with a constant term
N	ordinate intercept of the isotropic normal compression line in logarithmic demonstration
n_p	number of particles
∇	gradient operator
$\nabla \cdot$	divergence operator
p	prescribed pressure (traction) to the surface
φ	friction angle
φ_c	critical friction angle
φ_p	peak friction angle
q	surcharge stress
Q	bearing capacity
Q_{ult}	ultimate bearing capacity

r	radius of circle of neighbor search (support size)
RPIM	radial point interpolation method
(r, ϑ, z)	cylindrical coordinate system
\mathbf{r}	vector of residuum of the governing equation
ρ	density
$\dot{\rho}$	time derivative of density
ρ_n	numerical density
ρ_s	grain mass density
t	time step
\mathbf{t}	stress vector (traction)
\mathbf{T}	effective Cauchy stress tensor
$\dot{\mathbf{T}}$	objective rate of Cauchy stress tensor
$\dot{\mathbf{T}}$	time derivative of Cauchy stress tensor
T_1, T_2, T_3	first, second and third principal stresses, respectively
$\text{tr} \mathbf{X}$	sum of diagonal components of a tensor
u	pore water pressure
\mathbf{v}	velocity vector
v_p	upper plate velocity
$\bar{\mathbf{v}}$	mean velocity
\mathbf{v}'	fluctuation of velocity
\mathbf{Q}	rotation matrix
\mathbf{W}	spin tensor
(x, y, z)	Cartesian coordinate system
\mathbf{x}	position vector
$ \mathbf{X} $	Euclidean norm of a tensor, $ \mathbf{X} = \sqrt{\text{tr} \mathbf{X}^2}$
\mathbf{X}^0	normalization of a tensor $\mathbf{X}^0 = \mathbf{X}/ \mathbf{X} $
y	any of the governing equations
\mathbf{y}	vector of all governing equations

1 Soft PARticle Code

The basics of the meshfree numerical method implemented in the code SPARC and its further developments in the scope of this study are explained in this chapter. Furthermore, a comprehensive investigation regarding the quality of interpolation methods for the determination of spatial derivatives is conducted. Interested readers can refer to Chen [11] and Polymerou [42] for further details about the development and application of SPARC.

1.1 Discretization

In SPARC the continuum with unlimited number of degrees of freedom is discretized by a limited number material points (see Fig. 1.1), the so-called *soft particles*. At time t , for each particle, position \mathbf{x} and the field variables such as velocity \mathbf{v} , density ρ (or void ratio e) and the stress state \mathbf{T} are known.

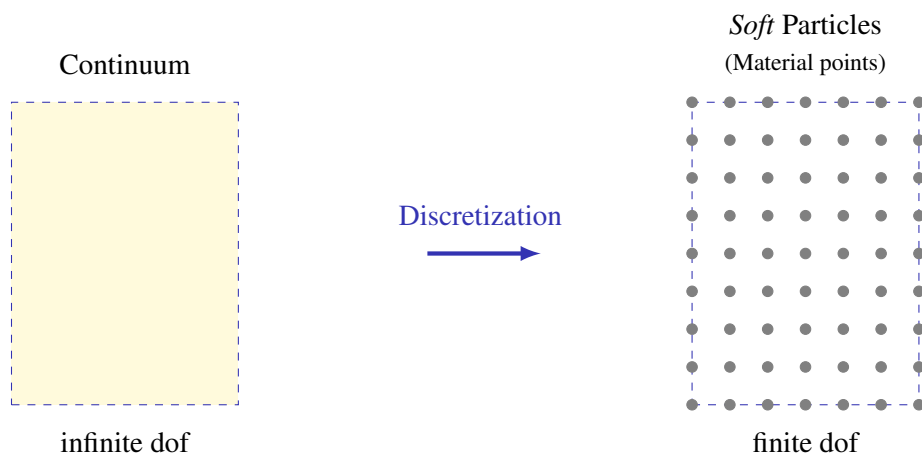


Figure 1.1: Discretization of continuum into a finite number of material points, "soft particles"

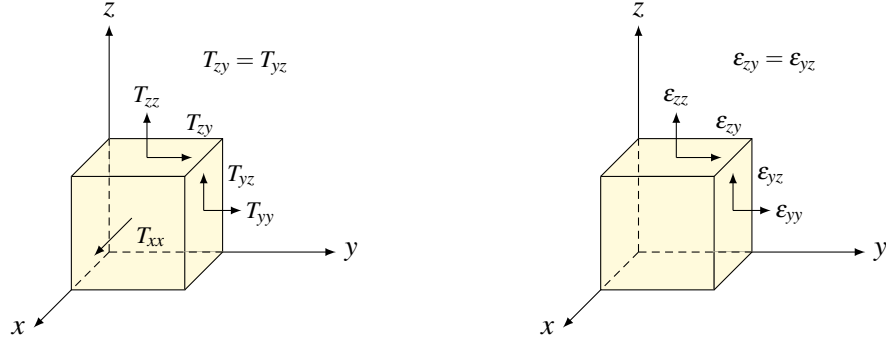


Figure 1.2: Coordinate system and the plane strain condition in x -direction, left: stress tensor \mathbf{T} , right: strain tensor $\boldsymbol{\epsilon}$

1.2 Coordinate system and plane strain condition

In this study, the simulations are conducted 2D in x -plane with plane strain condition, i.e. no displacement in x -direction (see Fig. 1.2)¹. As a result of the plane strain condition, the shear stresses and all components of the strain on x -plane vanish. Therefore, the stress and strain tensors read,

$$\mathbf{T} = \begin{bmatrix} T_{xx} & 0 & 0 \\ 0 & T_{yy} & T_{yz} \\ 0 & T_{zy} & T_{zz} \end{bmatrix}, \quad \boldsymbol{\epsilon} = \begin{bmatrix} 0 & 0 & 0 \\ 0 & \epsilon_{yy} & \epsilon_{yz} \\ 0 & \epsilon_{zy} & \epsilon_{zz} \end{bmatrix}.$$

Sign convention. When a normal component of the stress or strain tensor (e.g. T_{yy} or ϵ_{yy}) is positive, it means that the normal component acting on the right side pulls to the right and the normal component on the left side pulls to the left and consequently it is a *tensile* stress. Analogously, when a normal component is negative, it is *compressive*. The sign of tangential components (e.g. T_{yz} and ϵ_{yz}) has no intrinsic physical meaning and a positive tangential component represents an upward-acting vector on the right side and a downward-acting component on the left side, Malvern [35].

Effective stresses. For all the simulations in this study, the soil is considered to be dry and therefore, pore water pressure (u) is equal to zero and \mathbf{T} represents the effective stress tensor.

1.3 Governing equations

Particles are divided in SPARC into two groups, *field* particles, at which the Cauchy equation of motion applies (Eq. 1.1),

$$\nabla \cdot \mathbf{T} + \rho \mathbf{g} = \mathbf{0}, \quad (1.1)$$

and the *boundary* particles. The boundary particles have either kinematic boundary conditions with prescribed velocities or static boundary conditions. The static boundary

¹Only the simulations of Secs. 2.1 to 2.6 are conducted in 3D, (x, y, z) space.

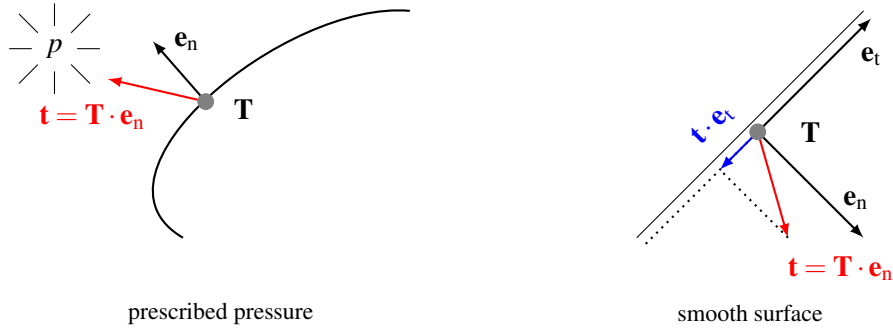


Figure 1.3: Demonstration of vectors for calculation of boundary condition with prescribed pressure p (left) and smooth boundary (right), $\mathbf{t} = \mathbf{T} \cdot \mathbf{e}_n$ is the stress vector

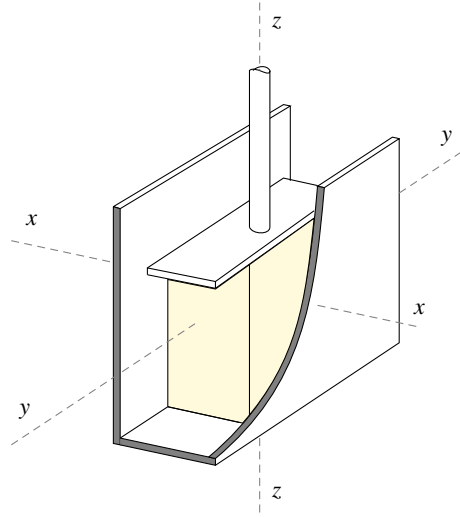


Figure 1.4: Schematic demonstration of biaxial test apparatus

condition in case of prescribed pressure (traction) is,

$$\mathbf{T} \cdot \mathbf{e}_n - (-p) \cdot \mathbf{e}_n = \mathbf{0}, \quad (1.2)$$

where \mathbf{e}_n is the normal unit vector on the surface and p is the pressure (see Fig. 1.3, left). In case of smooth boundary (particles in contact with smooth elements such as walls, cone and etc.), the following boundary condition is applied, which demands that the shear stresses on the surface disappear (\mathbf{e}_t is the tangential unit vector perpendicular to \mathbf{e}_n , see Fig. 1.3, right),

$$\mathbf{e}_n^T \cdot \mathbf{T} \cdot \mathbf{e}_t = 0. \quad (1.3)$$

The boundary conditions and their implementation in SPARC are explained for a biaxial test (see Fig.1.4). In Fig. 1.5, the boundary conditions for a 2D simulation of biaxial test are demonstrated. For the particles adjacent to the membrane, subject to the constant pressure p , the static boundary condition as described in Eq. 1.2 is applied. For the particles lying on the end plates, in vertical direction the velocities are prescribed equal

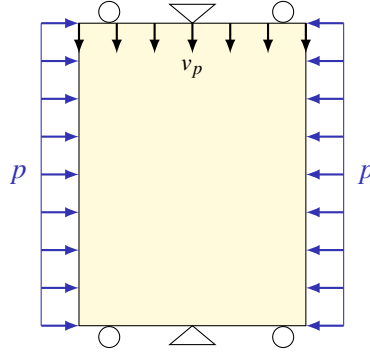


Figure 1.5: Schematic illustration of boundary conditions in a biaxial test

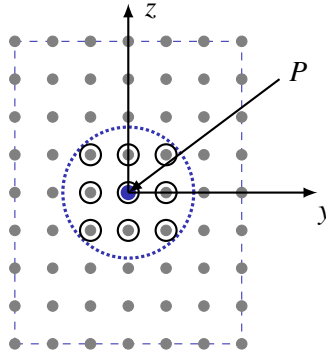


Figure 1.6: Neighbors of each particle are the particles lying within a circle of fixed radius r around the particle

to v_p for the upper plate and zero for the lower plate. However, for these particles, the boundary condition in the horizontal direction is the smooth surface as explained in Eq. 1.3. For the rest of the particles, which represent the field, the Cauchy equation of motion (Eq. 1.1) is considered. The results of simulation of biaxial test with SPARC are presented in Sec. 2.7.

1.4 Neighbor search and interpolation

In Fig. 1.6 the neighbors of particle P are shown. For each particle the neighbors, which consists of particles lying within a circle of fixed radius around the particle, are searched. By means of the neighbors, the spatial derivatives are calculated. The spatial derivatives are the velocity gradient ($\nabla \mathbf{v}$) and the divergence of the stress tensor ($\nabla \cdot \mathbf{T}$).

For a 2D problem the velocity in the horizontal direction, v_y , is interpolated by Eq. 1.4,

$$v_y = a_1 y + a_2 z, \quad (1.4)$$

where the origin of the coordinate system is shifted to the location of the particle P (see Fig. 1.6). The constants a_1 and a_2 are determined by least square method. Therefore, the

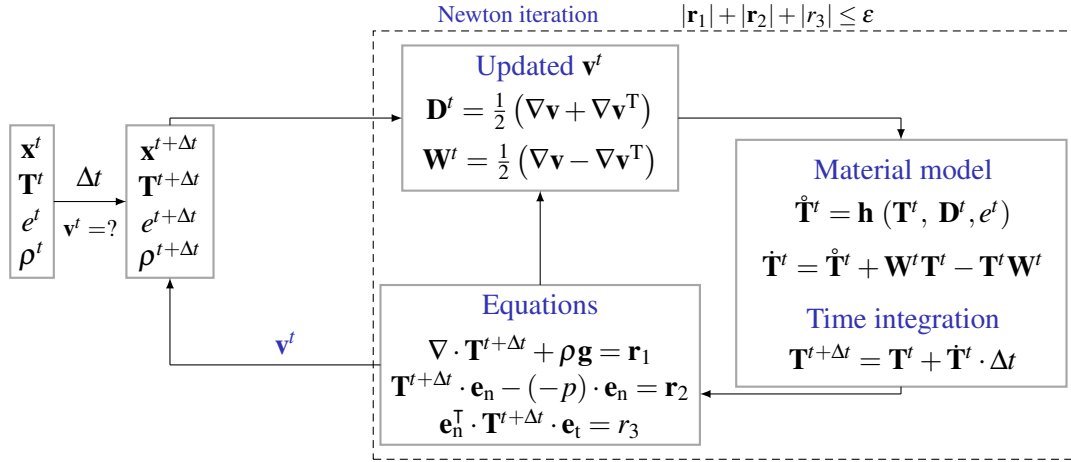


Figure 1.7: Flow chart of SPARC

spatial derivatives for v_y are,

$$\frac{\partial v_y}{\partial y} = a_1, \quad \frac{\partial v_y}{\partial z} = a_2. \quad (1.5)$$

The same interpolation is also applied to each component of the stress tensor, e.g. T_{yy} is interpolated as,

$$T_{yy} = b_1 y + b_2 z, \quad (1.6)$$

and like before, the spatial derivatives read,

$$\frac{\partial T_{yy}}{\partial y} = b_1, \quad \frac{\partial T_{yy}}{\partial z} = b_2. \quad (1.7)$$

The above procedure is applied to each component of velocities and stress of each particle and consequently, at each time step, the velocity gradient $\nabla \mathbf{v}$ and divergence of the stress $\nabla \cdot \mathbf{T}$ for each particle is calculated. For a more detailed description of the interpolation procedure the reader is referred to Chen [11].

1.5 Procedure of SPARC

In Fig. 1.7, the framework of SPARC is summarized. At time step t , the position of particles \mathbf{x}^t and the field variables, stress tensor \mathbf{T}^t , void ratio e^t and density ρ^t are known. The velocities of particles \mathbf{v}^t are the unknowns. Once the velocities are found, all field variables can be updated to the next time step $t + \Delta t$. In order to find the solution \mathbf{v}^t , a first guess for the velocities is made and the velocity gradient as explained in Sec. 1.4 for each particle is calculated. The symmetric part of velocity gradient, the so-called stretching tensor \mathbf{D} and the non-symmetric part, the spin tensor \mathbf{W} are determined. By means of the material model, the objective rate of stress state $\dot{\mathbf{T}}^t$, as a function of the current stress state, stretching tensor and void ratio is calculated. Furthermore, the Jaumann-Zaremba relation is applied to obtain the time derivative of the stress. Afterwards, the stress is updated to $\mathbf{T}^{t+\Delta t}$.

In the next step, the governing equations are built for the field particles and also the

boundary particles. The residua of the equations are calculated and compared with the accepted tolerance (ε). Newton iteration method is implemented to solve the system of non-linear equations.

After the velocity field \mathbf{v}^t is obtained, for which the governing equations are satisfied, the field variables are updated as follows,

$$\begin{aligned}\mathbf{x}^{t+\Delta t} &= \mathbf{x}^t + \mathbf{v}^t \cdot \Delta t, \\ \mathbf{T}^{t+\Delta t} &= \mathbf{T}^t + \dot{\mathbf{T}}^t \cdot \Delta t, \\ e^{t+\Delta t} &= e^t + \dot{e}^t \cdot \Delta t, \\ \rho^{t+\Delta t} &= \rho^t + \dot{\rho}^t \cdot \Delta t,\end{aligned}$$

where,

$$\dot{\mathbf{T}}^t = \mathbf{h}(\mathbf{T}^t, e^t, \mathbf{D}^t) + \mathbf{W}^t \mathbf{T}^t - \mathbf{T}^t \mathbf{W}^t, \quad (1.8)$$

$$\dot{e}^t = (1 + e^t) \cdot (\nabla \cdot \mathbf{v}^t), \quad (1.9)$$

and

$$\dot{\rho}^t = -\rho^t \cdot (\nabla \cdot \mathbf{v}^t). \quad (1.10)$$

1.6 Newton solver

For solving the nonlinear system of equations, the iterative Newton method is employed in SPARC. However, this method failed to converge for many of the problems presented in this work after the deformations became large or localization of deformation occurred. As described in Fig. 1.7, in SPARC the velocities at time step (\mathbf{v}^t) are the unknowns. Here we define n equal to the number of degrees of freedom, therefore, the matrix of unknown velocities at time step t for the first iteration of the Newton solver, $k = 1$, can be defined as,

$$\mathbf{v}_{k=1}^t = [v_i^t]_{i=1\dots n}. \quad (1.11)$$

The equations ($y = 0$), expressing either the boundary conditions (Eq.1.2 or Eq. 1.3) or the Cauchy equation of motion (Eq. 1.1) are defined as,

$$y := \begin{bmatrix} \nabla \cdot \mathbf{T} + \rho \mathbf{g} \\ \mathbf{T}^{t+\Delta t} \cdot \mathbf{e}_n - (-p) \cdot \mathbf{e}_n \\ \mathbf{e}_n^\top \cdot \mathbf{T}^{t+\Delta t} \cdot \mathbf{e}_t \end{bmatrix}. \quad (1.12)$$

For each degree of freedom, there is an equation $y = 0$ (Eq. 1.12) to be solved². All equations are collected in the vector \mathbf{y} ,

$$\mathbf{y} = [y_i]_{i=1\dots n}. \quad (1.13)$$

²Theoretically, it is possible to have more than one equation for each degree of freedom, however, in the scope of this study the Newton solver has never been able to find a solution which can simultaneously satisfy two equations for one degree of freedom.

The influence of each component of v_i on y_i in the k -th iteration of the Newton solver is expressed by the Jacobian matrix and is calculated as,

$$\mathbf{K}_k = \left[\frac{\partial y_i(\mathbf{v})}{\partial v_j} \right]_{i,j=1\dots n}. \quad (1.14)$$

The Jacobian matrix is an $n \times n$ matrix, and is the most time consuming part of calculation. Therefore, the procedure is parallelized in SPARC so that each column is computed in one individual central processing unit (CPU),

$$\mathbf{K}_k = \begin{bmatrix} \frac{\partial y_1}{\partial v_1} & \frac{\partial y_1}{\partial v_2} & \cdots & \frac{\partial y_1}{\partial v_n} \\ \frac{\partial y_2}{\partial v_1} & \frac{\partial y_2}{\partial v_2} & \cdots & \frac{\partial y_2}{\partial v_n} \\ \vdots & \vdots & \vdots & \vdots \\ \frac{\partial y_n}{\partial v_1} & \frac{\partial y_n}{\partial v_2} & \cdots & \frac{\partial y_n}{\partial v_n} \end{bmatrix}^{[n \times n]}. \quad (1.15)$$

After the Jacobian matrix is calculated, its inversion is computed in order to update the velocities to the $(k + 1)$ -th iteration of the solver,

$$\mathbf{v}'_{k+1} = \mathbf{v}_k - \mathbf{K}_k^{-1} \mathbf{y}(\mathbf{v}'_k). \quad (1.16)$$

Afterwards, the field variables are updated with \mathbf{v}'_{k+1} with the relationships introduced in Eqs.1.8 to 1.10 and the residua of the equations are compared with the accepted tolerance (see Fig. 1.7). If the residuum is smaller than the tolerance, the solution is accepted and the state variables are updated to the next time step. Otherwise, the Newton iteration is repeated.

1.7 Tension control

In order to avoid tension, the following procedure is implemented in SPARC. It must be noted that in SPARC the continuum mechanic convention for pressure and tension is applied, by which the pressure is negative and tension is positive, (see Sec. 1.2).

1. At time step $t + \Delta t$, the stress state is updated for each particle,

$$\mathbf{T}^{t+\Delta t} = \mathbf{T}^t + \dot{\mathbf{T}}^t \cdot \Delta t,$$

where,

$$\dot{\mathbf{T}}^t = \mathbf{h}(\mathbf{T}^t, \mathbf{e}^t, \mathbf{D}^t) + \mathbf{W}^t \mathbf{T}^t - \mathbf{T}^t \mathbf{W}^t.$$

2. The principal stresses (T_1, T_2, T_3) for each particle are calculated.
3. The eigenvectors for each particle are calculated and stored in the matrix \mathbf{Q} , whose columns are the corresponding eigenvectors.
4. The principal stresses (T_i) for $i = 1 \rightarrow 3$ are controlled and,

$$\text{if } T_i \geq 0,$$

then,

$$T_i = -1 \times 10^{-3} \text{ kPa.}$$

5. The updated \mathbf{T} is returned into the Cartesian coordinate system (x, y, z) ,

$$\mathbf{T}^{t+\Delta t} = \mathbf{Q} \cdot \mathbf{T} \cdot (\mathbf{Q})^{-1}.$$

1.8 Reconditioning the solution

Throughout this study many different approaches were implemented in SPARC to improve the performance of the solver. The most efficient approach is described here.

Let k be the number of iterations of the solver and t the time step, then the residuum of the governing equation $\mathbf{y} = \mathbf{0}$ at time step t after k iterations is \mathbf{r}_t^k . At each time step, the governing equations $\mathbf{y}(\mathbf{v}) = \mathbf{0}$ are calculated and the goal is to minimize the residuum of each equation. Theoretically, convergence of Newton solver means,

$$\lim_{k \rightarrow \infty} |\mathbf{r}_t^k| \rightarrow 0. \quad (1.17)$$

However, numerically we assume that the convergence after a finite number of iterations is successful if,

$$|\mathbf{r}_t^k| \leq \varepsilon, \quad (1.18)$$

where ε is the prescribed tolerance. Should this not be achieved, the residuum at time step t after r iterations, \mathbf{r}_t^r will be stored and added to the governing equation for the next $t + 1$ time step. This means that at time step $t + 1$, the governing equation reads,

$$\mathbf{y}_{t+1} = \mathbf{y} + \mathbf{r}_t^r = \mathbf{0}. \quad (1.19)$$

This procedure can be applied to each time step, for which the Newton solver is not capable of finding a solution unless the residuum is too large. The procedure proved to be efficient in simulating the foundation settlement in Chp. 3. When the peak of the load-settlement curve was reached (see Fig. 3.12), reconditioning of the solution for a number of time steps helped to pass the peak and continue the simulation.

1.9 Comparison of interpolation methods

The interpolation methods play a crucial role in the quality of results and also the convergence of the solver in SPARC. As explained in Sec. 1.4, interpolation is required in SPARC for the calculation of velocity gradient and divergence of stress. For the simulations with SPARC in this study, linear polynomial without a constant term (LP) and with the least possible number of neighbors has proved to deliver the smoothest results and better convergence for the solver and is applied for all simulations in this study. Besides first order polynomial without the constant term, two other interpolation methods, namely first order polynomial with the constant term (LPC) and radial point interpolation method (RPIM) are also investigated. For a detailed implementation of radial point interpolation method in SPARC, the reader is referred to Polymerou [42] and Liu et al. [34]. In this chapter we investigate the accuracy and quality of the above-mentioned interpolation in predicting the *derivative* of a function. It is important to mention, that since in SPARC the spatial derivatives are of interest, evaluating the quality and accuracy of an interpolation method in predicting the derivatives should be examined and *not* the

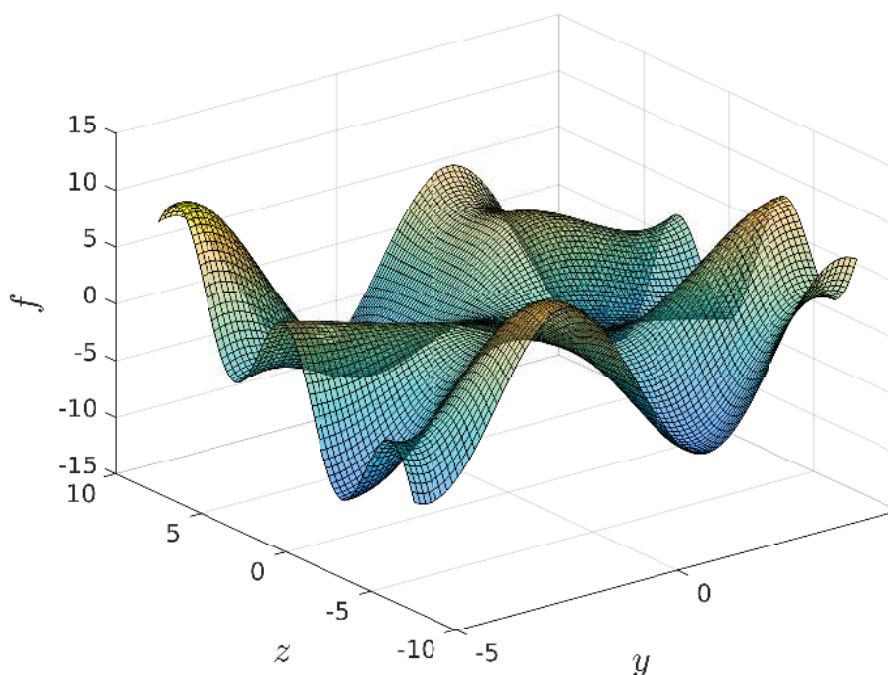


Figure 1.8: Illustration of function 1.20 over the calculation domain

ability of the interpolation method in reproducing the function. For this purpose, two sets of particles are used, a regular distribution of particles and an irregular distribution of particles. The derivatives are plotted against the analytical solution on the boundaries of the domain and also in the middle of the domain.

1.9.1 Regular distribution of particles

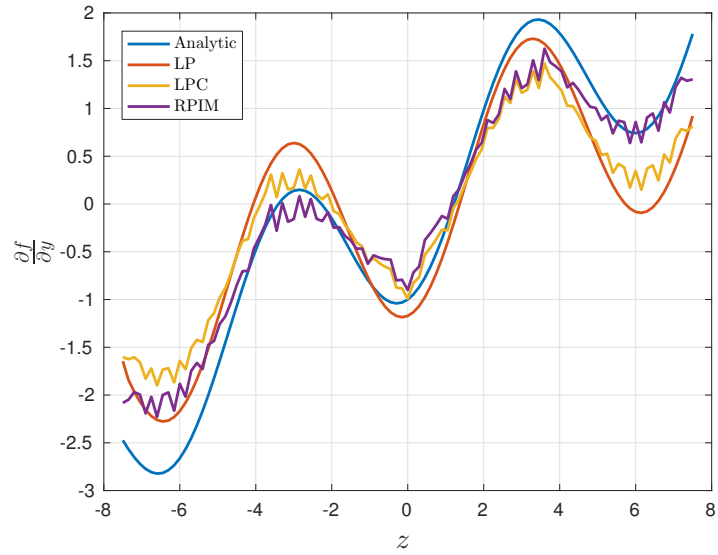
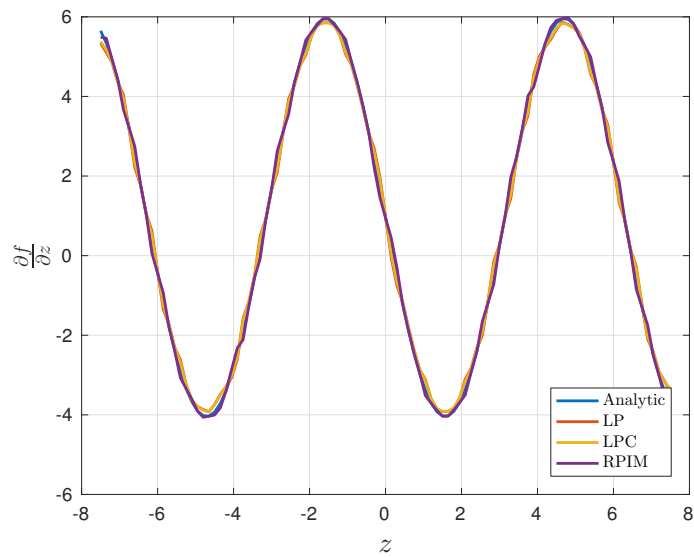
The function 1.20 (illustrated in Fig. 1.8) is used as the reference function for our purpose of evaluating the quality of the interpolation methods,

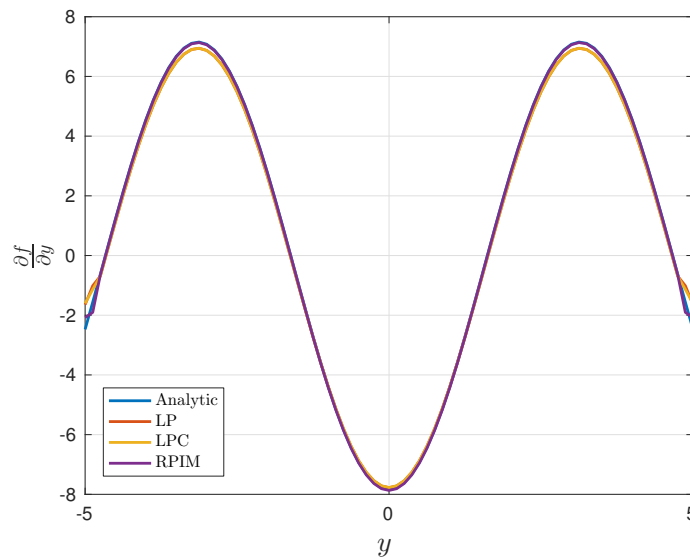
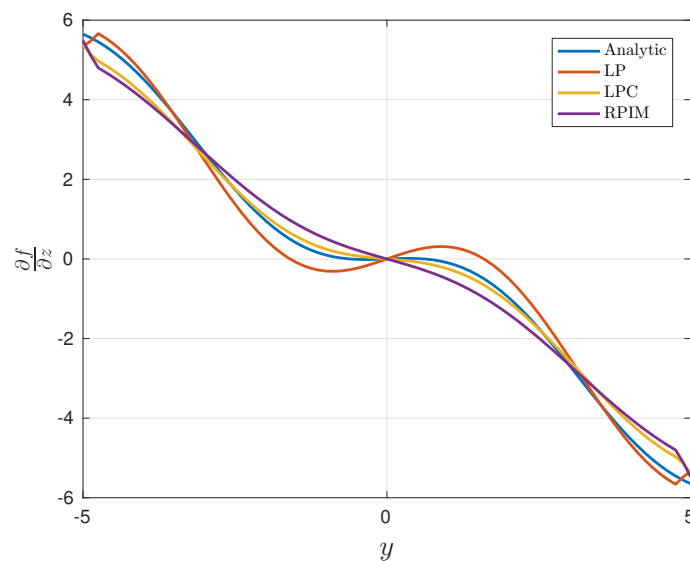
$$f = z \sin y - y \cos z. \quad (1.20)$$

For comparison of the three interpolation methods, a regular distribution of over 2000 particles which equals to a grid space of 0.3 is created.

1.9.2 Results

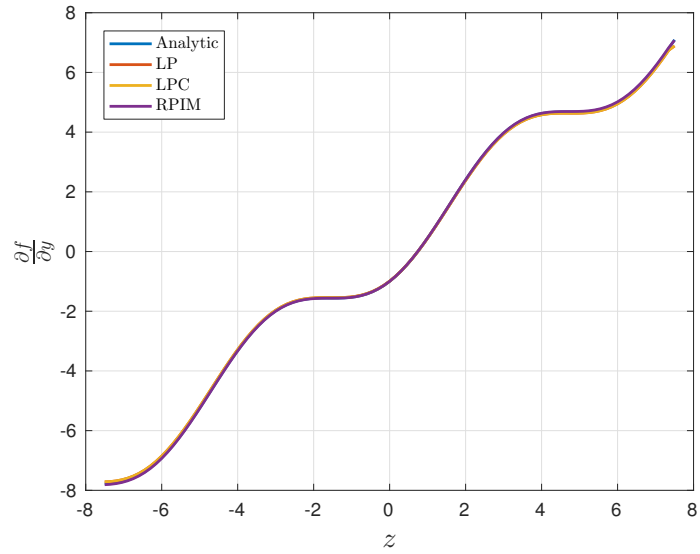
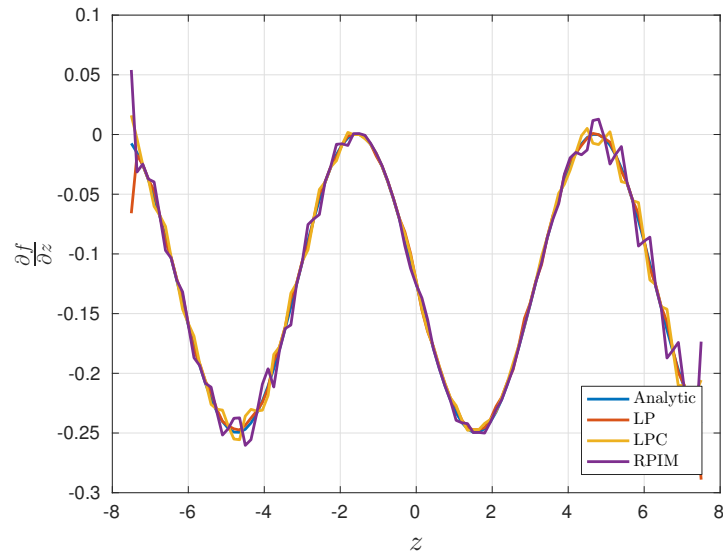
The numerical derivatives are calculated and the results are compared with the analytical solution. In order to offer a good demonstration of the results, the results are plotted along three lines of the study domain, $y = -5$, $z = -8$ and $y = 0$ in the middle of the domain (see the x -plane in Fig. 1.8). Figs. 1.9 and 1.10 show that the derivative along $y = -5$ with respect to z are in better agreement with the analytical solution compared to the derivative with respect to y . For $\frac{\partial f}{\partial y}$ along $y = -5$ (see Fig. 1.9), results of the

Figure 1.9: Derivative of function f with respect to y along $y = -5$ Figure 1.10: Derivative of function f with respect to z along $y = -5$

Figure 1.11: Derivative of function f with respect to y along $z = -8$ Figure 1.12: Derivative of function f with respect to z along $z = -8$

RPIM and LPC are comparable and show oscillations. The LP method although delivers a smooth curve, does deviate from the analytical solution considerably. For $\frac{\partial f}{\partial z}$ along $y = -5$ (see Fig. 1.10), the results of LPC method show oscillation and the other two methods have an almost good agreement, however, near to boundary the deviation of results are not negligible.

For particles along $z = -8$, the spatial derivatives are plotted in Figs. 1.11 and 1.12. Fig. 1.11 shows that smooth curves are obtained for $\frac{\partial f}{\partial y}$ along $z = -8$. LP and RPIM methods show a better agreement with the analytical solution in comparison with the LPC method, however, the results near to boundary deviate from the analytical solution.

Figure 1.13: Derivative of function f with respect to y along $y = 0$ Figure 1.14: Derivative of function f with respect to z along $y = 0$

Although Fig. 1.12 shows that smooth curves are obtained for $\frac{\partial f}{\partial z}$ along $z = -8$, the numerical solutions of all three methods deviate considerably from the analytical solution. At the boundaries $[-5, 5]$, the smoothness of the solution gets also lost.

For the particles along $y = 0$, the spatial derivatives are plotted in Figs. 1.13 and 1.14. Fig. 1.13 shows that all three methods deliver a smooth solution which also corresponds well to the analytical solution, with the exception that the LPC method deviates from the analytical solution at the boundaries.

In contrast to $\frac{\partial f}{\partial y}$ for the particles along $y = 0$, the solution for $\frac{\partial f}{\partial z}$ of these particles demonstrates oscillation for the LPC and RPIM method. The results of the LP method

are more acceptable, except for the limits of the boundary $[-8, 8]$, where the LP method also demonstrates oscillations.

1.9.3 Quantitative Comparison

In order to compare the results quantitatively, for each method, firstly the absolute error at each particle i is calculated,

$$\varepsilon_{yi} = \left| \left(\frac{\partial f}{\partial y} \right)_i - \left(\frac{\partial \hat{f}}{\partial y} \right)_i \right|, \quad (1.21)$$

$$\varepsilon_{zi} = \left| \left(\frac{\partial f}{\partial z} \right)_i - \left(\frac{\partial \hat{f}}{\partial z} \right)_i \right|. \quad (1.22)$$

where f and \hat{f} represent the function 1.20 and its interpolation, respectively. Secondly, the Euclidean or 2- Norm,

$$\|\varepsilon_y\|_2 = \sqrt{\sum_{i=1}^n \varepsilon_{yi}^2}, \quad (1.23)$$

$$\|\varepsilon_z\|_2 = \sqrt{\sum_{i=1}^n \varepsilon_{zi}^2}, \quad (1.24)$$

and the Chebyshev or ∞ -Norm,

$$\|\varepsilon_y\|_\infty = \max_{i=1, \dots, n} \varepsilon_{yi}, \quad (1.25)$$

$$\|\varepsilon_z\|_\infty = \max_{i=1, \dots, n} \varepsilon_{zi}, \quad (1.26)$$

are calculated. The results are summarized in Figs. 1.22 and 1.21.

According to the results, the LPC method shows the largest error and the LP and the RPIM methods expose comparable error. However, the LP method offers three advantages in comparison to the RPIM method. Firstly, the results are smoother. Secondly, the calculation time with LP is much shorter as opposed to RPIM and finally, for LP method a less number of neighbors are required.

1.9.4 Irregular distribution of particles

The same problem is conducted for an irregular distribution of particles. The study domain and the reference function are the same as introduced in Sec. 1.9.1. The irregular number of particles is created randomly and the number of particles is the same as for the regular distribution of particles. The random distribution of particles is demonstrated in Fig. 1.17.

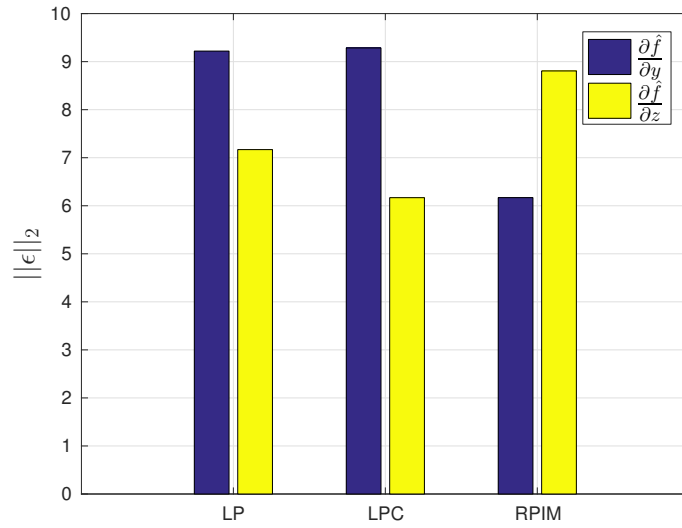


Figure 1.15: Comparison of Euclidean norm of absolute error for LP, LPC and RPIM for derivatives with respect to y (blue bar) and z (yellow bar)

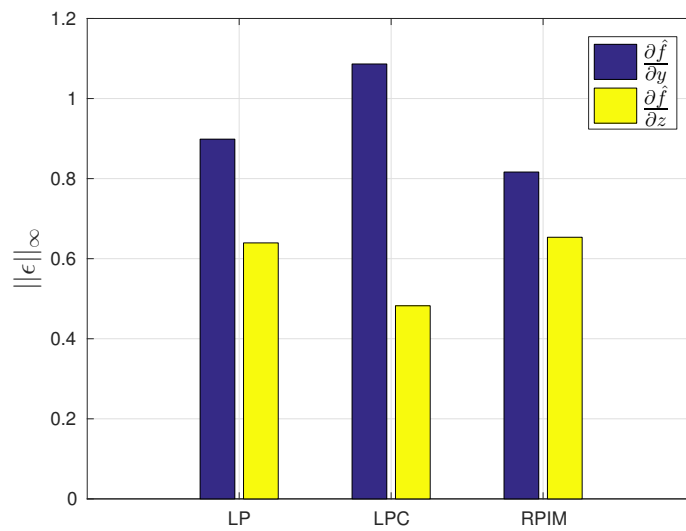


Figure 1.16: Comparison of Chebyshev norm of absolute error for LP, LPC and RPIM for derivatives with respect to y (blue bar) and z (yellow bar)

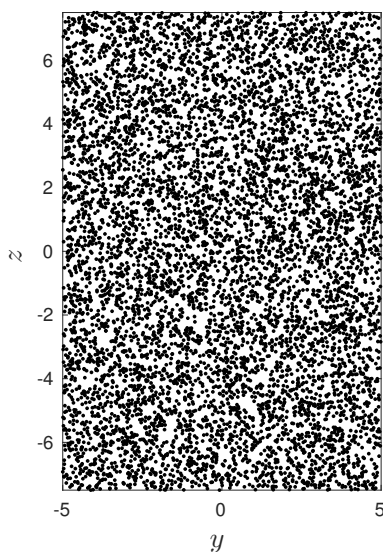
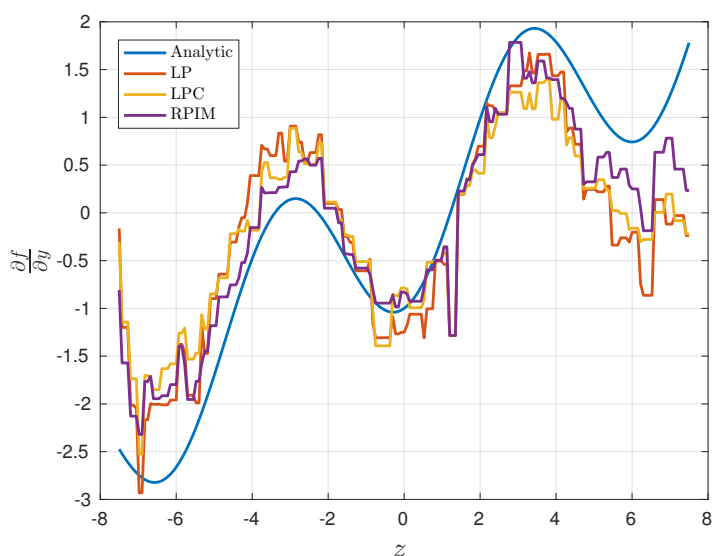


Figure 1.17: Irregular distribution of particles

Figure 1.18: Derivative of function f with respect to y along $y = -5$

1.9.5 Results

For comparison, the results for $\frac{\partial f}{\partial y}$ along $y = -5$ and $\frac{\partial f}{\partial z}$ along $y = 0$ are shown in Figs. 1.18 and 1.19. Results show that all three methods deliver oscillations larger than for the regular distribution of particles and the deviation from the analytic solution is not satisfactory. In Fig. 1.20, the moving average smoothing method, introduced in Sec. B.9, is applied to the results of the LP interpolation method. The comparison of the results shows that the quality of interpolation after smoothing the results is improved. However, the deviation of the smoothed result from the analytic solution is still noticeable and cannot be neglected.

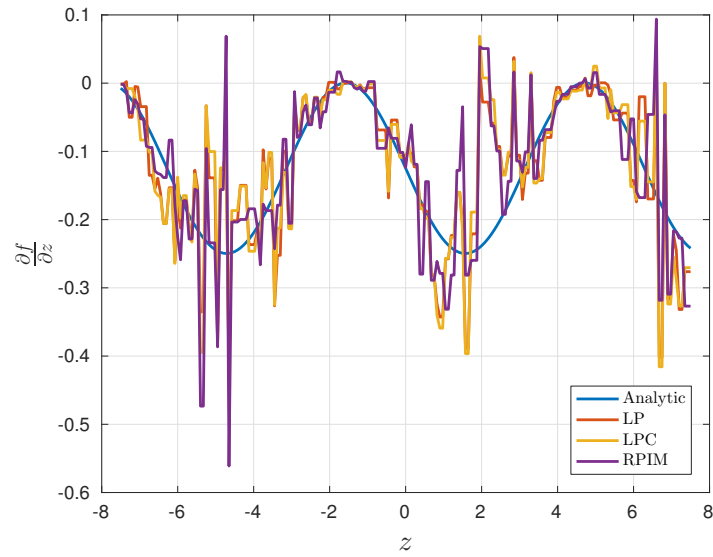


Figure 1.19: Derivative of function f with respect to z along $y = 0$

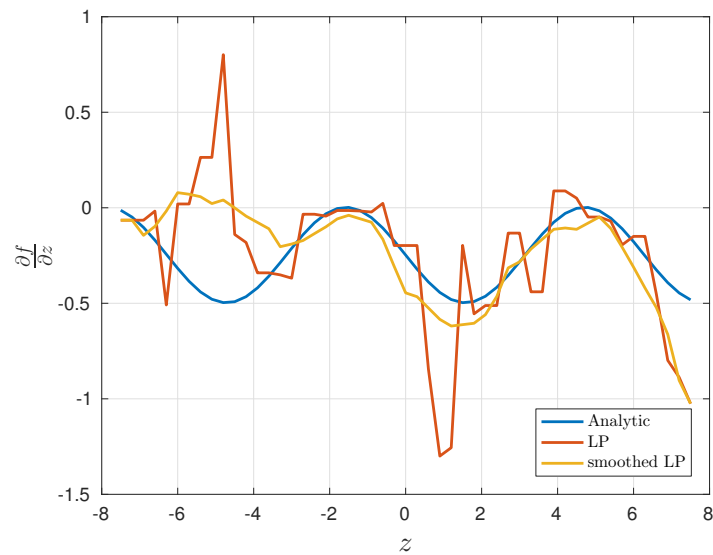


Figure 1.20: Comparison of derivative of function f with respect to z along $y = 0$ for LP and smoothed LP (by applying moving average smoothing method explained in Sec. B.9)

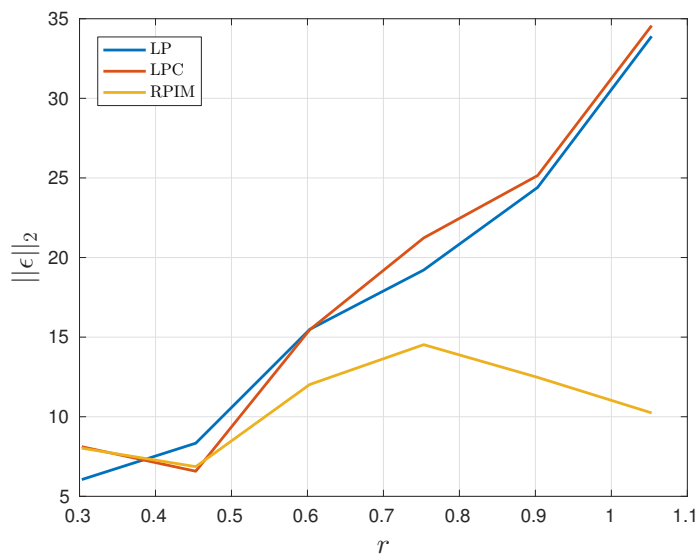


Figure 1.21: Effect of increasing radius of support size, r , on the Euclidean norm of absolute error, $r = 0.3$ is equal to $1 \cdot d$ and $r = 1.1$ is equal to $3.6 \cdot d$, where d is the average grid space

1.9.6 Effect of support size

In a further investigation of the interpolation methods, the norms of the error as explained in Sec. 1.9.3 are compared for an increasing neighbor search radius (r). For this comparison the regular distribution of particles as explained in Sec. 1.9.1 is used. The radius of neighbor search is varied from $r \approx 0.3$ to 1.1 (see Figs. 1.21 and 1.22), which is equal to a grid space (average distance between two adjacent particles) of $d \approx 1$ to 3.6.

Figs. 1.21 and 1.22 show that for LP and LPC the error grows with increasing search radius (equal to more neighboring particles). On the other hand, RPIM shows a different behavior and the errors decrease generally with increasing number of neighboring particles. Although the error decreases for RPIM with increasing number of neighbors, the obtained error does not become smaller than that for LP with small number of neighboring particles. It must be also noted, that increasing number of neighboring particles is associated with longer calculation time. Therefore, as discussed at the beginning of this chapter, the LP interpolation method with the least number of neighboring particles has proved so far to be the most accurate and the fastest interpolation method with smoother results.

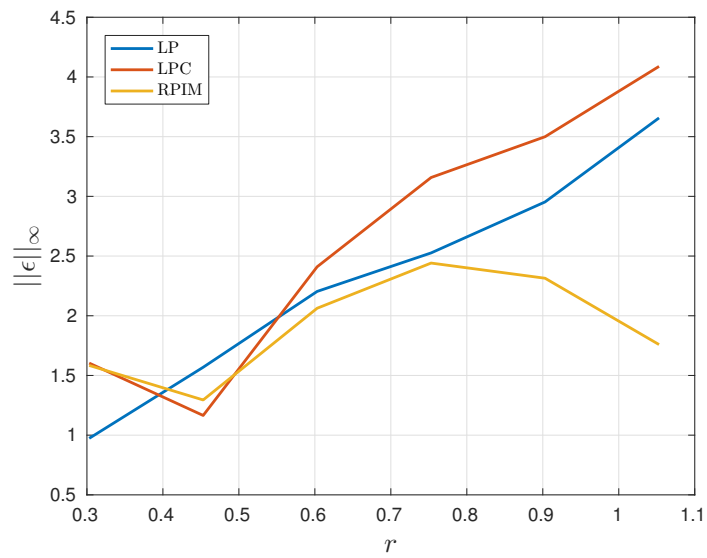


Figure 1.22: Effect of increasing radius of support size, r , on the Chebyshev norm of absolute error, $r = 0.3$ is equal to $1 \cdot d$ and $r = 1.1$ is equal to $3.6 \cdot d$, where d is the average grid space

2 Investigations with SPARC

The Soft PARTicle Code (SPARC) was firstly applied by Chen [11] for simulation of conventional laboratory tests (oedometer and triaxial tests). Chen has used for his simulations the linear polynomials with regularly distributed particles and a fixed-radius research method. Chen has conducted the simulation of the oedometeric test for a cubic sample of $7.5 \text{ cm} \times 7.5 \text{ cm} \times 7.5 \text{ cm}$ with 64, 125 and 343 particles and a constant upper plate velocity $v_p = 10^{-2} \text{ m/s}$.

For the simulation of the triaxial test, Chen has simulated a cylindrical sample with radius of 5 cm and height of 20 cm with a total number of 444 particles. The end plates have been simulated frictionless (leading to homogeneous deformation) and with adherent end plates (leading to inhomogeneous deformation). Chen has mentioned that for the simulation with frictionless plates, the solver had difficulties finding the solution after an axial strain of about 5%. However, for the simulation with the fixed plate an axial strain of 13% has been achieved and afterwards the simulation has not been possible even for very small time increment $\Delta t = 10^{-7}$. Since Chen has applied the arc-length solver method for his simulations, the velocity of the upper plate is not constant throughout the simulation and v_p is varied by the solver until a solution is found. The same as for the oedometer test, he has conducted the simulation only for a dense sample with an initial void ratio $e_0 = 0.62$.

In this chapter a parameter study for triaxial and oedometer is conducted by the author for SPARC. The oedometer test and triaxial tests are simulated with SPARC for dense and loose samples. The number of particles and the upper plate velocity for both tests are varied and the behavior of the solver is investigated for different number of particles and different upper plate velocities. The contents of Secs. 2.1 to 2.6 are adapted from I. Michel, I. Bathaeian et al. [38]¹. In the aforementioned publication the results are also compared with another meshfree method introduced in Ostermann et al. [41], and the weaknesses and strengths of each method are discussed.

2.1 Laboratory tests

The oedometeric and triaxial tests and their corresponding setups are described in this section. These setups are the basis of the case studies. For SPARC the influence of the most important parameters is analyzed with respect to quality and the ability to reproduce the element test for loose and dense samples. The results of the respective element tests are used as reference. The evaluation of stress and strain components (T_{yy} , T_{zz} , ϵ_{zz} and ϵ_v) for

¹GEM - International Journal on Geomathematics by Springer Berlin Heidelberg. Reproduced with permission of Springer Berlin Heidelberg in the format Thesis/Dissertation via Copyright Clearance Center.

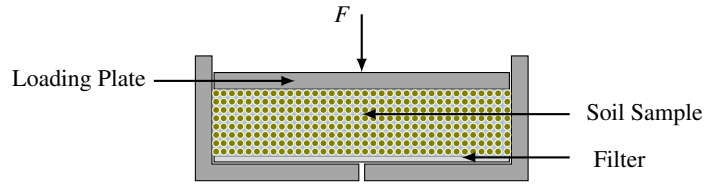


Figure 2.1: Schematic illustration of the oedometric test

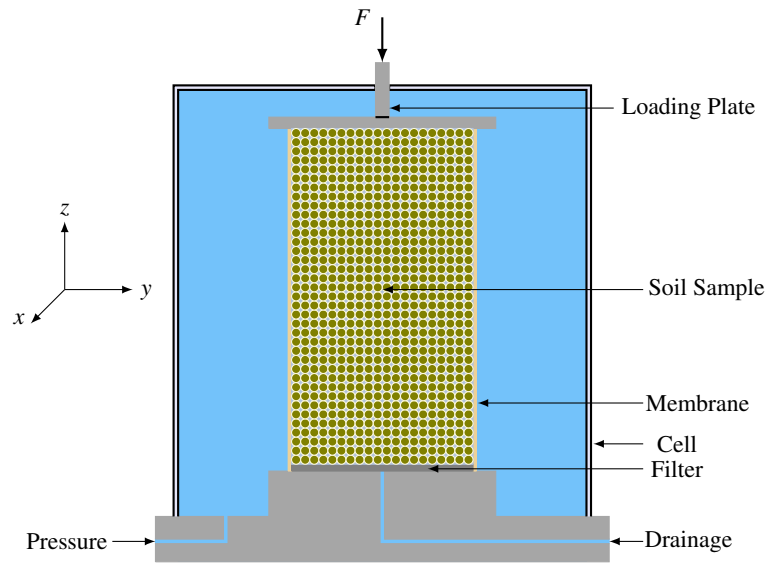


Figure 2.2: Schematic illustration of the triaxial test

plotting the results is presented in Sec. 2.3, including the specific simulation setups for laboratory tests.

As described in Ostermann et al. [41], two popular benchmark problems in soil mechanics are the oedometric and the triaxial test. The oedometric one a confined compression test. The soil sample is loaded in axial direction and rigid side walls hinder any lateral expansion (see Fig. 2.1). In contrast to this, in a conventional triaxial test the soil sample is enclosed in a thin rubber membrane and placed between two plates inside a pressure chamber. The sample is then loaded in axial direction by the stress component T_{zz} and by constant lateral stresses $T_{yy} = T_{xx}$, which is denoted as confining pressure σ_c , (see Fig. 2.2)².

The measurements for the oedometric test refer to a sample of Hostun sand with height of 2.5 cm and diameter of 9.45 cm. Details can be found in [24]. In the oedometric tests the height of the sample is kept small in order to reduce lateral friction effects. We consider both a dense and a loose sample according to Tab. 2.1. Note that in reality oedometric tests are often stress-controlled, i.e. a particular force is applied to the loading plate and the deformations are measured over the course of time. Subsequently, the strains are

²Simulations of Secs. 2.1 to 2.6 are conducted in 3D, (x, y, z) space with $T_{yy} = T_{xx}$.

	dense sample	loose sample
initial void ratio	$e = 0.66$	$e = 0.87$
initial density	$\rho = 1590 \frac{\text{kg}}{\text{m}^3}$	$\rho = 1416 \frac{\text{kg}}{\text{m}^3}$

Table 2.1: Setup for oedometric tests

	dense sample	loose sample
initial void ratio	$e = 0.63$	$e = 0.84$
initial density	$\rho = 1623 \frac{\text{kg}}{\text{m}^3}$	$\rho = 1436 \frac{\text{kg}}{\text{m}^3}$
confining pressure	$\sigma_c = 100 \text{ kPa}$	$\sigma_c = 100 \text{ kPa}$

Table 2.2: Setup for triaxial tests

calculated from the recorded plate displacements. However, in our simulations the oedometric test is simulated strain-controlled. For the triaxial test we consider a cylindrical soil sample of Hostun sand with height and diameter of 10 cm, see [24]. The setup is given in Tab. 2.2.

2.2 Material model

For the simulations of this study, the barodetic material model after Kolymbas (2011) [29] is implemented in SPARC. The material model is explained in details in Sec. A.2.1. The calibration of the constants for Hostun sand is offered in Tab. A.1.

2.3 Setup and evaluation

The case studies for SPARC in Secs. 2.4 and 2.5, respectively, are based on the following simulation setups independent of the test type and the sample type:

simulation setup I – constant upper plate velocity and varying number of particles

simulation setup II – fixed number of particles and varying upper plate velocity

In order to compare the 3D simulations with the corresponding element test, the necessary 1D stress-strain-curves and stress paths are generated by averaging the considered quantity over all particles at the loading plate. The ε_v vs. ε_{zz} are generated by averaging the volume change over each particle of the simulated soil sample to accommodate the volumetric character. Note that a consistent comparison of the results is guaranteed by considering the axial strain in logarithmic form, since for the calculation of ε_{zz} of the element test, the D_{zz} component of stretching tensor is directly integrated. The relation between logarithmic and engineering strain is,

$$\varepsilon_{zz}^{\text{log}} = \ln(1 + \varepsilon_{zz}^{\text{eng}}), \quad (2.1)$$

	simulation setup	n_p	v_p ($\frac{m}{s}$)	Δt (s)	$\Delta t \cdot v_p$ (m)
dense sample	I	147	∓ 0.001	0.0025	$\mp 2.5 \cdot 10^{-6}$
		1125	∓ 0.001	0.0025	$\mp 2.5 \cdot 10^{-6}$
		3703	∓ 0.001	0.0025	$\mp 2.5 \cdot 10^{-6}$
	II	1125	∓ 0.01	0.0025	$\mp 2.5 \cdot 10^{-5}$
		1125	∓ 0.001	0.0025	$\mp 2.5 \cdot 10^{-6}$
		1125	∓ 0.0001	0.0025	$\mp 2.5 \cdot 10^{-7}$
loose sample	I	147	∓ 0.001	0.0025	$\mp 2.5 \cdot 10^{-6}$
		1125	∓ 0.001	0.0025	$\mp 2.5 \cdot 10^{-6}$
		3703	∓ 0.001	0.0025	$\mp 2.5 \cdot 10^{-6}$
	II	1125	∓ 0.01	0.001	$\mp 1.0 \cdot 10^{-5}$
		1125	∓ 0.001	0.001	$\mp 1.0 \cdot 10^{-6}$
		1125	∓ 0.0001	0.001	$\mp 1.0 \cdot 10^{-7}$

Table 2.3: Simulation parameters for the oedometric test

where,

$$\epsilon_{zz}^{\text{eng}} = \frac{\Delta h}{h_0}, \quad (2.2)$$

where Δh and h_0 are the amount of deformation in the height and initial height of the sample, respectively.

2.4 Oedometric test

In Tab. 2.3, the simulation parameters for the oedometric test are summarized. For both the dense and the loose sample we consider a constant upper plate velocity $v_p = \pm 0.001$ m/s and three different numbers of particles (simulation setup I). Furthermore, simulations for the medium number of particles $n_p = 1125$ and three upper plate velocities are analyzed (simulation setup II). Due to the applied boundary conditions and the homogeneous deformation, convergence of Newton solver is achieved relatively easy.

2.4.1 Dense sand

The 3D simulations for simulation setup I show a very good agreement with the element test (see Fig. 2.3). Since the deformation is homogeneous, the number of particles has no influence on the accuracy. Therefore, the curves for the different resolutions almost perfectly fit to the curve of the element test. The results for simulation setup II are illustrated in Fig. 2.4. Only in case of upper plate velocity $v_p = \mp 0.01 \frac{m}{s}$ a slight deviation from the element test can be observed. This is due to the fact that the time step size Δt

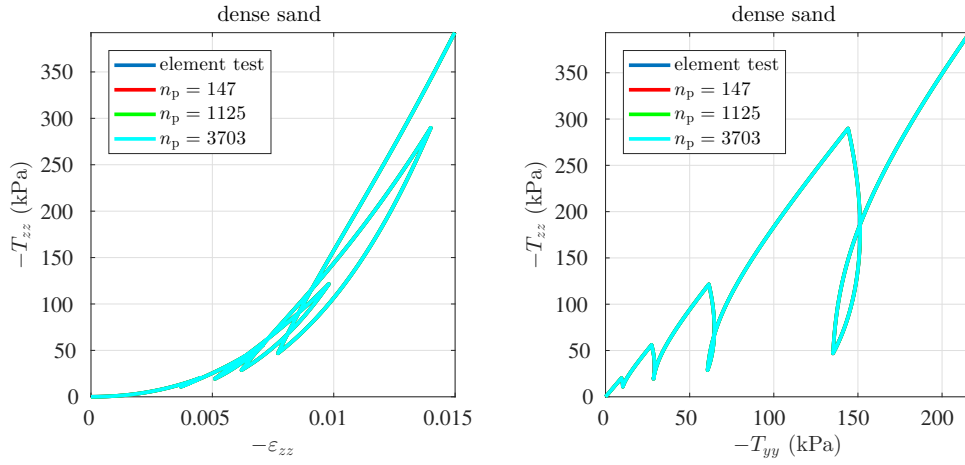


Figure 2.3: *Dense oedometric test* – Comparison of element test and 3D simulations for simulation setup I: stress-strain-curve (a) and stress path (b), the curves are coincident and the colors cannot be distinguished

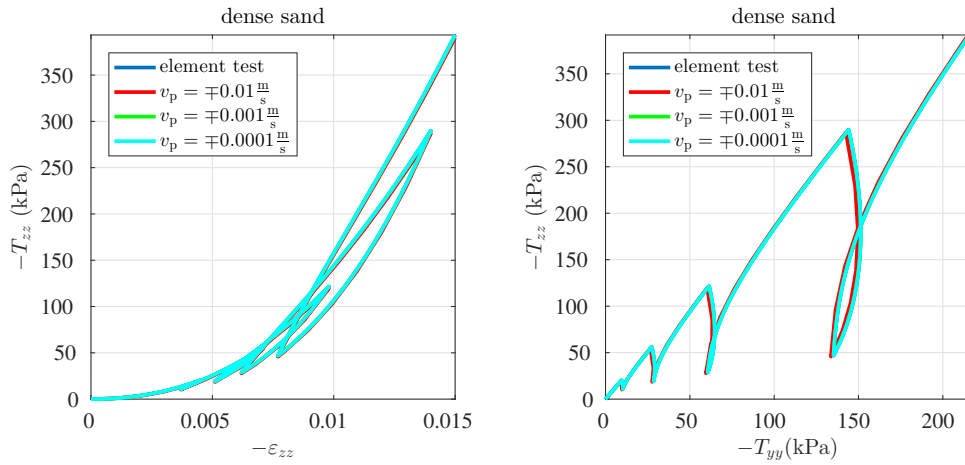


Figure 2.4: *Dense oedometric test* – Comparison of element test and 3D simulations for simulation setup II: stress-strain-curve (a) and stress path (b) the curves are coincident and the colors cannot be distinguished

is kept constant for all v_p . Adapting the time step size such that the product $\Delta t \cdot v_p$ is constant would lead to an even better agreement for $v_p = \mp 0.01 \frac{m}{s}$.

2.4.2 Loose sand

As before, the 3D simulations are in very good agreement with the element test for loose sand considering varying particle numbers (simulation setup I), cf. Fig. 2.5. However, SPARC encounters convergence difficulties for loose sand in case of $v_p = \mp 0.01 \frac{m}{s}$ and $\Delta t = 0.0025$ s after the first unloading at axial strain $-\varepsilon_{zz} = 0.01$. Due to the change

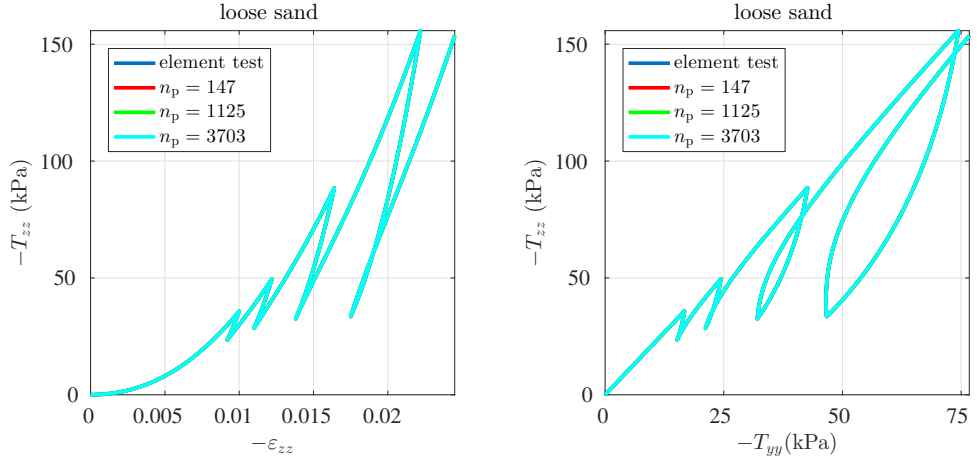


Figure 2.5: *Loose oedometric test* – Comparison of element test and 3D simulations for simulation setup I: stress-strain-curve (a) and stress path (b), the curves are coincident and the colors cannot be distinguished

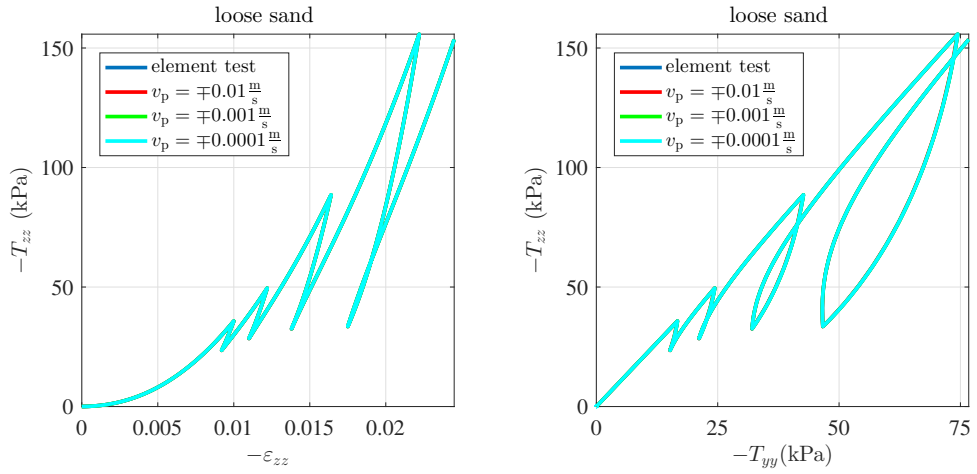


Figure 2.6: *Loose oedometric test* – Comparison of element test and 3D simulations for simulation setup II: stress-strain-curve (a) and stress path (b), the curves are coincident and the colors cannot be distinguished

from loading to unloading, the initial guess of the solution, which is inherited from the previous time step, becomes an inadequate choice. In order to guarantee convergence of the Newton solver, Δt is incrementally reduced until convergence is achieved with $\Delta t = 0.001$ s. This value is used for all three simulations with varying v_p , i.e. simulation setup II (see Fig. 2.6).

2.5 Triaxial test

The triaxial test is characterized by fixed vertical velocity at the upper plate and prescribed confining pressure at the membrane. The boundary conditions make the convergence of the Newton solver difficult or sometimes even impossible. Consequently, SPARC is very sensitive to the number of particles n_p , the loading rate v_p , and the time step size Δt .

Another important factor is the mode of constraint of particles in x - and y -directions. To illustrate the influence of this factor, we consider a dense sample where the particles located on the symmetry line are set free to move in x - and y -directions. The results of this *unconstrained* simulation can be seen in Fig. 2.7. However, the assumption of frictionless plates does not necessarily correspond to reality. Usually, filter stones with rough surfaces are located at the center of the sample on both plates to prevent the sample from sliding horizontally during the experiment (even if the plates are lubricated). The high degree of freedom results in convergence problems in the Newton solver even before the localization of deformation³. This ultimately leads to the abortion of the simulation at maximum axial strain of $-\varepsilon_{zz} = 0.18$. Therefore, for the following SPARC simulations the motion of particles located on the symmetry line is constrained in both horizontal (x and y)-directions, while the other particles are set free to move in all directions.

The simulation parameters for the triaxial test are summarized in Tab. 2.4, where $(-\varepsilon_{zz})_{\max}$ denotes the maximum axial strain reached during the respective simulation. Again, for both the dense and the loose sample simulations with reference loading rate $v_p = -0.001 \frac{\text{m}}{\text{s}}$ and three different numbers of particles are considered (simulation setup I). Moreover, rate-independence is investigated (simulation setup II).

Dense sand

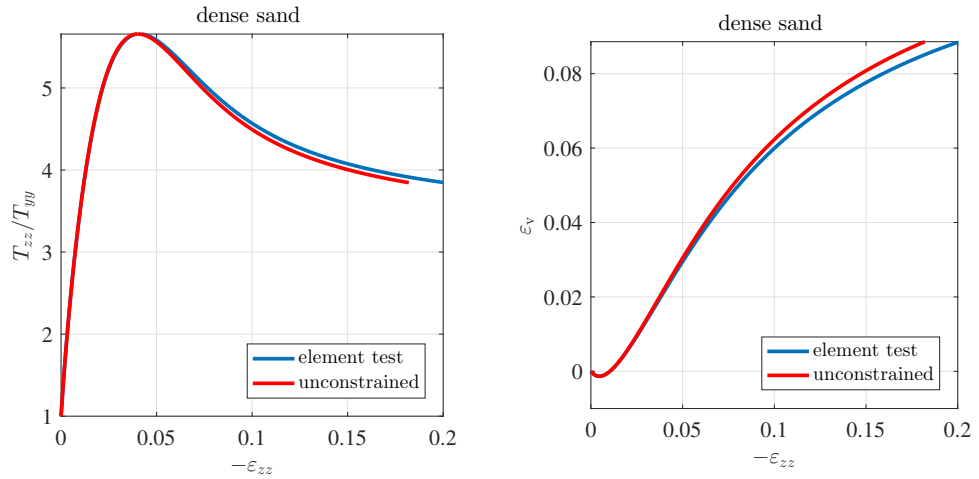
The illustration of the results for simulation setup I in Fig. 2.8 reveals that the larger the number of particles is, the earlier SPARC encounters convergence problems. In general, good agreement with the element test is achieved before the stress peak. Minor deviations can be observed after the peak.

Convergence problems are already encountered in the first time step in case of $v_p = -0.01 \frac{\text{m}}{\text{s}}$ and $\Delta t = 0.4$ s. Therefore, Δt was gradually reduced to $\Delta t = 0.06$ s until convergence is achieved. In Fig. 2.9, the results for simulation setup II are presented. It is obvious that the smaller the loading rate is (in the sense of absolute value), the earlier SPARC diverges: For $v_p = -0.001 \frac{\text{m}}{\text{s}}$ SPARC diverges right after the stress peak, whereas for $v_p = -0.0001 \frac{\text{m}}{\text{s}}$ even the peak of the stress-strain-curve is not reached. In case of small loading rates the numerical errors accumulate to such an extent that convergence of the Newton solver is difficult or even impossible.

³Localization of deformation means that with increasing loading the deformation of a solid body localizes in narrow zones which gradually develop to shear bands. This occurs when the stiffness approaches zero. Vanishing stiffness leads to an ill-posed initial boundary value problem inducing convergence problems in the Newton solver. For further details see [47].

	simulation setup	n_p	$v_p \left(\frac{m}{s}\right)$	Δt (s)	$\Delta t \cdot v_p$ (m)	$(-\epsilon_{zz})_{max}$
dense sample	I	222	-0.001	0.4	$-4.0 \cdot 10^{-4}$	0.2
		441	-0.001	0.4	$-4.0 \cdot 10^{-4}$	0.16
		567	-0.001	0.4	$-4.0 \cdot 10^{-4}$	0.11
	II	441	-0.01	0.06	$-6.0 \cdot 10^{-4}$	0.08
		441	-0.001	0.06	$-6.0 \cdot 10^{-5}$	0.05
		441	-0.0001	0.06	$-6.0 \cdot 10^{-6}$	0.02
loose sample	I	222	-0.001	0.4	$-4.0 \cdot 10^{-4}$	0.2
		441	-0.001	0.4	$-4.0 \cdot 10^{-4}$	0.12
		567	-0.001	0.4	$-4.0 \cdot 10^{-4}$	0.05
	II	441	-0.01	0.05	$-5.0 \cdot 10^{-4}$	0.10
		441	-0.001	0.05	$-5.0 \cdot 10^{-5}$	0.10
		441	-0.0001	0.05	$-5.0 \cdot 10^{-6}$	0.01

Table 2.4: SPARC simulation parameters for the triaxial test

Figure 2.7: Comparison of element test and 3D simulation for the *unconstrained* triaxial test with dense sand ($n_p = 259$, $v_p = -0.01 \frac{m}{s}$, and $\Delta t = 0.01$ s): stress-strain-curve (a) and volumetric-axial-strain-curve (b)

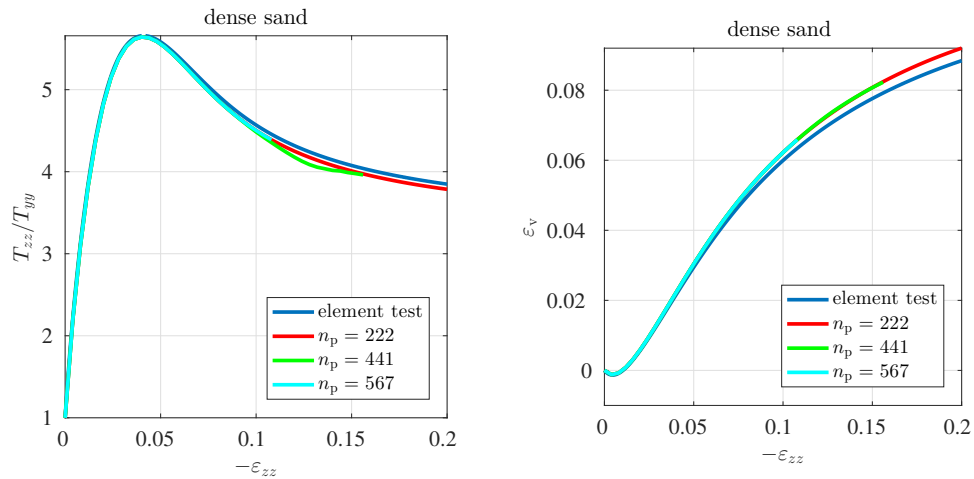


Figure 2.8: *Dense triaxial test* – Comparison of element test and 3D simulations for simulation setup I: stress-strain-curve (a) and volumetric-axial-strain-curve (b)

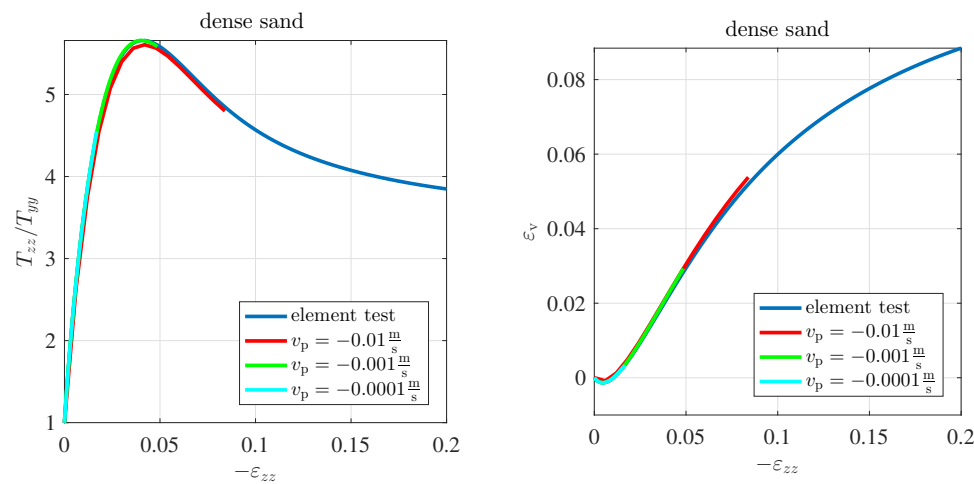


Figure 2.9: *Dense triaxial test* – Comparison of element test and 3D simulations for simulation setup II: stress-strain-curve (a) and volumetric-strain-curve (b)

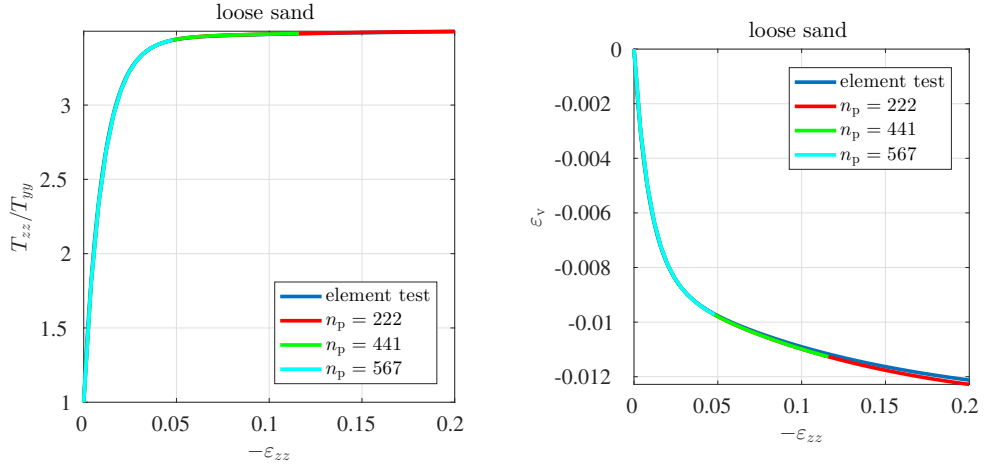


Figure 2.10: *Loose triaxial test* – Comparison of element test and 3D simulations for simulation setup I: stress-strain-curve (a) and volumetric-axial-strain-curve (b)

Loose sand

The results for loose sand with simulation setup I are illustrated in Fig. 2.10. As for the dense sample, the larger the number of particles is, the earlier SPARC encounters convergence problems (compare $(-\varepsilon_{zz})_{\max}$ in Tab. 2.4). Nevertheless, the 3D simulations agree well with the element test before and slightly after the plateau of the stress-strain-curve. As before, for the highest loading rate (in the sense of absolute value) $v_p = -0.01 \frac{\text{m}}{\text{s}}$ convergence problems can be observed for large time step sizes. Therefore, Δt is incrementally reduced to $\Delta t = 0.05$ s until convergence is achieved for simulation setup II. In Fig. 2.11, it can be observed that the smaller the loading rate is, the earlier SPARC diverges. For $v_p = -0.01 \frac{\text{m}}{\text{s}}$ and $-0.001 \frac{\text{m}}{\text{s}}$ SPARC diverges at almost $-\varepsilon_{zz} = 0.1$. For $v_p = -0.0001 \frac{\text{m}}{\text{s}}$ even the plateau of the stress-strain-curve is not reached. This is again due to the accumulation of numerical errors for small loading rates v_p .

2.6 Discussion of results

As long as deformations are homogeneous, the 3D simulations are in agreement with the element test. Although the Newton solver suffers from convergence problems for specific number of particles or upper plate velocities, especially in the softening regime, SPARC is capable of modeling triaxial tests beyond the stress peak if the appropriate parameters are chosen. However, the parameter study shows that SPARC is very sensitive to the number of particles and the velocity of the upper plate. In case of large number of particles, the simulation breaks even before the peak of stress is achieved. Furthermore, small upper plate velocities cause problems for the solver and the simulation breaks after a small axial strain $-\varepsilon_{zz} = 0.01$ has been reached.

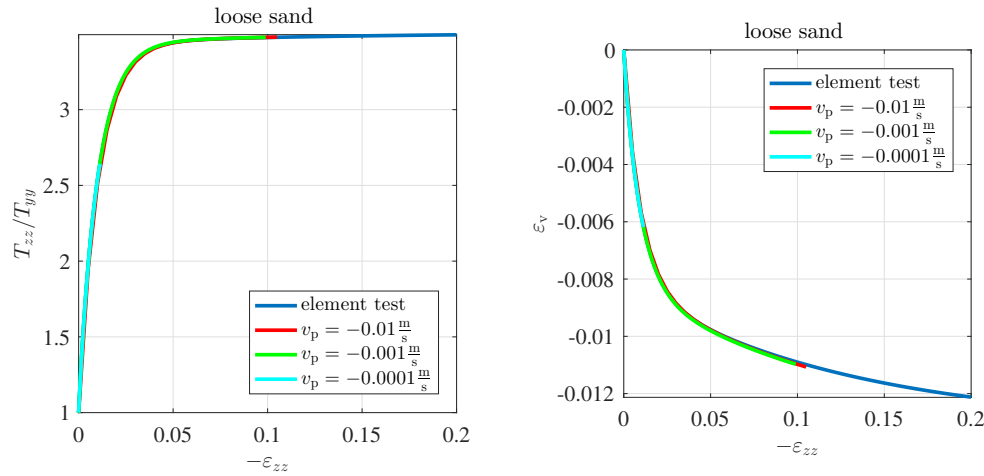


Figure 2.11: *Loose triaxial test* – Comparison of element test and 3D simulations for simulation setup II: stress-strain-curve (a) and volumetric-strain-curve (b)

2.7 Simulation of shear bands in clay

Simulation of shear bands with SPARC for *sand* was first conducted by Chen [11]. For the simulations, Chen implements the barodetic material model after Kolymbas (2011) [25] with the calibration for Hostun sand. The material model and the calibration of the constants are explained in Sec. A.2.1 and Tab. A.1, respectively. For the simulations, Chen discretizes the continuum with 231 regular particles and conducts the simulation for a dense sample with initial void ratio $e_0 = 0.63$. Chen also conducts a parameter study, regarding the initially irregular distribution of particles and discusses that in case of irregular particles, strain localization can be simulated but no shear bands can be detected. Furthermore, Chen adds that although using irregular allocated particles is one of the main goals of meshfree methods, the performance of SPARC with irregularly distributed particles is much worse than with regularly distributed ones.

In the following we present the development, thickness and orientation of shear bands in clay in biaxial tests with the boundary conditions introduced in Sec. 1.3. As for the material model, the barodetic material model for clay after Medicus and Fellin (2017), [37] with the calibration for Dresden clay is implemented in SPARC. A detailed description of the material model with its calibration procedure is offered in Sec. A.2.4 and Tab. A.4, respectively. The contents of Secs. 2.7 to 2.11 are adapted from the publication, *Simulation of Shear Bands with Soft Particle Code (SPARC) and FE, in GEM - International Journal on Geomathematics* [47]⁴.

In the publication [47], the results of the simulation with SPARC are also compared for the same initial conditions with the results of Finite Element method (FE), however, in the following only the results of SPARC are presented. Furthermore, the parameters of Mohr-Coulomb failure criterion are determined, so as to compare the orientation of shear bands with the analytical solution.

⁴GEM - International Journal on Geomathematics by Springer Berlin Heidelberg. Reproduced with permission of Springer Berlin Heidelberg in the format Thesis/Dissertation via Copyright Clearance Center.

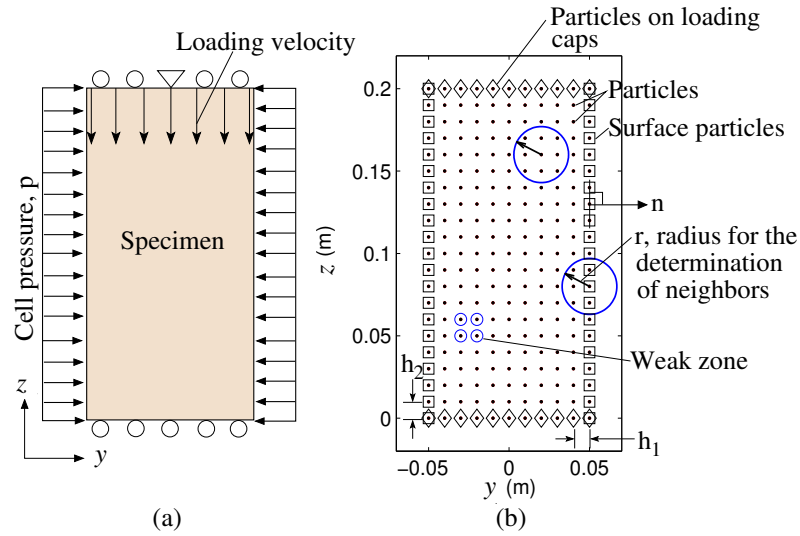


Figure 2.12: Illustration of (a) boundary conditions and (b) particles representing the study domain

2.8 Simulation setup

A biaxial test can be regarded as a plane strain adaption of a triaxial test, to show shear localization in a 2D numerical setup. The deformation is driven by two lubricated loading caps on the top and the bottom of the specimen. The upper cap moves downward compressing the specimen. On the lateral boundaries, the constant traction of p is applied (see Eq. 1.2). The resulting boundary conditions are illustrated in Fig. 2.12 a. In our simulations, the initial void ratio $e_0 = 0.45$ under a cell pressure $p = 100$ kPa, corresponding to a dense sample, is adopted. Therefore, a peak in the stress-strain relationship with post-peak strain-softening, strain localization or formation of shear band(s) in the biaxial test simulation are to be expected. The particle configuration is shown in Fig. 2.12 b. The surface particles are subjected to cell pressure p . Velocity components v_z of particles on loading caps are prescribed, whereas v_y is unknown. Note that in order to prevent the specimen from horizontal translation, the velocity component $v_y = 0$ for the particle in the middle-top of the sample is prescribed.

Two simulation examples, with and without imperfection in the specimen, are presented in the following. The imperfection is implemented by increasing the void ratio of the particles representing a weak zone (Fig. 2.12 b) by 0.02, resulting in relatively looser state and thus lower stiffness. Given a weak zone, the formation of shear bands is expected to initiate from the weak zone. In order to investigate the dependency of the shear bands, simulated by SPARC, on the number of particles, three sets of simulations with initially homogeneous setup for three number of particles, $n_p = 180, 231$ and 299 were conducted. Simulation with an implemented imperfection were done only for 231 particles. All simulations are summarized in Tab. 2.5.

Method	Setup	n_p		
SPARC	homogeneous	180	231	299
	imperfection	-	231	-

Table 2.5: Summary of simulations

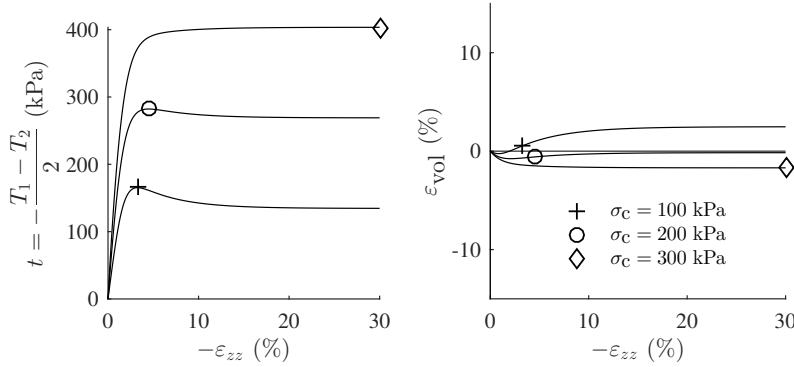


Figure 2.13: Element test with barodesy for clay, a) stress-strain curve b) volumetric behavior

2.9 Mohr-Coulomb vs. barodesy

The analytical solutions addressing the orientation of shear bands for granular materials, are based on two conventional soil parameters, friction angle φ and dilatancy angle ψ (see Sec. 2.10.3 for detailed discussion). Element simulation of triaxial test with barodesy for clay for three consolidation pressures ($\sigma_c = 100$ kPa, 200 kPa and 300 kPa) were conducted and the results are presented in Fig. 2.13. Where T_1 and T_2 are the principal stress components⁵. The acquired values achieved from the element tests were applied for determination of friction angle φ and cohesion c according to Mohr-Coulomb criterion (see Fig. 2.14), which yields a friction angle of $\varphi = 32.9^\circ$ and cohesion of $c = 24.7$ kPa. In order to reproduce almost the same volumetric plastic strains with Mohr-Coulomb, a dilatancy angle of $\psi = 7.3^\circ$ was assumed. Stress-strain curves and volumetric behavior with linear-elastic, perfect-plastic Mohr-Coulomb are plotted Fig. 2.15.

2.10 Results

2.10.1 Simulations with initially homogeneous fields

Since the initial stress field and void ratio field are homogeneous, the deformation in the sample shall be homogeneous, meaning that the stress strain curve of all particles must be identical and must overlap with the curve obtained from element test result. The constitutive model barodesy for clay is used to obtain the stress strain curve by

⁵Since the calibration of Mohr-Coulomb parameters, is conducted in axisymmetric conditions, therefore, $T_2 = T_3$. However, the biaxial test has plane strain conditions, by which $T_2 = T_3$ does not hold.

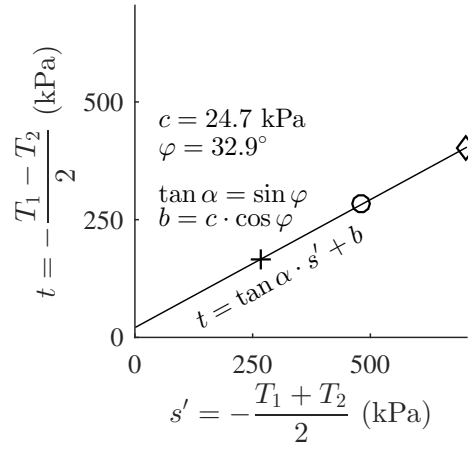


Figure 2.14: Mohr-Coulomb criterion for determination of friction angle φ and cohesion c

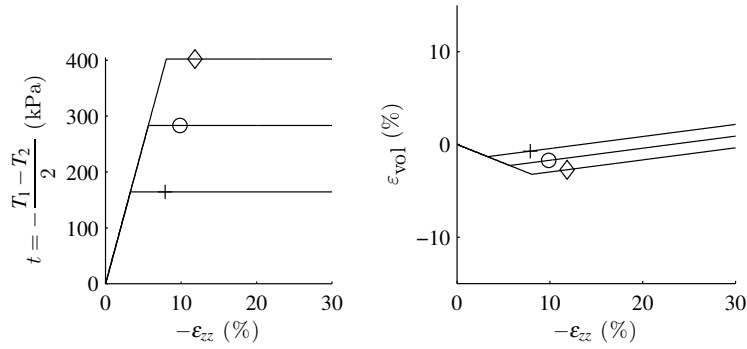


Figure 2.15: Simulation with Mohr-Coulomb for $\varphi = 32.9^\circ$, $c = 24.7$ kPa, $E = 10$ MPa and $\nu = 0.3$ a) stress-strain b) volumetric behavior for $\psi = 7.3^\circ$

prescribing the deformation matrix,

$$\mathbf{D} = \begin{bmatrix} 0 & 0 & 0 \\ 0 & D_{yy} & 0 \\ 0 & 0 & -1 \end{bmatrix}, \quad (2.3)$$

and using an initial void ratio $e = 0.45$ and stress state $\mathbf{T} = \mathbf{1} \cdot (-100$ kPa). D_{yy} is determined in each time step by satisfying the condition $T_{yy} = 0$ with \dot{T}_{yy} obtained from the constitutive model.

The stress-strain curves of all particles obtained from SPARC simulation are shown in Fig.2.16. The SPARC simulation results show that all curves overlap with one another and with the element test curve until $-\epsilon_{zz} \approx 4.6\%$ is reached. This implies that the deformation of the sample for $-\epsilon_{zz} < 4.6\%$ is homogeneous. Thereafter, the deformation starts to localize at particles, the localization causes numerical error and the continuation of simulation leads to the accumulation of the error. When the axial strain ($-\epsilon_{zz}$)

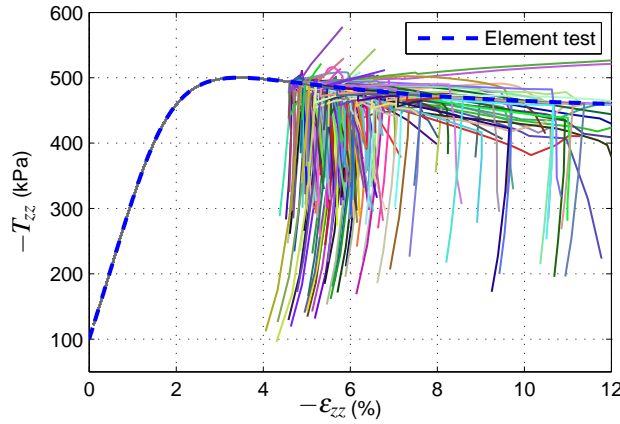


Figure 2.16: Stress-strain curves ($T_{zz} - \varepsilon_{zz}$) of all particles in SPARC, the blue dashed line is the result of an element test

approaches 4.6% deformations start to localize and as it can be seen in (Figs.2.18 a and 2.19 a) at $-\varepsilon_{zz} = 6.2$, shear bands in "V" form are formed in the middle bottom of the model. The void ratio field after localization in Fig. 2.18 a, shows that contraction occurs in the whole sample. However, when deformations start to localize, the void ratio in the shear bands exhibit volumetric increases (see Fig.2.18 a). This trend is expected to occur in a dense granular sample with strain softening behavior.

2.10.2 Simulations with imperfection implemented

The stress strain curves in terms of σ_{zz} and ε_{zz} obtained by SPARC are plotted in Fig. 2.17. For $-\varepsilon_{zz} < 2.0\%$ all curves except for those of particles in the weak zone are in good agreement with those of the element test curve. At $-\varepsilon_{zz} \approx 2.3\%$, strains start to localize significantly in a shear band initialized by the weak zone. Thereafter, strains occur mainly in the shear band. The initial shear band is followed by some other shear bands (see Figs. 2.18 b and 2.19 b) before the program aborts. At this point the solver cannot find any solution even with an extremely small time-steps $\Delta t < 10^{-10}$. The void ratio field in Fig. 2.18 b, shows that contraction occurs in the whole sample, however, once the deformations start to localize, the changes in the void ratio of the shear band show a dilatant behavior.

2.10.3 Orientation and thickness of the shear bands

Vermeer [57] conducted theoretical and experimental investigations on the orientation θ and thickness of shear bands in biaxial tests, his investigations show that for fine sand, the orientation of shear bands coincides almost the Mohr-Coulomb solution $\theta = 45^\circ + \varphi/2$ is observed. Where φ is the friction angle. Investigations of Hand and Drescher [20] explain the dependency of the shear bands on the magnitude of the confining pressure. As mentioned in Han and Drescher [20], the shear band inclination angle with respect to the minor principal stress decreases when the confining pressure increases, however, the shear strains increase. Experimental results of Hand and Drecher [20], have shown that

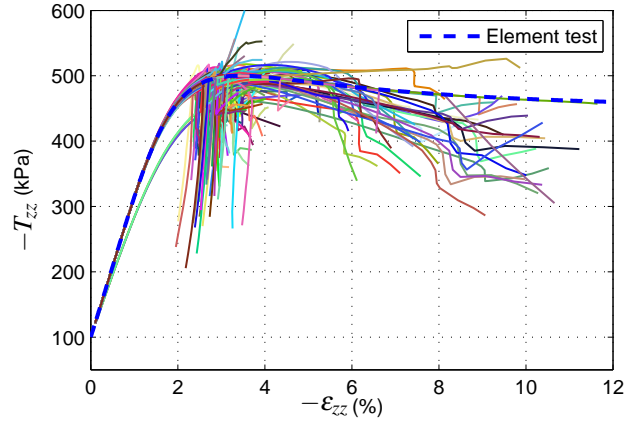


Figure 2.17: Stress-strain curves ($T_{zz} - \varepsilon_{zz}$) of all particles in simulations with imperfection implemented in SPARC, the blue dashed line is the result of an element test

at higher confining pressures (almost 400 kPa), the shear band inclination is in general much lower than the one predicted by Mohr-Coulomb. The acquired inclination angle with SPARC is about 39.8° for the test with initially homogeneous sample and about 45.8° for the test with implemented imperfection.

As discussed in Sec. 2.9, a friction angle of $\varphi = 32.9^\circ$ can be attributed to Dresden clay. Considering the solution of Mohr-Coulomb with $\theta = 45^\circ + \varphi/2$, we should be expecting an inclination of $\theta = 61.4^\circ$ which is larger than the the results of SPARC.

As for the thickness and inclination of the shear bands acquired by FE methods using a hypoplastic constitutive model, Tejchman and Wu have shown in [51] that the inclination and thickness of the shear band are dependent on the spatial discretization. In a further investigation, Tejchman and Bauer [50] benefit from the results of an extension of the hypoplastic model for polar continuum with a characteristic length, the so-called mean grain diameter d_{50} . Their results show, the thickness of the shear band is the same for a fine and coarse mesh. Tejchman and Bauer also mention in order to realistically simulate the thickness of the shear zone within a polar continuum, the size of the finite element should be smaller than $5 \cdot d_{50}$.

In Figs. 2.19 a, c and d and Figs. 2.18a, c and d, results of SPARC for a homogeneous setup and for different number of particles are presented. As can be seen, for the lower number of 180 particles, shear bands are not clearly formed and deformation seems to localize on the two corners of up-left and down-right. This phenomenon can be so explained, that in case of homogeneous setup, the shear bands appear as a result of the accumulated error in each time-step, and with less number of particles, the accumulation stays smaller which can lead to later appearance of shear bands or no meaningful appearance of shear bands. For more than 231 particles, the shear band has a "V" shape in the middle bottom of the specimen and has a thickness of $5 \cdot d$, where d is the average distance between two particles, while for more than 299 particles (see Figs. 2.18 c and 2.19 c), the shear band is not as thick as by 231 particles and has a thickness of $3 \cdot d$. Furthermore, for 299 particles, shear bands have a symmetric shape not only along y axis, but also along z axis. As for the inclination, the acquired shear bands for more particles

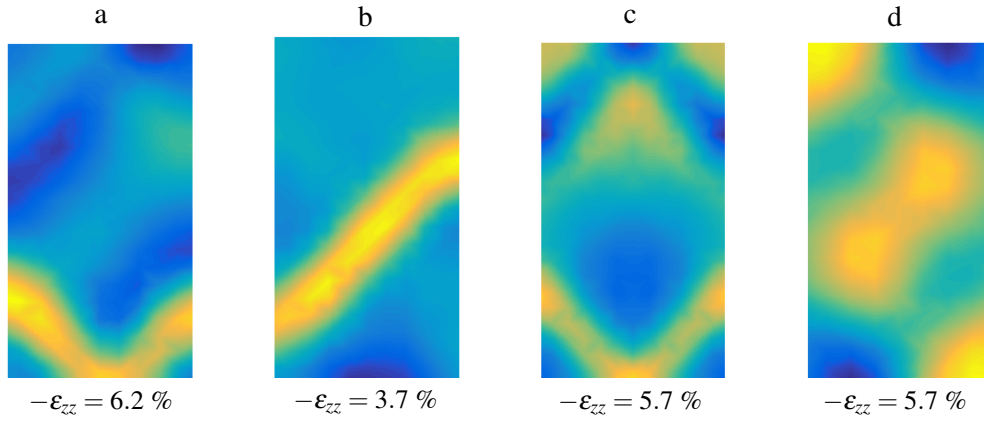


Figure 2.18: Demonstration of shear band in form of void ratio for a) homogeneous, $n_p = 231$ b) with weak zone, $n_p = 231$ c) homogeneous, $n_p = 299$ d) homogeneous, $n_p = 188$

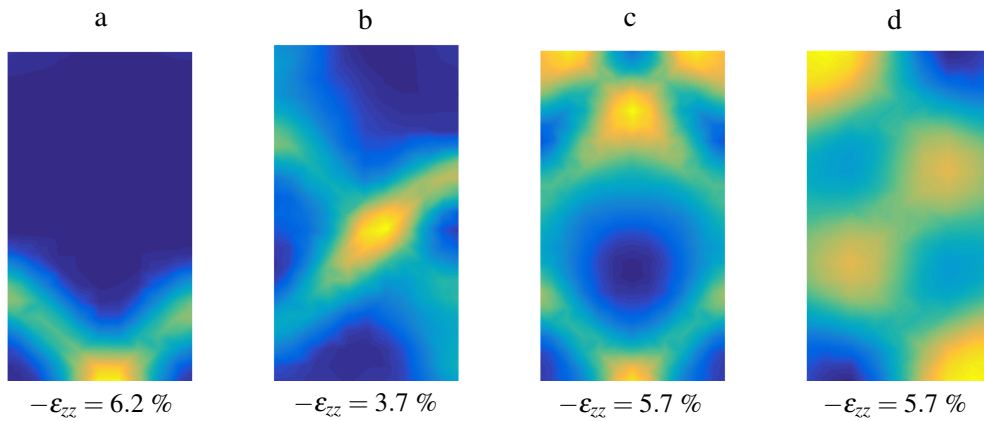


Figure 2.19: Demonstration of shear band in form of $|\mathbf{D}|$ for a) homogeneous, $n_p = 231$ b) with weak zone, $n_p = 231$ c) homogeneous, $n_p = 299$ d) homogeneous, $n_p = 188$

(299) have a slightly larger angle as those acquired for 231 particles. From the acquired symmetric shape, and the larger inclination angle, it can be deduced that for SPARC, the denser the particles, the better the shear bands can be simulated.

2.11 Discussion of results

SPARC uses the strong formulation to solve the differential equations. Therefore, the equilibrium is fulfilled at every single particle with a prescribed tolerance. SPARC is capable of simulating shear bands even when the specimen has an initially homogeneous setup, this can be attributed to the numerical inaccuracy and error accumulation in the

domain. Simulations with different number of particles with SPARC have demonstrated that the density of particles also plays a role in the shape, thickness and orientation of shear bands and the denser the particles, the better the shear bands can be reproduced in the framework of SPARC.

3 Simulation of punching

The simulation of punching into sand was a challenging task for SPARC and could not be easily achieved. The first attempt at simulating punching by solving the Cauchy equation of motion (Eq. 1.1) on the boundaries of the model (walls and bottom) failed and the simulation broke after some time steps. In the second attempt, the idea of exclusion of boundary particles as introduced in Sec. B.6, was implemented. Also this idea did not prove to be effective and the simulation could not continue. Afterwards, the definition of slip boundary condition (Eq. 1.2) on the side walls and the bottom of the model and the tension control as explained in Sec. 1.7 were implemented, which proved to be efficient and the simulation could be continued until the peak of the load-settlement curve (see Fig. 3.12) was reached and afterwards, the convergence of the solver was no more possible. The problem of finding no solution at the peak was finally solved by implementing the idea of reconditioning the solution procedure, explained in Sec. 1.8. The reconditioning procedure needed to be applied over a number of time steps at the peak of the load-settlement curve and afterwards, the solver could continue without reconditioning. Anyway, the simulation could not continue after reaching a relative depth of about $d_p/B \approx 0.2$, where d_p is the penetration depth and B is the width of the foundation, even for very small time steps and the reconditioning of the solution could not help.

3.1 General remarks

In this section, the slide planes (shear bands) and the load-displacement behavior associated with the problem of punching are introduced and the analytically predicted geometry of the slide planes is used for comparison of the numerical results delivered by SPARC (see Sec. 3.3.4).

Kolymbas considers in [29] a circular slide plane as the simplest failure mechanism for the ideal case of friction free soil ($\varphi = 0$). There are more complicated failure mechanisms introduced, however, all methods make simplifying assumptions regarding the soil properties, ideal rigid plastic material, and the development of deformations, formation of a wedge of soil under the foundation. Despite such simplifications, comparisons between model tests and full-size foundations by Heinz [21] demonstrate that the acquired failure mechanism for sand is comparable with real failure mechanism (see Fig. 3.1). Slip planes develop when soil is sheared to failure. However, the rigid foundation hinders formation of any slip plane through the foundation and as a result, no slip plane is formed just below the foundation but only a rigid wedge. The wedge just below the foundation in Fig. 3.2 penetrates into the soil and causes twin zones of shear. In the zones, adjacent to the wedge, shear planes are formed. In the neighboring triangular zone, the

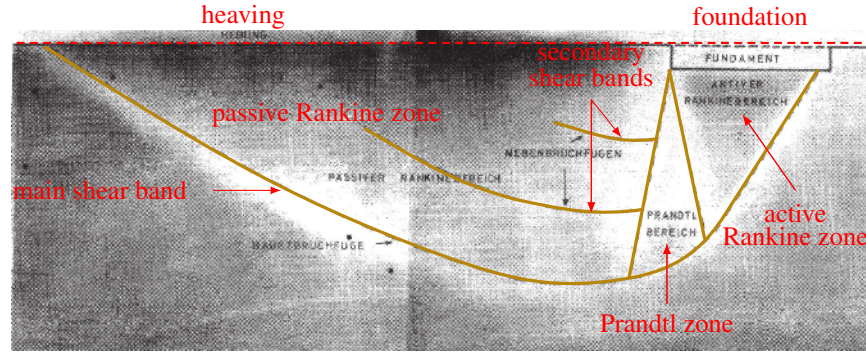


Figure 3.1: X-ray photograph of failure mechanism of dense sand, adapted from Aubram [2], first published in Heinz [21]

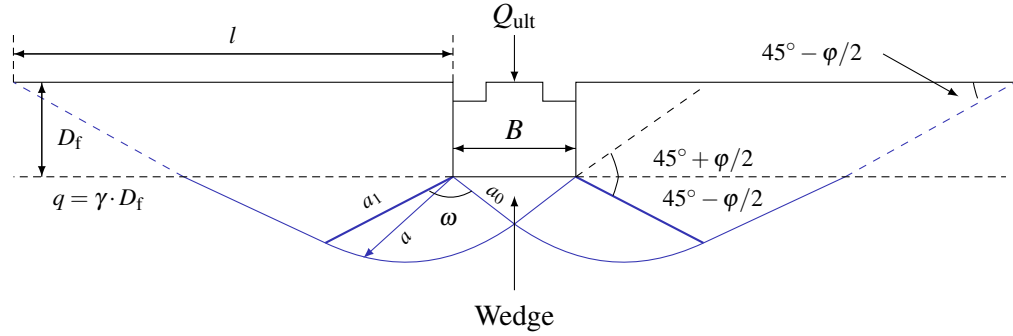


Figure 3.2: Assumed shape of failure of dense sand according to Leonards [33], Budhu [9] and Terzaghi and Peck [52]

so-called Rankine passive zone, shear planes are formed oriented at angles of $45^\circ + \frac{\phi}{2}$ to the horizontal, Budhu [9], Leonards [33]. The triangular shear zone is connected to the wedge with the logarithmic spiral function suggested by Terzaghi and Peck [52],

$$a = a_0 \cdot e^{\omega \cdot \tan \phi}, \quad (3.1)$$

with a , a_0 and ω demonstrated in Fig. 3.2. By setting $\omega = \frac{\pi}{2}$ in Eq. 3.1, the length of a_1 can be obtained. The slide planes reach the ground surface in the distance of l from the corner of the foundation which is equal to,

$$l = 2 \cdot a_1 \cdot \cos\left(45 - \frac{\phi}{2}\right). \quad (3.2)$$

We need to distinguish here between dense soil and loose soil, as for the dense dilatant soil, the collapse corresponds to the peak friction angle ϕ_p , see the left diagram in Fig. 3.3. On the other hand, for loose non-dilatant soil, the failure is associated with the critical friction angle ϕ_c and no peak in the load-settlement curve is expected, see the right diagram in Fig. 3.3. In this study, the term "peak failure" is attributed to the peak of the load-settlement curve for dense soils. There is a plethora of equations available for

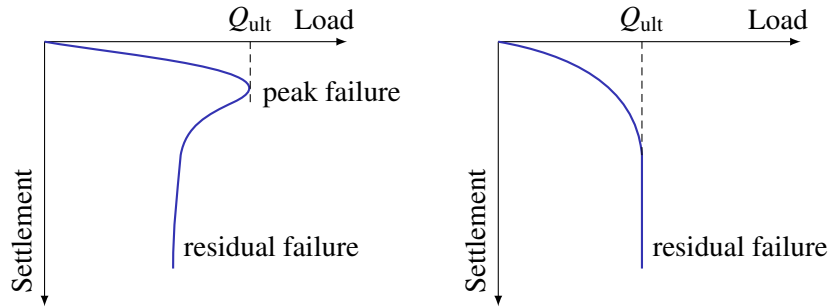


Figure 3.3: Assumed load-settlement behavior - left: dense soil, right: loose soil, by Budhu [9]

calculation of the bearing capacity of shallow foundations, regarding the friction angle φ , cohesion c and surcharge q , the expression for bearing capacity q_{ult} can be summarized as follows [29],

$$q_{\text{ult}} = \gamma \cdot B \cdot N_b + c \cdot N_c + q \cdot N_d, \quad (3.3)$$

where γ is the density of the soil and N_γ , N_c and N_q are dimensionless factors. N_γ is the factor due to the soil weight and is only a function of the friction angle. N_c and N_q take into account, respectively, the effects of cohesion and surcharge. The ultimate bearing force Q_{ult} is calculated,

$$Q_{\text{ult}} = q_{\text{ult}} \cdot B. \quad (3.4)$$

For a more detailed insight into the equations of bearing capacity, the reader can refer to [31, 9, 33].

3.2 Experimental model test

In this chapter we refer to the experimental results conducted by Aubram [2] for comparison and validation of our numerical results. These experiments were designed and conducted for the validation of the Arbitrary Lagrangian-Eulerian (ALE) method developed by Aubram, and are therefore also appropriate for our purpose. Moreover, the experiments give an insight into the phenomenology of penetration.

3.2.1 Test setup

Aubram [2] has conducted experimental tests on sand to investigate the displacement field, formation of slide planes and load-settlement behavior during punching. The experiments are carried out under quasi-static and plane strain conditions.

The model provides a chamber with internal dimensions of 1003 mm \times 502 mm \times 152 mm filled with dry sand and the model foundation has dimensions of 150 mm \times 100 mm \times 150 mm, (breadth $B = 150$ mm). The tests have been carried out at 1g and no surcharge has been applied to the ground surface.

Property	Unit	Value
angularity	-	rounded to subangular
form	-	cubic to elongate
grain mass density ρ_s	g/cm ³	2.65
e_{\min}	-	0.482
e_{\max}	-	0.779
d_{10}	mm	0.61
d_{30}	mm	1.07
d_{50}	mm	1.37
d_{60}	mm	1.58
C_u	-	2.59
C_c	-	1.19
φ_c	°	31.5

Table 3.1: Granulometric and mechanical properties of the model sand, Aubram [2]

3.2.2 Model test sand and details of penetration

The sand used for the experiments has diameter of 1 to 3 mm. The minimum and maximum void ratio of the sand lie between $e_{\min} = 0.482$ and $e_{\max} = 0.779$, respectively. In Tab. 3.1, a summary of main properties of the model sand is provided. The material model applied for our simulation is the hypoplastic model after von Wolffersdorff introduced in Sec. A.2.3 with the calibration for the model test sand summarized in Tab. A.3. The dense setup of the experiments with $e_0 = 0.545$ is chosen for back-calculation in this study. For the dense sample a maximum relative penetration depth of $(d_p/B)_{\max}$ equal to 0.55 has been achieved. The penetration increment for this experiment is $\Delta z = 2$ mm.

3.3 Numerical simulation and validation

3.3.1 Dimension of the model

The dimensions of the numerical model are chosen in correspondence to the experiment with slight modifications as demonstrated in Fig. 4.9. The simulation is conducted in plane strain condition and although it is possible to take advantage of the symmetry, the complete model is simulated. In this way, the particles lying on the symmetry line under the foundation, have more neighboring particles. This leads to better approximation of spatial variables and a more stable calculation procedure. However, for the demonstration of the results, the half symmetric parts of the simulations are plotted. For the simulation $n_p = 861$ number of particles with an average grid size of $d = 2.5$ cm were created. The fixed search radius was chosen equal to $r \approx 1 \cdot d$ so as to have the least number of required

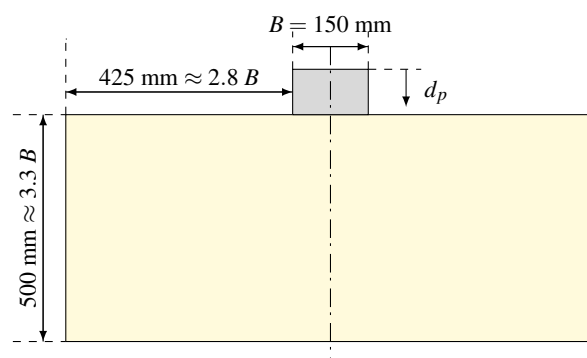


Figure 3.4: Initial geometry of the model

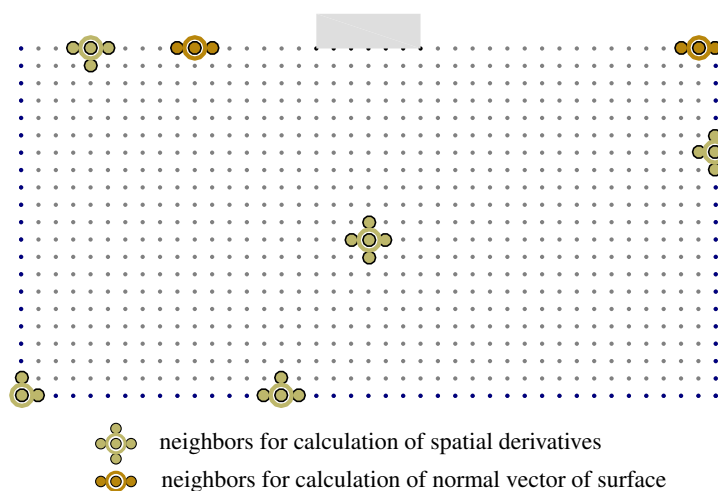


Figure 3.5: Demonstration of particle distribution and neighbors for determination of spatial derivatives and normal vector of the surface

neighbors (see Fig. 3.5). As discussed earlier in Sec. 1.9, simulations with less number of neighbors deliver the smoothest results and consequently deeper penetration depths can be achieved .

3.3.2 Foundation and boundaries

The foundation which represents a strip foundation, is rigid and perfectly rough. The particles lying on the vertical walls have freedom of movement in vertical direction and the slip boundary condition as explained in Eq. 1.3 is applied on the walls. The particles on the bottom are free to move in horizontal direction and the same boundary condition (Eq. 1.3) is applied on the bottom of the model. On the ground surface, the boundary condition with prescribed traction as explained in Eq. 1.2 is applied. For the pressure p in Eq. 1.2 a value of 1 kPa is chosen so as to avoid the occurrence of tensile stresses. Furthermore, tension control as explained in Sec. 1.7 is applied to the stress tensor of all particles after each time step. Simulations without the tension control and the slip

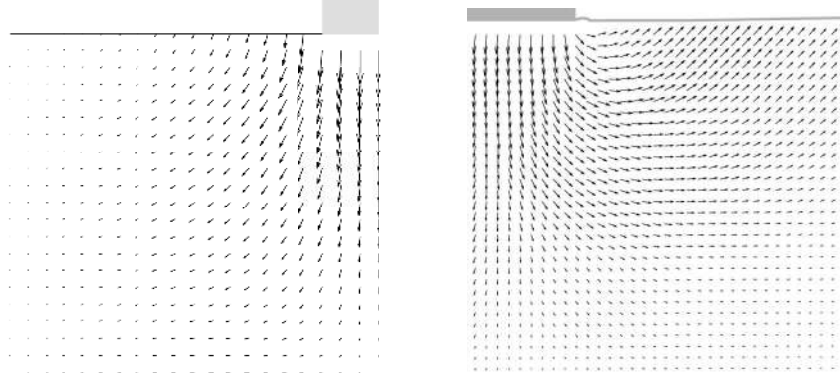


Figure 3.6: Left: SPARC simulation of shallow penetration into sand at $d_p/B = 0.01$ - smoothed incremental displacement field. Right: PIV result of shallow penetration into sand for the corresponding d_p/B - incremental displacement (adapted from Aubram [2], Fig. D.3)²

boundary condition broke before reaching the peak of the load-settlement curve.

3.3.3 Initial stress

The initial stress is assumed to be a K_0 -state, with $K_0 = 1 - \sin \varphi_c = 0.47$, according to Tab. 3.1. The stress state grows linearly with the depth,

$$T_{zz} = \gamma \cdot z, \quad (3.5)$$

and,

$$T_{yy} = T_{xx} = K_0 \cdot T_{zz}, \quad (3.6)$$

with $\gamma = 16.81 \text{ kN/m}^3$ for $e_0 = 0.545$.

3.3.4 Results and discussion

The incremental displacements after a slight penetration depth of $d_p/B = 0.01$ are compared with the experimental results in Fig. 3.6¹. SPARC is capable of simulating the outward movement of particles to the surface and boundary of the model due to the penetrating foundation. However, the incremental displacements far away from the foundation and near to the surface of the ground are underestimated in comparison to those from the experiment. As mentioned by Aubram [2], by varying the values of the granular hardness h_s (parameter of the hypoplastic model von Wolffersdorff [58]) a better prediction of the ground heaving is possible, however, this also influences the load-displacement behavior of the simulation, since the parameter h_s determines the stiffness of the material model, and has therefore been avoided in this study.

¹Differences in the size of the foundations in Figs. 3.6 to 3.11 are due to the scaling factors applied to the figures in the experimental results in Aubram [2].

²Veröffentlichungen des Grundbauinstitutes der Technischen Universität Berlin. Reproduced with permission of Shaker Verlag GmbH.

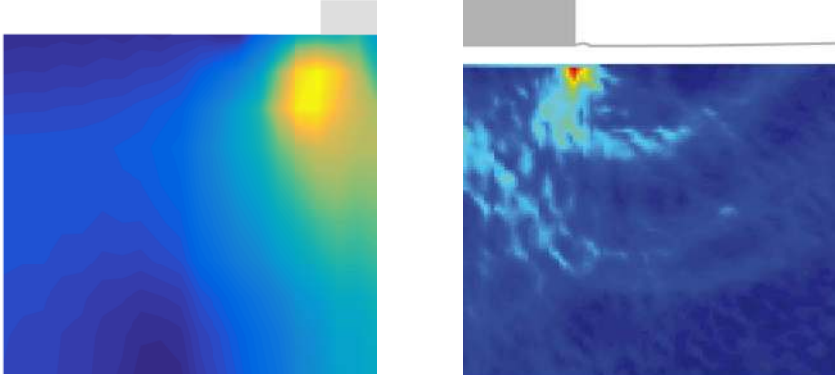


Figure 3.7: Left: SPARC simulation of shallow penetration into sand at $d_p/B = 0.01$ - smoothed maximum shear rate of deformation. Right: PIV result of shallow penetration into sand for the corresponding d_p/B - incremental maximum shear strain (adapted from Aubram [2], Fig. D.3)¹

Maximum incremental shear strains,

$$\Delta\gamma_s = \frac{1}{2}|\Delta\varepsilon_1 - \Delta\varepsilon_2|, \quad (3.7)$$

where $\Delta\varepsilon_1$ and $\Delta\varepsilon_2$ are the maximum and minimum eigenvalues of the increment in the strain tensor, respectively, are used for demonstration of shear bands in the experiments of Aubram. For demonstration of shear bands in SPARC, the maximum shear rate $\dot{\gamma}_s$ of deformation is plotted,

$$\dot{\gamma}_s = \frac{1}{2}|D_1 - D_2|, \quad (3.8)$$

where D_1 and D_2 are the maximum and minimum eigenvalues of the rate of the deformation tensor \mathbf{D} . At $d_p/B = 0.01$, the maximum incremental shear strains are compared in Fig. 3.7. PIV results show that initially, the shear strains are localized beneath the outer edge of the foundation forming a wedge under the foundation as discussed in Sec. 3.1. Results of SPARC also show the formation of the wedge beneath the foundation initiated from the outer edge of the foundation. The experimental results, also show that radial shear bands start to develop from the very beginning of the penetration (see Fig. 3.7, right). However, these initial radial shear bands are not reproduced by SPARC in this stage of penetration. In Fig. 3.8, the incremental displacements after reaching the peak of the load-displacement curve and complete formation of shear zones are plotted. Particles beneath the foundation are pushed away due to the penetrating foundation, which is very well simulated by SPARC and can be considered as an advantage of meshfree nature of SPARC, since most mesh based numerical methods are not capable of reproducing this behavior and the material points beneath the foundation follow an almost vertical trajectory, see e.g. in Fig. 3.9 the incremental displacement field predicted by ALE method compared with the experimental results. ALE results seem to be in contrast with the results obtained from the experiment(see Fig. 3.9, left), where no clear wedge formation can be observed and the incremental displacements direct under the foundation have an outward component. The incremental displacements of SPARC near to the wall boundary show that the particles move almost vertically upwards and the horizontal components of the displacement disappear, which does not correspond to the results

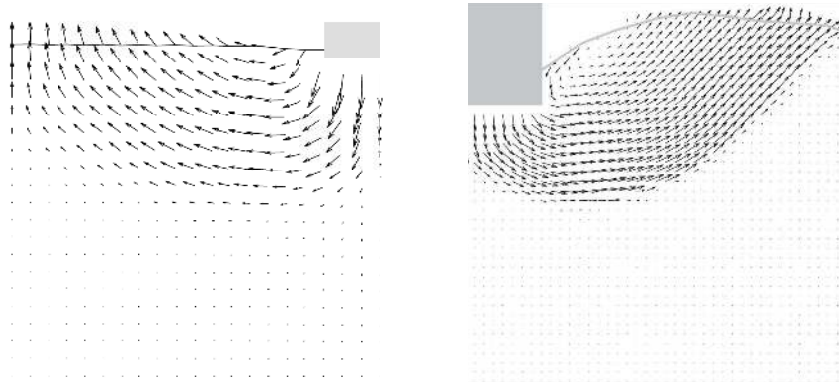


Figure 3.8: Left: SPARC simulation of shallow penetration into sand at $d_p/B \approx 0.18$ - smoothed incremental displacement field. Right: PIV result of shallow penetration into sand for $d_p/B = 0.33$ - incremental displacement (adapted from Aubram [2], Fig. D.4)¹

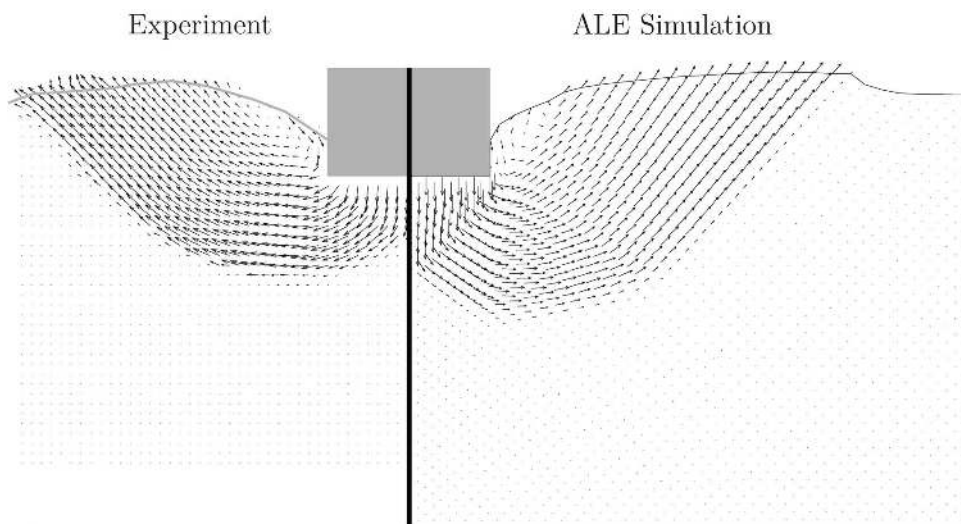


Figure 3.9: Left: PIV results of shallow penetration into sand - incremental displacements. Right: ALE simulation of shallow penetration into sand - incremental displacements (adapted from Aubram [2], Fig. 8.14)¹

from the experiment. Results from Fig. 3.11 show how well SPARC is capable of reproducing failure mechanism and the development of the slide planes. The dense sand with $e_0 = 0.545$, loosens in the shear bands and reaches a maximum value of $e \approx 0.59$. In the wedge beneath the foundation, the material is on the other hand densified and reaches $e \approx 0.53$ (see Fig. 3.10). Evaluation of incremental volumetric strain of the experiments in Aubram [2], p. 291, show that no extreme densification occurs in the wedge below the foundation, which also corresponds to the prediction of SPARC in comparison to the predictions made by the ALE method in Aubram [3] where $e = 0.482$ in the wedge has been predicted. This is due to the fact that SPARC can more realistically simulate the outward escape of the particles due to penetration under the foundation and therefore no excessive densification is predicted.

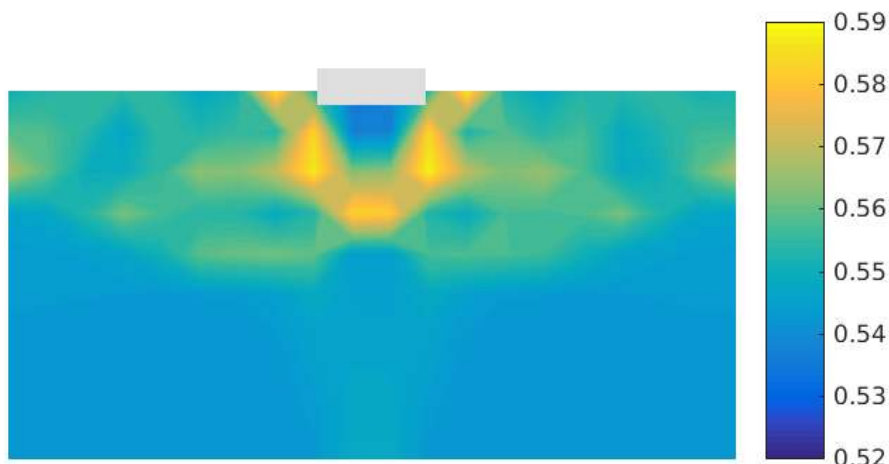


Figure 3.10: Demonstration of void ratio field for $d_p/B = 0.18$, $e_0 = 0.545$

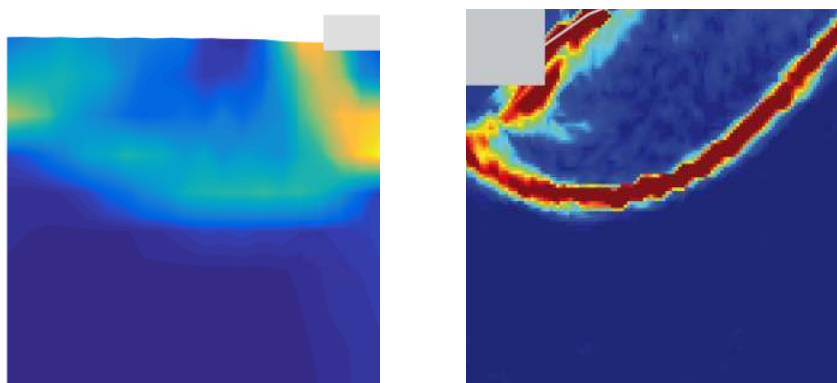


Figure 3.11: Left: SPARC simulation of shallow penetration into sand at $d_p/B \approx 0.18$ - smoothed maximum shear rate of deformation. Right: PIV result of shallow penetration into sand for the $d_p/B = 0.33$ - incremental maximum shear strain, (adapted from Aubram [2], Fig. D.4)¹

The normalized load-displacement curve obtained by SPARC is compared with the experiment in Fig. 3.12. The results show that SPARC has been able to predict the load-displacement behavior well and the peak of the curve is predicted at the same relative penetration d_p/B of the experiments. This can also be attributed to the more realistic simulation of particle trajectories in the wedge area and their outward movement which result in an earlier prediction of the full mobilization of the shear strength in comparison to other mesh based numerical methods (e.g. see Aubram [3]). Secondly, no excessive densification is predicted by SPARC in the wedge which also contributes to a better prediction of the load-displacement behavior. In Fig. 3.13, the shear bands obtained by the analytical solution as shown in Fig. 3.2 are plotted over the shear bands obtained by SPARC for comparison. It can be seen that the depth of the wedge obtained from the analytical solution is in good agreement with the one obtained from SPARC, however, the shear bands predicted by SPARC lie deeper in comparison.

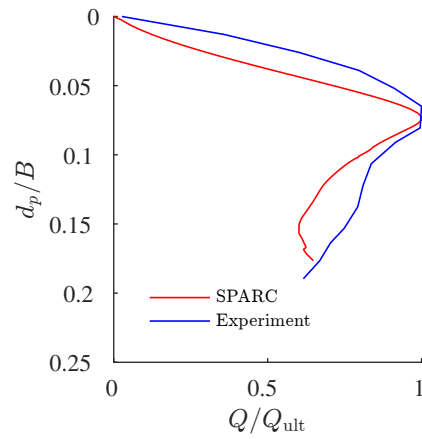


Figure 3.12: Comparison of load-displacement behavior for SPARC and the experiment, data of the experiment extracted from Aubram [2]¹

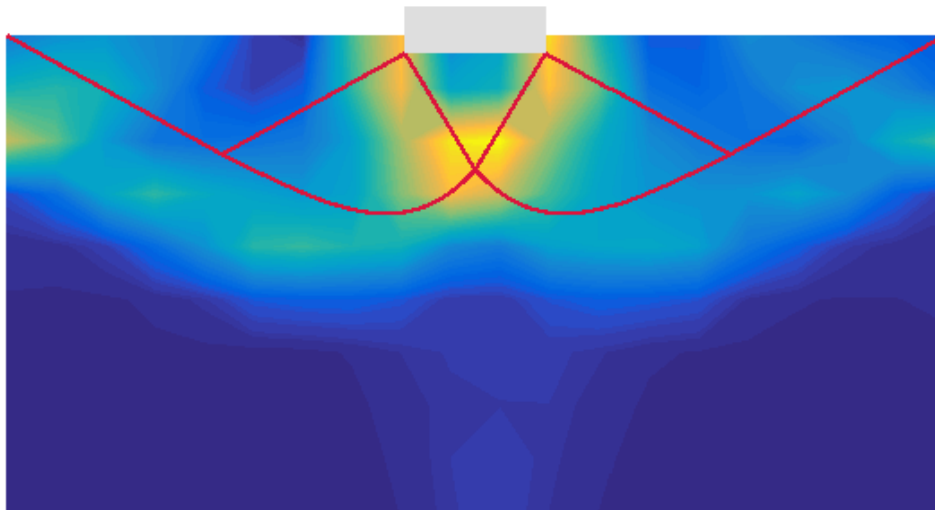


Figure 3.13: Comparison of the shape of the shear band obtained for the analytical solution (see Fig. 3.2) with the results of SPARC

4 Cone and pile penetration

4.1 General remarks

Investigation into cone/pile penetration tests can be categorized in three main fields, experimental, analytical and numerical. The analytical methods include: bearing capacity theories by limit plasticity, cavity expansion and strain path method. The numerical methods can be categorized as, conventional FEM, large-displacement FEM (ALE and adaptive remeshing), discrete element methods (DEM), and meshless methods.

4.2 Experimental analysis

4.2.1 Aubram, 2013

Aubram [2] conducted different cone penetration tests on gravelly sand 1 to 3 mm, a quartz sand with well-rounded to angular grains. The detailed granulometric and mechanical properties of the model sand are given in Tab. 3.1. The results have been evaluated by means of Particle Image Velocimetry (PIV). The pile penetration tests have been conducted in both dense and loose sand and with three different pile tips (flat, conical and hemispherical). Here, the results of his experiments for pile penetration with conical pile tip (cone) are presented. The incremental displacement and formation of shear zones for $d_p/D = 1.5$, where d_p is the penetration depth and D the maximum diameter of the cone, are plotted in Fig. 4.1.

4.2.2 Zöhrer, 2006

Zöhrer [63] carried out several CPT model tests on four Martian analogue materials ², all four materials have a grain distribution of medium silt to coarse sand. Tests are conducted in a cylindrical container with a diameter of 26.2 cm and height of 33.3 cm, the cone has a diameter of 1.8 cm, which means that the ratio of the sample diameter to cone diameter is approximately 15. Five different shapes of tips have been used for the experiments, three with conical shapes with opening angles of 30°, 45° and 60°, a spherical and a flat tip.

Zöhrer has investigated the influence of several parameters, from which, the influence of

¹Veröffentlichungen des Grundbauinstitutes der Technischen Universität Berlin. Reproduced with permission of Shaker Verlag GmbH.

²The term "Martian analogue material" is used by Zöhrer to denote a sand similar to the one expected on the surface of Mars.

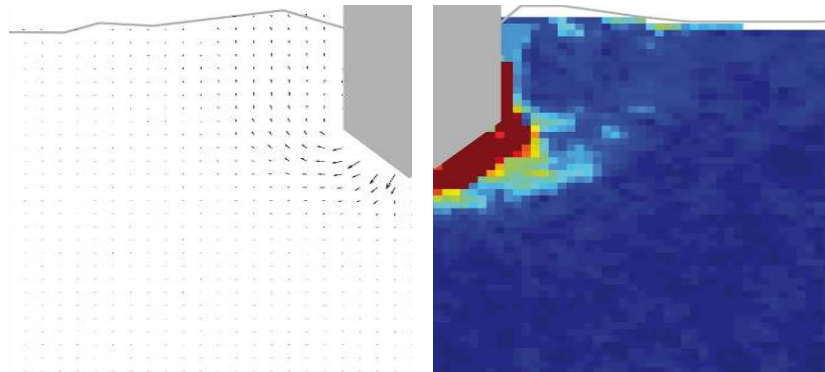


Figure 4.1: PIV results for pile penetration in dense sand ($D_r = 95\%$), Left: incremental displacements at $d_p/D = 1.5$, Right: incremental maximum shear strain at $d_p/D = 1.5$, (adapted from Aubram [2], Figs. D.10 and D.11)¹

dry density and tip shape are of interest. As expected, density has proved to have a fundamental influence on the penetration force, e.g. an almost 15% increase in density results in almost 30 times higher penetration force at a penetration depth of 20 cm. Investigations into the influence of tip shape have revealed that tip variation does not significantly affect the penetration force as the dry density does. However, it can be seen that for lower values of opening angles the penetration force is smaller and the maximum penetration force is achieved for a flat tip.

4.2.3 White, 2002

White [61] has conducted detailed experimental tests on pile penetration, a summary of his experimental results is provided here. His experiments show a cone of soil below the pile tip which moves with the pile (see Fig. 4.2). White divides the velocity field into three zones, I: directly below the pile is a zone of rigid body which is translating with the pile, II: below this zone, and extending upwards under a line at approximately 45° from the vertical is a zone of soil which is translating radially away from the pile, III: above this zone is a region of soil in which the velocity is relatively low. White finds this sharp variation in velocity in direct contrast to a cavity expansion model for penetration, in which all components are assumed to vary only in radial direction. In contrast to velocity, the trajectories illustrate the curvature of the paths during the installation (see Fig. 4.3). As the pile penetrates, the movement is generally downwards, with the soil trajectories curving toward horizontal as the pile passes. After the pile tip has passed the soil, the direction of movement reverses and the soil relaxes back towards the pile shaft. For soil elements located between $0.5D$ and $1D$ from the pile, strains reach values greater than 50% in compression and 200% in extension. These strain ranges are beyond the range of conventional laboratory tests and constitutive models are rarely applied to such large deformations. Key characteristics are sharp increase in horizontal extension close to the pile tip and the more gradual increase in vertical compression (see Fig. 4.4). On passing pile tip, soil elements remain in horizontal extension relative to their initial

³Reproduced with permission of the author: David White, University of Southampton.

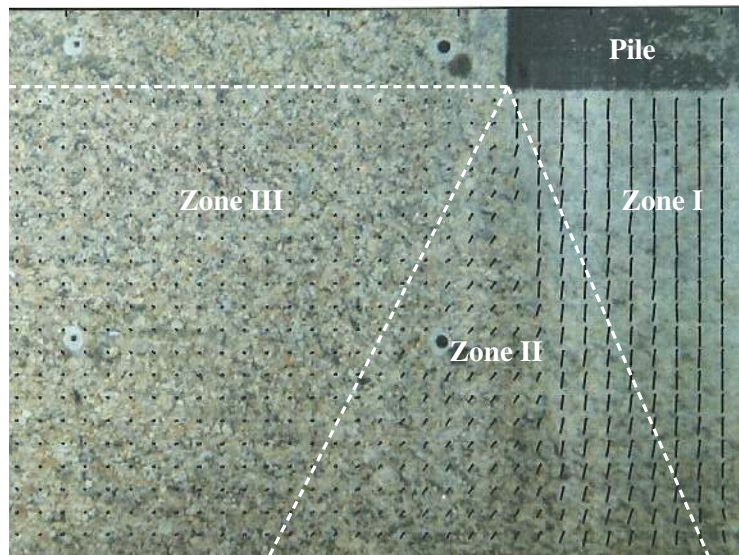


Figure 4.2: Velocity field close to advancing pile and the demonstration of cone of soil below the pile tip, the area in which the velocities have no radial component according to White (figure adapted from White [61])³

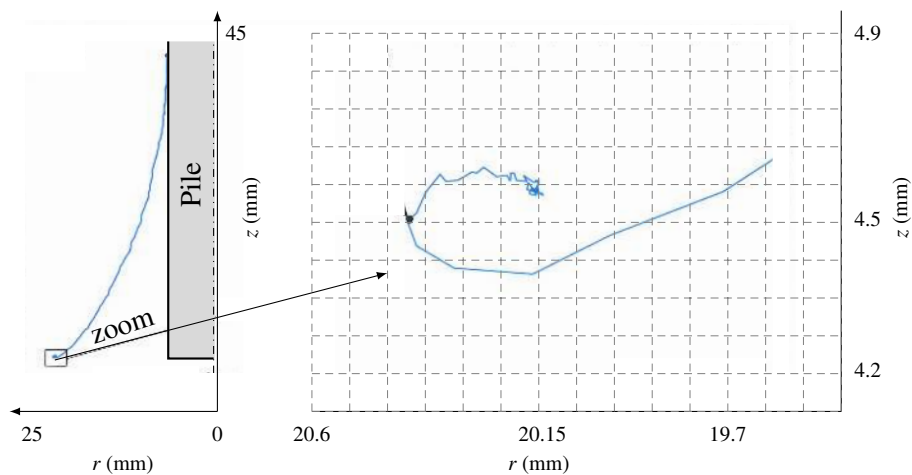


Figure 4.3: Trajectory during pile installation. Left: the black point and the box are the initial and the end points, respectively. Right: zoom-in of the box and demonstration of displacement relaxation (figure reprinted by data from White [61] p. 5-47)³

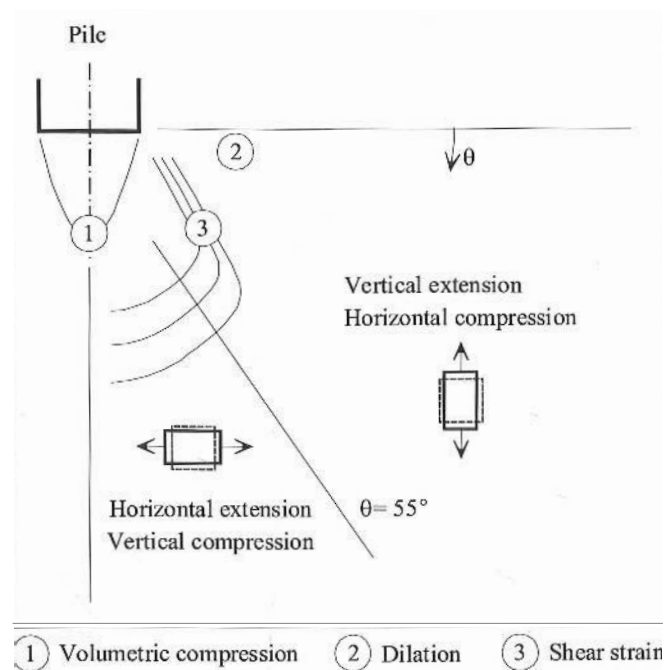


Figure 4.4: Demonstraion of strains surrounding a pile during an increment of penetration (adapted from White [61])³

state, albeit having rotated by as much as 45° . White summarizes the distribution of strain surrounding a pile during an increment of penetration in Fig. 4.4. Results of experiments conducted by White and Bolton [60] demonstrate that the effect of end wall boundary on the kinematic behavior close to the pile can be neglected.

4.2.4 Bolton et al. 1999

Bolton et al. [8] conducted a number of centrifuge cone penetration tests and investigated the effects of container size, particle size and stress level as follows,

Effect of container size

Results for B/D ratios of 85 to 8.5, where B is the distance from the periphery of the cone to the end boundary and D is the maximum diameter of the cone, for dense sand show that the difference in cone penetration resistance for B/D larger than almost 30 is negligible. However, for $B/D < 8.85$, the cone penetration resistance increases significantly (see Fig. 4.5). The suggestion by Bolton et al. [8] is to conduct cone penetration tests at least $10 \cdot D$ away from rigid boundaries.

³Geotechnique Letters by Institution of Civil Engineers (Great Britain). Reproduced with permission of Thomas Telford, Ltd. in the format Republish in a thesis/dissertation via Copyright Clearance Center.

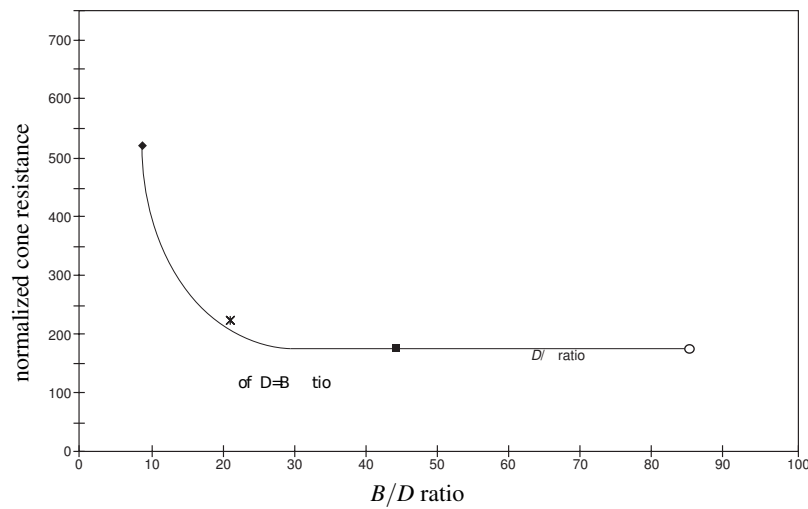


Figure 4.5: Effect of container size on cone penetration resistance, (adapted from Bolton et al. [8], p.547)⁴

Particle size effect (D/d_{50})

The effect of the ratio of cone diameter (D) to particle mean size (d_{50}) has also been studied. Results have shown that for values of D/d_{50} between 28 to 85, cone penetration resistance is not affected significantly by particle size. However, it has been reported that some increase in cone penetration resistance is to be expected if the value of D/d_{50} falls below 20.

Stress level effect

Three different tests for elevated gravity levels of 40g, 70g and 125g have been conducted, while other parameters have been kept constant. The results demonstrate that the penetration resistance decreases with increase of stress. Bolton et al. argue that this decrease could be due to grain crushing.

4.3 Analytical methods

The analytical methods suffer from shortcomings due to the assumptions made. The bearing capacity methods, define the soil behavior as rigid-plastic and the failure mechanisms do not comply with the boundary conditions. The cavity expansion method is not capable of modeling the real shape of the cone (Teh [49], Baligh [5]). The experimental results conducted by White [60] are in direct contrast with strains calculated by cavity expansion theory, in which they increase as the pile approaches. Finally for the strain path method, although the obtained strain paths match well with the experimental results, the volumetric behavior of the sand is not captured since the method is developed for undrained penetration. Furthermore, the stress field determined by the strain path method does not satisfy the equilibrium conditions, Teh [49].

Due to the shortcomings of the above mentioned methods and the uncertainties included

	rough		smooth	
	u_z	u_r	u_z	u_r
shaft	prescribed	0	free	0
cone	prescribed	0	prescribed	0

Table 4.1: Description of kinematic boundary conditions for rough and smooth cone, u_z and u_r are the vertical and radial displacements, respectively

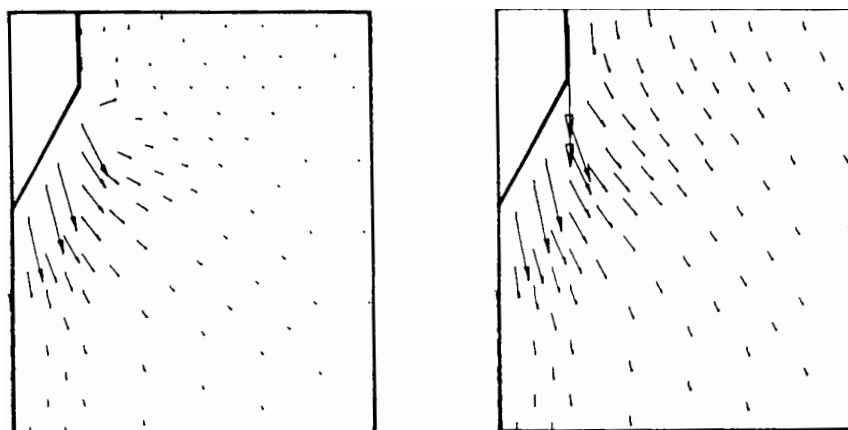


Figure 4.6: Comparison of displacement field for smooth cone, (left) and rough cone, (right) (adapted from Teh [49] p. 8.12)⁵

in the derivation of the theories, we avoid to further explain these methods. Interested readers are referred to Durgunoglu and Mitchell [13] for bearing capacity theory, Yu and Hously [62] for cavity expansion theory and Baligh [6] for strain path method.

4.4 Numerical models

4.4.1 Conventional finite element method

Teh [49] carried out analytical and numerical investigation of the cone penetration test into clay, for the analytical investigation he applied the strain path method, in which the soil is assumed to flow like a viscous fluid. In the numerical FEM model, the cone has been simulated wished in place. Teh investigates rough and smooth boundaries. He defines the boundary conditions on the shaft of the cone different from the cone for rough and smooth conditions, see Tab. 4.1 for boundary conditions applied by Teh. Teh mentions that the displacement fields below the tip in both cases are found to be similar and the rough shaft affects only soil displacements adjacent to it, in contrast to the smooth shaft, where the displacements around the shaft are very small (see Fig. 4.6).

Cudmani [12] conducted simulations for cone penetration test (CPT) in axisymmetric conditions. Cudmani has used the hypoplastic model after von Wolffersdorff [58] with

⁵Reproduced with permission of the author: Teh Cee, Nanyang Technological University, Singapore

the calibration from Herle and Gudehus [22] for his simulations. The simulations have been carried out with and without intergranular strain concept (Niemunis and Herle [39]). The cone has been modeled as a rigid body and friction-free contact between the soil and the shaft has been assumed. The following boundary conditions have been assumed:

- on the wall: $T_{rr} = \text{const.}$ and $T_{r\vartheta} = 0$
- on the ground surface: $T_{zz} = \text{const.}$
- on the bottom: $u_r = u_z = 0$
- penetration: $v_z = \text{const.}, u_r = 0$

The results of Cudmani show that the radius, at which the void ratio (e) experiences a change of 1% of its initial value, is half of the radius at which pressure components (p_r and p_z) reach 1% change in their initial value. Results of calculations with the hypoplastic model without intergranular strain concept underestimate the experimental values for penetration force obtained in experiments with Ticino [4], Toyoura [15], Monterey [46] and L. Buzzard [23] sands. Cudmani explains that the underestimation of penetration force when no intergranular strain concept is implemented could be attributed to changes in the direction of deformation, which lead to stiffer response of soil and cannot be modeled without intergranular strain concept.

4.4.2 Large displacement finite element method

Aubram [2] has analyzed the penetration into sand by means of an Arbitrary Lagrangian-Eulerian method (ALE) particularly developed for plane and axisymmetric penetration into sand. The developed ALE method breaks up solution of the governing equations over a time step into a Lagrangian step, and a mesh regularization step. Simulations have been carried out with the hypoplastic model proposed by Gudehus [19] and Bauer [7] with the intergranular strain concept proposed by Niemunis and Herle [39]. Aubram reported the large variation of the soil stiffness at the free surface and underneath the cone as a challenge which may lead to an ill-conditioned stiffness matrix and therefore, stable and robust simulations are usually hard to achieve. In his simulations, the pile is assumed to be rigid and its surface is assumed to be perfectly smooth. The dimensions of the computational domain in the three models are $250 \text{ mm} \times 700 \text{ mm} = 5D \times 14D$, ($D = 50 \text{ mm}$) which comply with the configuration of the experimental tests in Sec. 4.2. It needs to be mentioned that Aubram has considered an artificial capillary pressure of 0.1 kPa in order to improve the stability at very low mean effective stress levels. Comparison of numerical with experimental results are shown in Fig. 4.7.

Zöhrer [63] carried out discrete element method (see Sec. 4.4.3) and FEM simulations with ALE adaptive remeshing for further investigation of the CPT procedure. For FEM calculations with ALE adaptive mesh, the non-associated Drucker-Prager failure criterion and the hypoplastic constitutive model were used⁶.

Zöhrer mentions that the increase of voids between particles as a result of penetration in circumferential direction can be modeled properly by DEM and continuum mechanical methods can deal with loosening in circumferential direction only under high compressive stress so that the loosening leads only to reduction of the compressive stress. How-

⁵Veröffentlichungen des Grundbauinstitutes der Technischen Universität Berlin. Reproduced with permission of Shaker Verlag GmbH.

⁶Zöhrer does not mention exactly which version of hypoplasticity has been implemented for FEM simulations.

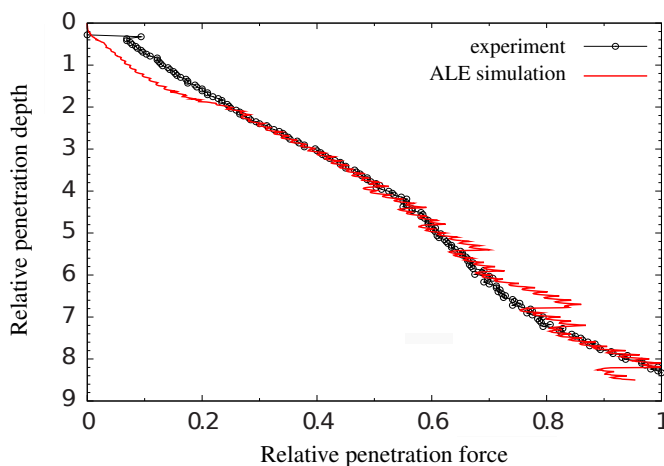


Figure 4.7: Comparison of the measured and predicted load-displacement curves of pile penetration for pile with conical tip, $D_r = 21\%$ (adapted from Aubram [2], Fig. 8.23)¹

ever, results of FEM regardless of the uppermost centimeters of the penetration, have shown better accuracy and a plausible dependency of the penetration resistance on the input parameters compared to DEM.

Van Den Berg [56] has applied an extension of the updated Lagrangian description to an Eulerian formulation (ALE). As for the constitutive model, Drucker-Prager criterion has been applied. van den Berg et al. models the cone as a fixed boundary with interface friction and the boundaries are defined by spring elements. The initial K_0 condition is applied for stress state and the simulation is conducted wished in place. The process of penetration is applied by incremental displacements at the lower boundary of the mesh. Susila and Hryciw [48] have used an auto-adaptive FEM method for simulation of cone penetration test. Sand behavior is simulated by Drucker-Prager constitutive model and Coulomb friction law has been implemented for the interface. The type of mesh adaptivity used, is the r -adaptivity scheme, in which the distorted mesh is changed by relocating nodes without adding or deleting degrees of freedom. Susila and Hryciw do not use the wished in place method as opposed to the study conducted by Van Den Berg, therefore, the horizontal stresses on the cone are not underestimated. Furthermore, in their simulations, the vertical displacements on the top of the soil are constrained.

4.4.3 Discrete element method

Zöhrer [63] conducted discrete element simulations for further investigation of the cone penetration. His results show that the field of displacement is not smooth at all (see Fig. 4.8). Furthermore, particles at a radius of $0.5D$ from the shaft have a radial and downward movement and the particles out of this range have an upward movement, particles at the bottom of the model also show irregular directions. Throughout the process, smaller particles are pushed into pores between larger particles.

Wang and Zhao [59] conducted 2D discrete element method simulations in crushable



Figure 4.8: Displacement vectors of particles obtained by discrete element method (adapted from Zöhrer [63])

sands. The crushable sand was modeled only around the pile. The validation of their model has been done by comparing the results with published centrifuge and calibration chamber tests. The boundaries of the model are set to $30 \cdot D$ while the crushable zone is limited to $2 \cdot D$ width and $27 \cdot D$ depth, in the middle of the model. The strains obtained by Wang and Zhao are compared with the experimental results of White [60], see Sec. 4.2, and are found to be in good agreement.

Finally, Wang and Zhao report that the two factors, controlling the the tip resistance in their model are, in situ stress and particle breakage.

4.5 Simulation of cone penetration with SPARC

The simulation of the cone penetration into sand was a challenging task for SPARC and no noticeable penetration depths could be obtained in the scope of this study. Many attempts were made at achieving this goal, which can be classified in two groups: (i) ideas which can be considered as modification of framework of SPARC (discussed in Sec. B) and (ii) efforts at defining the boundary condition of the penetrating cone.

In the first series of attempts, the penetrating cone was simulated with adherent particles, this assumption does not correspond to the reality, though. Adherent particle means that it is fixed in the horizontal direction and in the vertical direction the velocity is prescribed equal to the velocity of the penetration. The boundary condition of adherent particles causes unreasonable stress states and void ratios for particles lying on the cone and the simulation aborts before a notable penetration depth is achieved.

In the second series of attempts, the penetrating cone is assumed to be perfectly smooth. Therefore, two different smooth boundary conditions were implemented in SPARC for the smooth cone which are explained in the following sections. The penetration depth in case of the perfectly smooth cone was even less than the boundary condition with adherent particles.

Last but not least, I must mention here that throughout this study many other attempts

were made towards simulation of cone penetration, which are presented shortly here,

- Different initial geometries, e.g. modeling half of the model by benefiting from the symmetry
- Different initial distribution of particles, e.g. irregular distribution or modeling a column of particles on the symmetry line or not
- Considering different initial void ratios or different initial stress states by applying different values for p in Eq. 1.2
- Repeating the simulation for all the constitutive models explained in Chp. A and linear elastic material model
- Defining different search radii for the neighboring particles.
- Searching for new neighbors after each time step or maintaining the initially searched neighbors from the first time step.

All these unsuccessful attempts could be considered valuable for future studies with SPARC. Since they mean that for simulation of cone penetration with SPARC either the framework of the code needs to undergo modifications or the cone needs to be modeled differently.

All in all, our investigations show that simulating a *moving* kinematic boundary condition by means of soft particles which are actually *soil* particles can work well only for problems where the boundary does not penetrate into the continuum like the upper plate in oedometer, biaxial or triaxial tests or when the penetration is relatively small like simulation of punching (see Chp. 3) or cone penetration for small penetration depths.

4.5.1 Geometry of the problem and plane strain condition

For the simulation of CPT, the experiments conducted by Aubram [2] are used. A half-cylindrical pile with a conical segment with a diameter of $D = 50$ mm is used to model cone penetration. However the simulations in SPARC are conducted in 2D with plane strain condition. The penetrating cone has a length of 650 mm and the maximum penetrating depth is 400 mm which is equal to $d_p/D \approx 8$, where d_p is the depth of penetration. For detailed dimensions and geometry of the penetrating pile with cone tip, see Fig. 4.9. The minimum boundary distance to the periphery of the penetrating cone is $S/D = 5$, the chamber of the experiment has a depth of 891 mm and the depth of the sand in the chamber is about 700 mm.

Plane strain condition

As it is discussed in Sec. B.1, the attempt at simulating the cone penetration in axisymmetric SPARC failed. The simulations presented in this section are conducted in plane strain condition and correctly speaking, the penetration of a *prism* into soil is simulated and not the penetration of a cone.

4.5.2 Wall and bottom boundaries

The particles lying on the vertical walls of the model have freedom of movement in vertical direction and the slip boundary condition as explained in Eq. 1.3 is applied on the walls. The particles on the bottom are free to move in horizontal direction with the same boundary condition explained in Eq. 1.3.

On the ground surface, the static boundary condition as explained in Eq. 1.2 is applied.

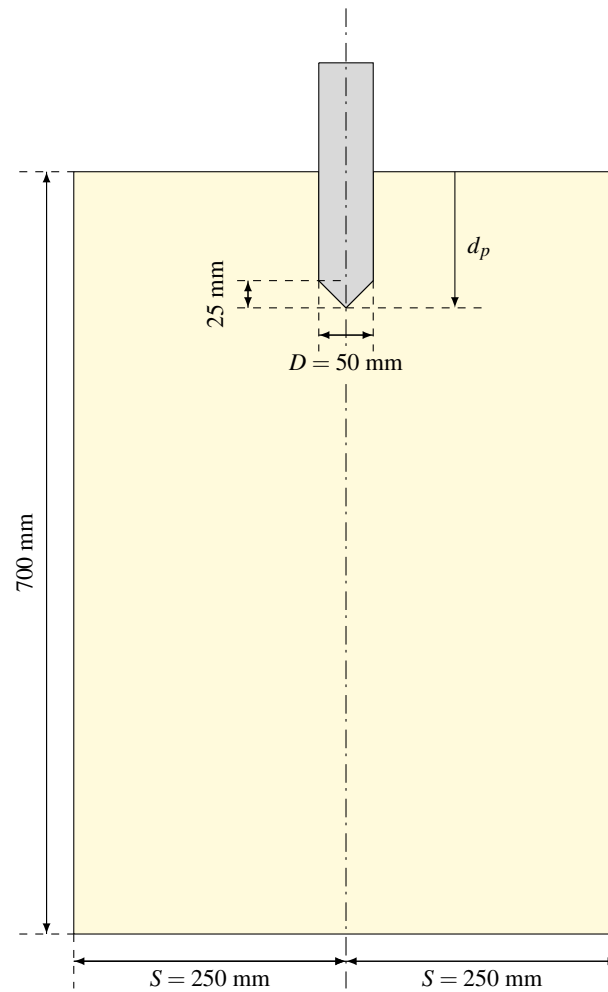


Figure 4.9: Geometry of the model

For the pressure p in Eq. 1.2 a value of 60 kPa is chosen so as to avoid tensile stresses. Furthermore, tension control as explained in Sec. 1.7 is applied to the stress tensor after each time step.

4.5.3 Initial stress

The initial stress is assumed to be a K_0 -state, with $K_0 = 0.47$ (see Sec. 3.3.3). The stress grows linearly with depth,

$$T_{zz} = \gamma \cdot z, \quad (4.1)$$

and,

$$T_{yy} = T_{xx} = K_0 \cdot T_{zz}, \quad (4.2)$$

with $\gamma = 15.71 \text{ kN/m}^3$ for $e_0 = 0.71$. In this chapter only the simulation results conducted with the material model after Kolymbas (2011) introduced in Sec. A.2.1 are presented.

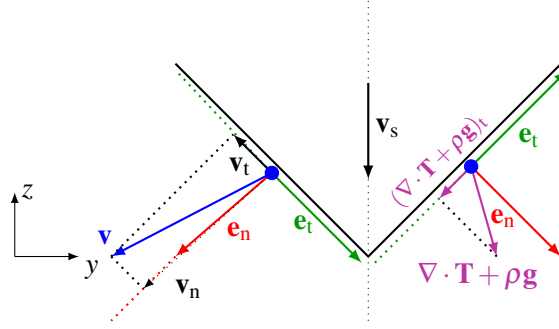


Figure 4.10: Vectors for explanation of Boundary condition I

4.5.4 Smooth cone - boundary condition I

For the simulation of a penetrating cone with smooth surface, the following boundary condition for the cone is implemented in SPARC. It is not claimed that solving the equilibrium equation on the boundary of the cone is strictly correct. The cone has a constant vertical velocity $\mathbf{v}_s = [0, v_s]^T$. The unit normal and tangential vectors (\mathbf{e}_n and \mathbf{e}_t) on the cone are determined. For particles lying on the cone, we consider the normal component \mathbf{v}_n and the tangential component \mathbf{v}_t (see Fig. 4.10). \mathbf{v}_n is determined as follows,

$$\mathbf{v}_n = (\mathbf{v}_s \cdot \mathbf{e}_n) \cdot \mathbf{e}_n. \quad (4.3)$$

For \mathbf{v}_t , the equilibrium equation $\nabla \cdot \mathbf{T} + \rho \mathbf{g} = 0$ is calculated and projected in the tangential direction as follows,

$$(\nabla \cdot \mathbf{T} + \rho \mathbf{g})_t = ((\nabla \cdot \mathbf{T} + \rho \mathbf{g}) \cdot \mathbf{e}_t) \cdot \mathbf{e}_t. \quad (4.4)$$

By means of Newton solver, a tangential velocity will be determined that fulfills the following requirement,

$$|(\nabla \cdot \mathbf{T} + \rho \mathbf{g})_t| \leq \varepsilon,$$

where ε is the accepted tolerance. After \mathbf{v}_t is determined, the total velocity of the particle is known as the sum of the normal and the tangential velocities,

$$\mathbf{v} = \mathbf{v}_t + \mathbf{v}_n.$$

Finally the components of the acquired velocity in y - and z -directions are determined,

$$v_y = \mathbf{v} \cdot \mathbf{e}_y, \quad v_z = \mathbf{v} \cdot \mathbf{e}_z.$$

Results of smooth cone - boundary condition I

The solution obtained (velocity field) by the solver for four different relative penetration depths are plotted in Fig. 4.11, the red arrows show the velocities obtained for the cone by solving the boundary condition explained in Sec. 4.5.4. Unfortunately, the simulation breaks after reaching a maximum relative penetration depth $d_p/D = 0.047$. In Fig. 4.12 the velocities around the cone and the velocities at the cone for the smooth boundary condition I are plotted. In the first glance, one can deduce that by increasing penetration,

the velocity field looks less smooth and the obtained velocities make less sense. For example in Fig. 4.12 for $d_p/D = 0.04$ and 0.047 . The two columns of particles lying on the left and right side of the symmetry line move inwards instead of moving outwards, which contradicts the expectation that particles should be pushed away by the penetrating cone. The velocities obtained at the cone have from the beginning of the simulation an inward inclination, which means that these particles are not pushed away as the cone approaches them.

4.5.5 Smooth cone - Boundary condition II

In this section, the boundary condition for smooth surface, as explained in Eq. 1.3 is applied for simulation of a smooth cone. Eq. 4.5 demands that the shear stresses on the shaft and tip of the cone disappear,

$$\mathbf{e}_n^T \cdot \mathbf{T} \cdot \mathbf{e}_t = 0. \quad (4.5)$$

For the particles lying on the cone, we consider the normal component \mathbf{v}_n and the tangential component \mathbf{v}_t (see Fig. 4.13). \mathbf{v}_n is determined with Eq. 4.3. For determination of \mathbf{v}_t , first the stress vector \mathbf{t} is calculated,

$$\mathbf{t} = \mathbf{T} \cdot \mathbf{e}_n, \quad (4.6)$$

and projected in the tangential direction as follows,

$$(\mathbf{t})_t = \mathbf{t} \cdot \mathbf{e}_t. \quad (4.7)$$

By means of Newton solver, a tangential velocity will be determined that fulfills the following requirement,

$$|(\mathbf{t})_t| \leq \varepsilon,$$

where ε is the accepted tolerance. After \mathbf{v}_t is determined, the total velocity of the particle is the sum of the normal and the tangential velocities,

$$\mathbf{v} = \mathbf{v}_t + \mathbf{v}_n.$$

Finally the components of the acquired velocity in y - and z -directions are determined,

$$v_y = \mathbf{v} \cdot \mathbf{e}_y, \quad v_z = \mathbf{v} \cdot \mathbf{e}_z.$$

Results of smooth cone - boundary condition II

In Fig. 4.14 a comparison of obtained velocities at the cone for both smooth boundary conditions is shown. Although there are still oscillations present in the obtained velocities, the velocities at the cone for boundary condition II have mainly outward components, which is in agreement with the expectation that particles at the vicinity of the cone should be pushed away.

The obtained velocity field for the above smooth boundary condition is plotted in Fig. 4.15. The maximum relative penetration depth is almost the same as for the boundary condition introduced in Sec. 4.5.4. However, the boundary condition II offers two advantages. Firstly, the velocity field is smoother and the velocities of particles make better sense, compare Figs. 4.12 and 4.16.

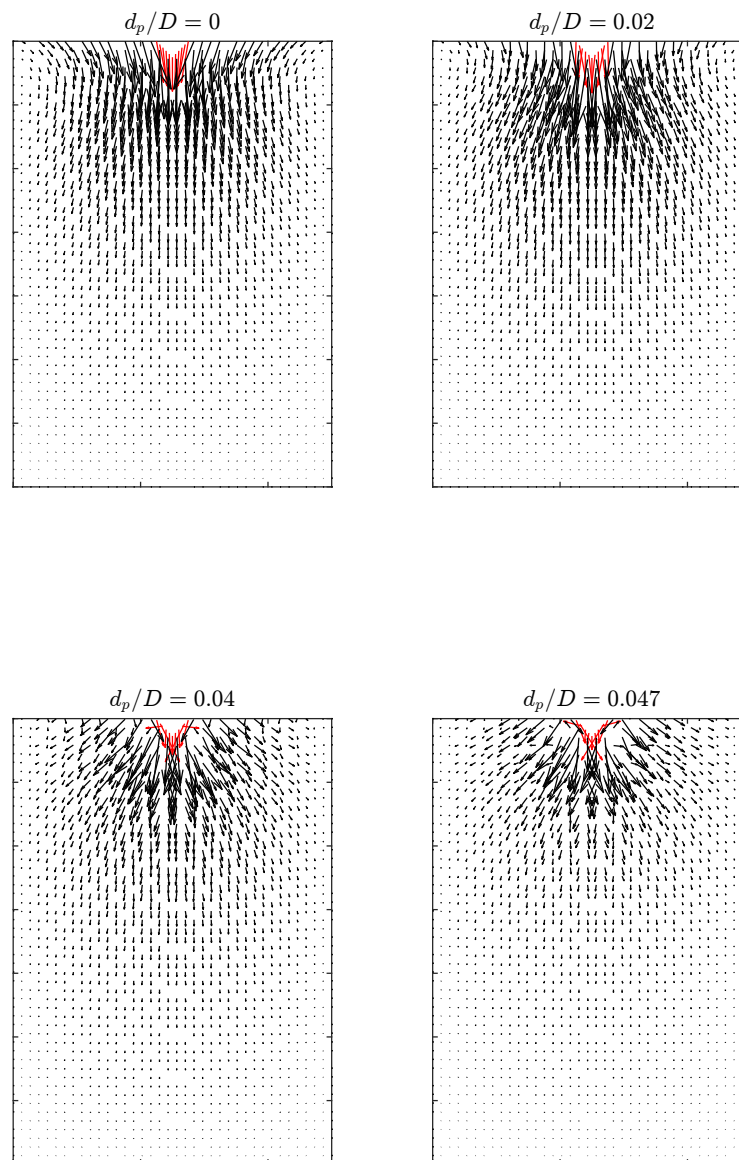


Figure 4.11: Obtained solution (velocity field) for increasing relative penetration depths, d_p/D , the red arrows represent the obtained velocities at the cone, smooth cone-boundary condition I, see Fig. 4.12 for zoom of velocities around the smooth cone

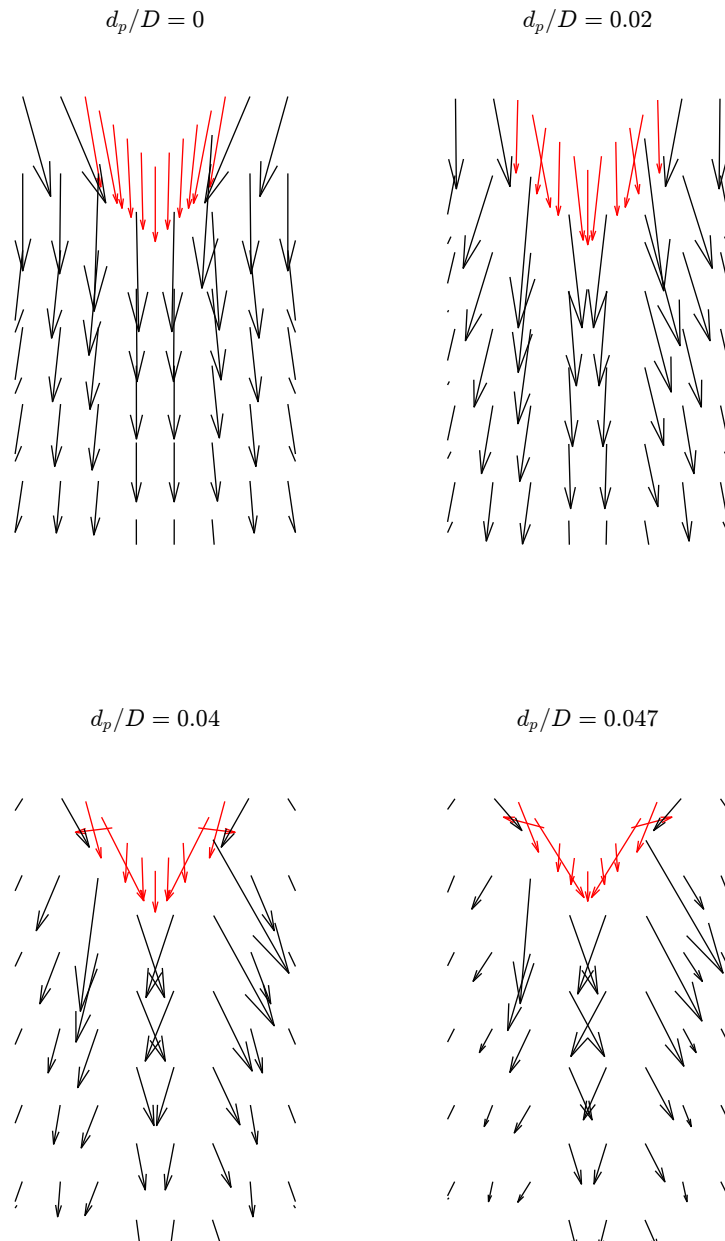


Figure 4.12: Zoom of obtained solution (velocity field) around the cone for increasing relative penetration depths, d_p/D , the red arrows represent the obtained velocities at the cone, , smooth cone-boundary condition I

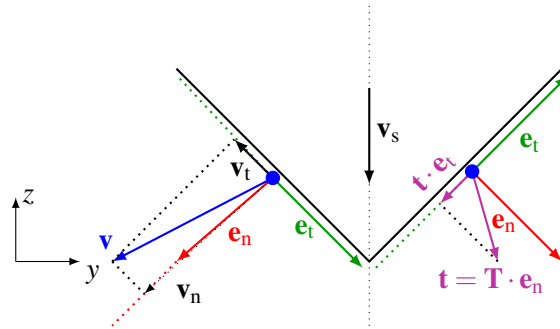


Figure 4.13: Vectors for explanation of Boundary condition II

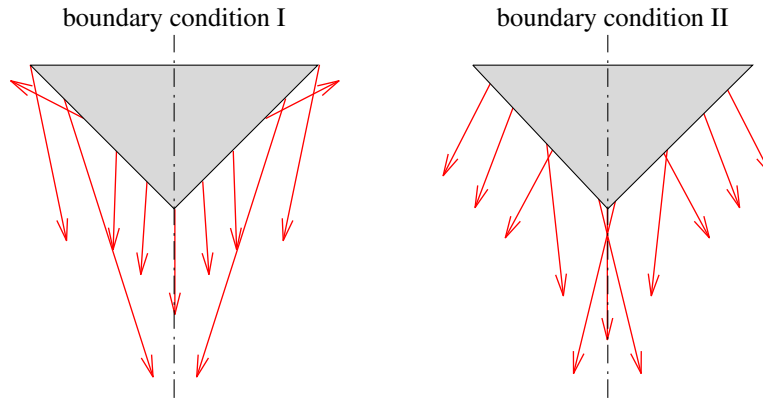


Figure 4.14: Comparison of obtained velocities for smooth boundary conditions, Left: boundary condition introduced in Sec. 4.5.4, right: boundary condition introduced in Sec. 4.5.5

4.5.6 Adherent particles

The maximum relative depth $d_p/D = 0.35$ is obtained for adherent particles. Adherent particle means that for the cone particles the velocity in the vertical direction is prescribed and the horizontal velocities are set to zero. It must be mentioned that SPARC was able to reach the relative depth of $d_p/D = 0.35$ through the implementation of "re-conditioning of the solution" (explained in Sec. 1.8). Without benefiting from this feature in SPARC, relative depths of only 0.1 were possible to obtain. In Fig. 4.17 the obtained velocities for different relative depths are plotted. The velocity field is almost smooth in the initial stages of the penetration, however, one can detect oscillations in Fig. 4.17 for $d_p/D = 0.35$, especially on the soil surface and near to the cone. In Fig. 4.18 the zoom of the results in the vicinity of the cone for the corresponding relative depths is plotted. In Fig. 4.19, the development of void ratio and the norm of stress throughout the simulation for one particle on the surface of the cone are plotted. Fig. 4.19 shows how the norm of stress for an adherent particle grows enormously throughout the simulation and its void ratio becomes negative (see also Sec. B.6). It is important to mention that this particle is not the particle on the tip of the cone, where it is expected to observe strong

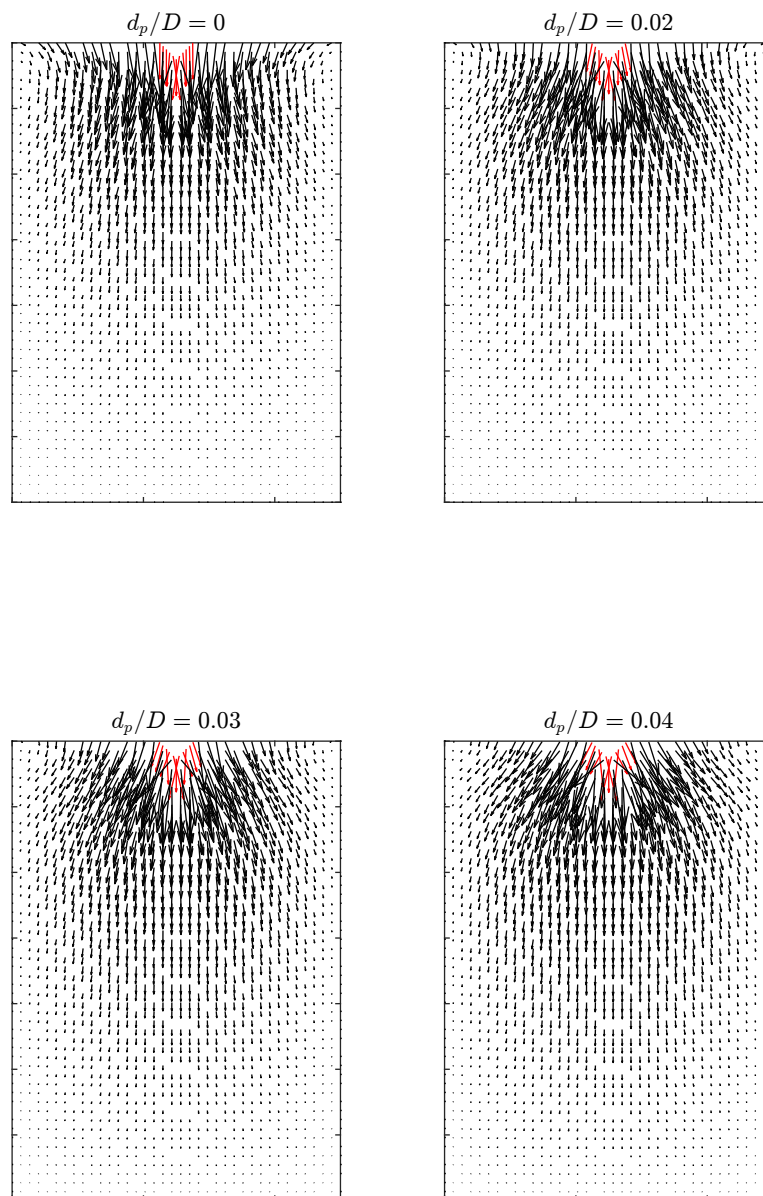


Figure 4.15: Obtained solution (velocity field) for increasing relative penetration depths, d_p/D , the red arrows represent the obtained velocities at the cone, smooth cone-boundary condition II, see Fig. 4.16 for zoom of velocities around the smooth cone

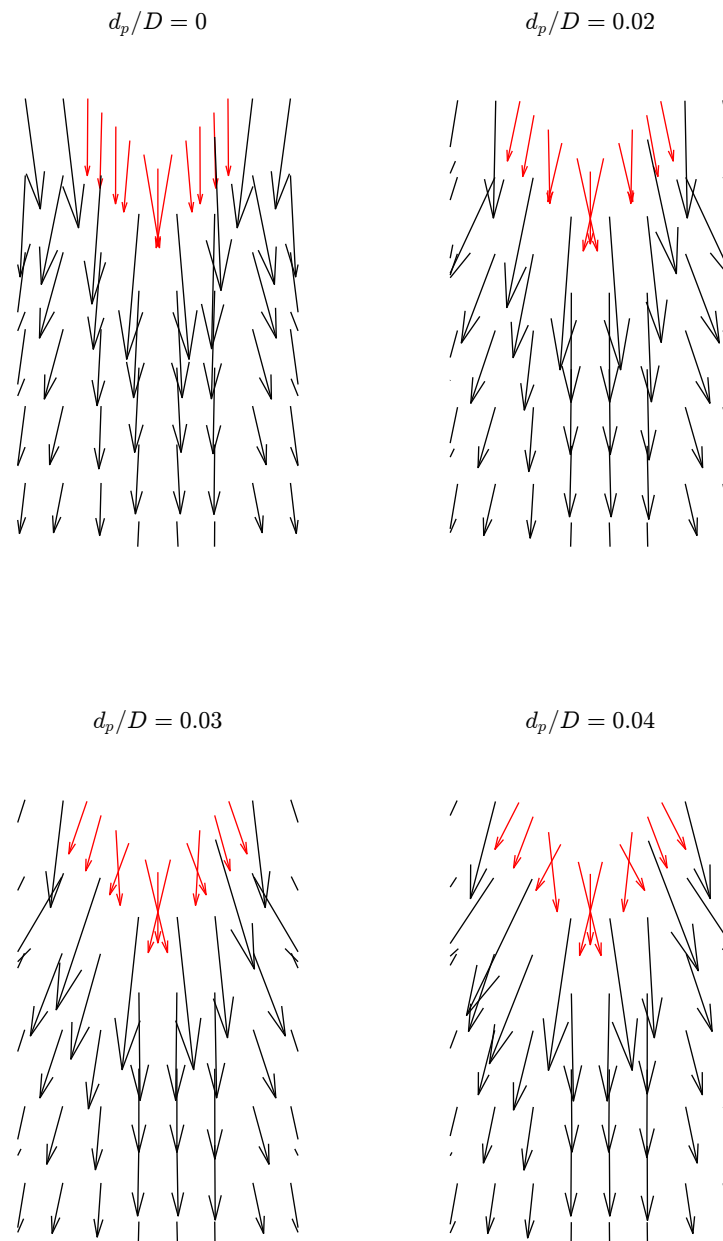


Figure 4.16: Zoom of obtained solution (velocity field) around the cone for increasing relative penetration depths, d_p/D , the red arrows represent the obtained velocities for the cone, smooth cone-boundary condition II

densification and even grain breakage, but lies on the shaft of the cone. A precise look at the velocity field adjacent to the cone in Figs. 4.17 and 4.18 shows how the adherent boundary condition pulls the surface and neighboring particles throughout the simulation towards the cone. On the other hand, the adherent particles are fixed in horizontal direction and cannot move away. Therefore, it is reasonable for the adherent particles to experience excessive densification and large changes in stress. These results show that the boundary condition of adherent particles is not correct and leads to unreasonable values of void ratio, density and stress.

In Fig. 4.19, a jump in both diagrams at the same calculation progress of $t \approx 500$ can be observed. The jump occurs when the void ratio of the particle becomes negative and afterwards, the $|\mathbf{T}|$ grows with a steeper slope. A closer look at the material model Kolymbas 2011 explained in Sec.A.2.1 and its f function (Eq. A.8), shows that the f function delivers large values for negative void ratio and consequently, the response of the material model becomes stiffer.

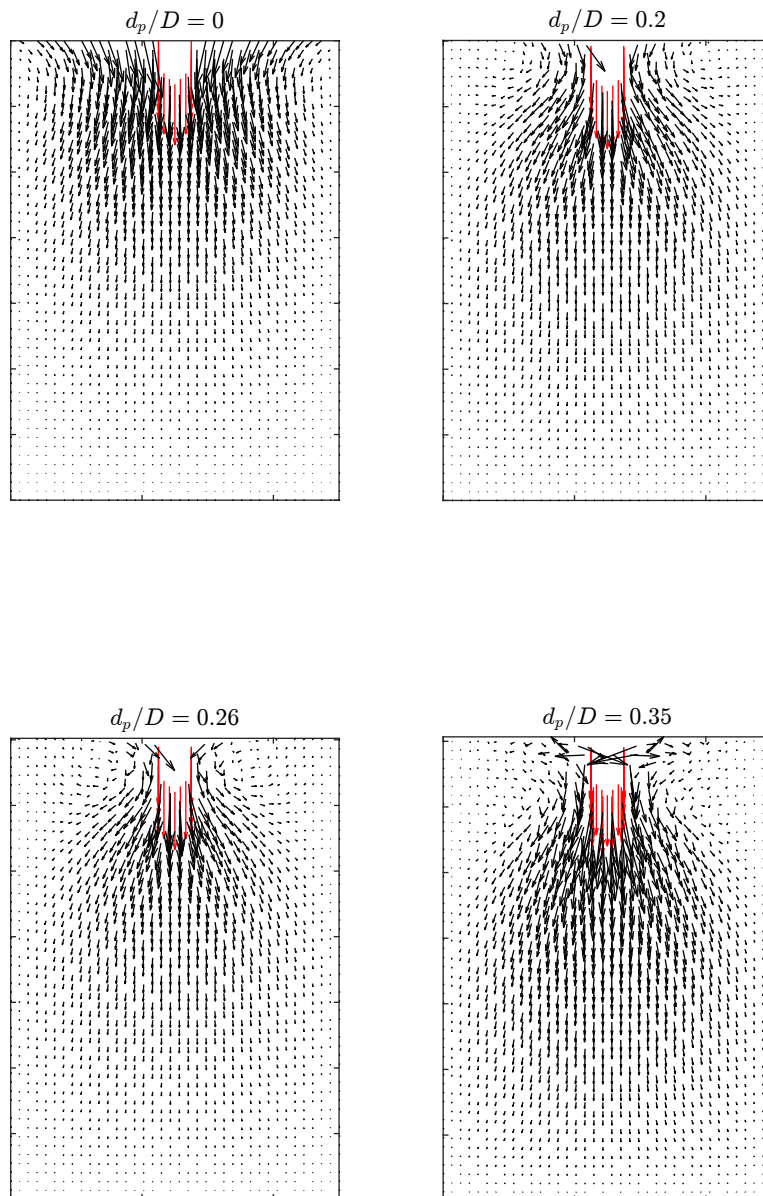


Figure 4.17: Obtained solution (velocity field) with adherence at the cone surface for increasing relative penetration depths, d_p/D , the red arrows represent the prescribed velocities at the cone for adherent particles, see Fig. 4.18 for zoom of velocities around the cone

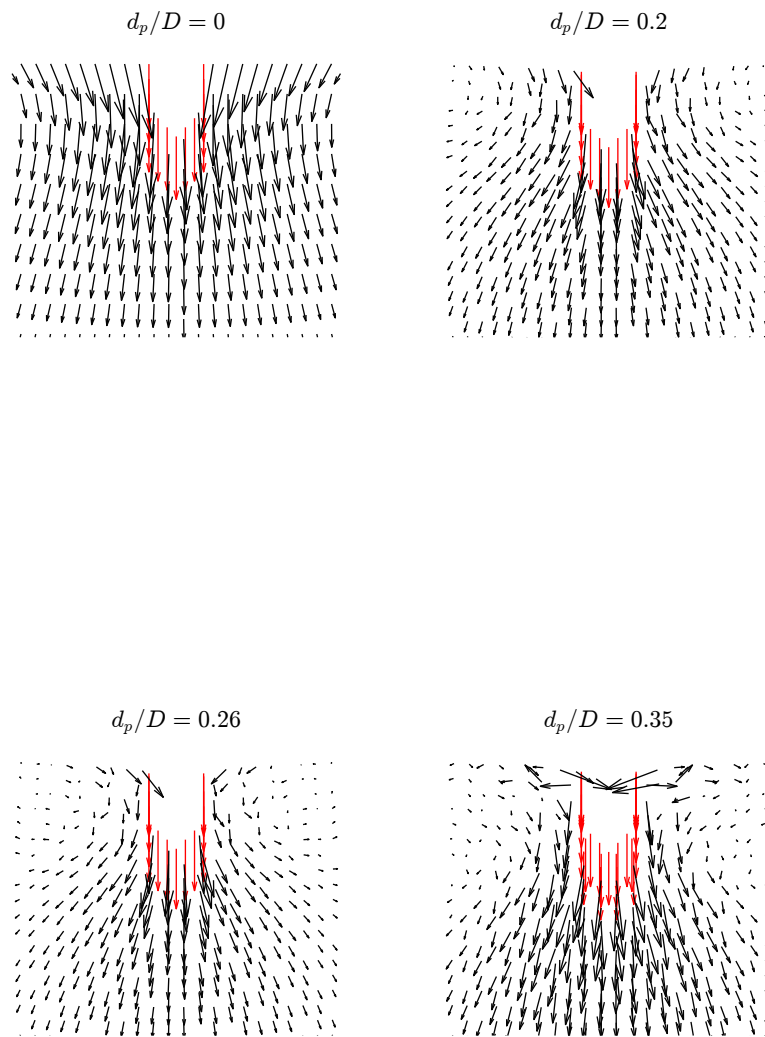


Figure 4.18: Zoom of obtained solution (velocity field) with adherence around the cone for increasing relative penetration depths, d_p/D , the red arrows represent the prescribed velocities at the cone for adherent particles

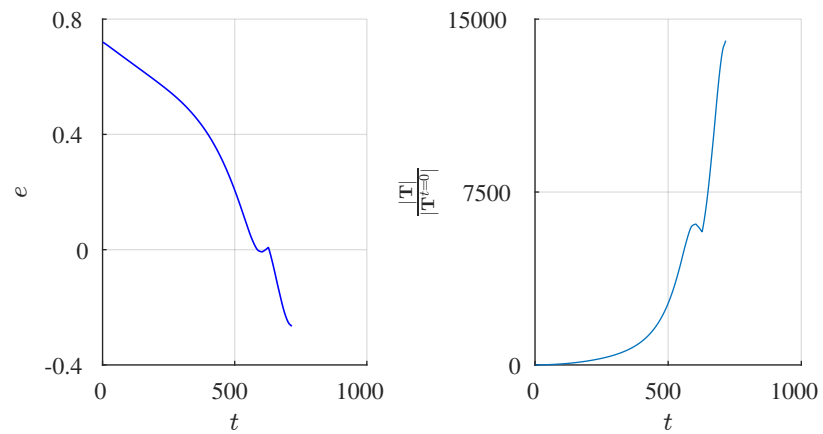


Figure 4.19: Left: changes in void ratio of a particle adherent to the shaft of the cone over time. Right: growth of the norm of stress $|\mathbf{T}|$ normalized by the norm of stress at $|\mathbf{T}^{t=0}|$ for a particle adherent to the shaft of the cone (t has no physical meaning and only represent the progress of calculation)

5 Turbulence in granular solids

5.1 Introduction

In this chapter the vortices that appear in the course of deformation of granular solids is considered. To denote this vorticity we use the word "turbulence", which is established in fluid mechanics. Of course, in fluids turbulence has to do with a surplus of kinetic energy, whereas the motions of sand considered here are slow. Thus, turbulence in granulates is not exactly the same as turbulence in fluids, but in both cases the appearance of vortices is predominant. I do not adopt the word "granulence", that has been proposed Radjai and Roux [43] for turbulence in granulates.

5.2 Element tests and their controllability

"Element tests" are by definition tests with spatially constant stress and deformation. The latter means that the displacements (or velocities) depend in a linear (or affine) way on the spatial coordinates \mathbf{x} . Therefore, an inhomogeneous displacement field is also called a non-affine displacement field.

In order to deduce stress-strain relations from laboratory tests, they must be element test. Otherwise it is not possible to infer the stress and strain from the measured forces and displacements, respectively. For an element test to be "controllable" at a particular stress state \mathbf{T} , one must,

1. prescribe
 - a) the boundary displacements (or velocities) as linear dependent on the boundary coordinates $\mathbf{x}_{\mathcal{B}}$: $\mathbf{v}_{\mathcal{B}} = \mathbf{A}\mathbf{x}_{\mathcal{B}}$, with $\mathbf{A} = \text{const}$, in one part of the boundary, and
 - b) the boundary tractions $\mathbf{t} = \mathbf{T}_{\mathcal{B}}\mathbf{n}_{\mathcal{B}}$ in the complementary part of the boundary.
2. Inequality 5.6 must be fulfilled.

In the words of Revuzhenko, the fulfillment of $\mathbf{v} = \mathbf{A}\mathbf{x}$ on the boundary of an element test implies its fulfillment also in the interior of the sample (provided (i) absence of mass forces and (ii) uniqueness of response) Revuzhenko [44].

It is common in soil mechanics to assume that triaxial tests with smooth end plates are element tests at the beginning of the deformation, until an inhomogeneous mode of deformation (usually a localized shear band) sets on at a certain bifurcation point. In particular, oedometric tests with smooth side walls and end plates are considered as unconditionally controllable, i.e. having homogeneous deformation.

However, smooth side walls and end plates impose the normal velocity but *not* the tangential velocity. Thus, the boundary velocities are *not* fully prescribed. Therefore, *neither oedometric nor triaxial tests are necessarily related with unique deformation of*

sample. This implies that inhomogeneous (non-affine) deformation can appear even at the very beginning of the test and can be manifested with vortices. There is plenty of evidence of vortices in granular media, observed with DIC (digital image correlation) and also with DEM simulations. The special case of shear bands can be interpreted as so-called vortex sheets, i.e. as planar arrays of vortices.

In the laboratory, rigid confinements of a sample are either smooth or, in the ideal case, absolutely rough. In the first case the boundary displacements are not fully prescribed, in the second case no deformation is allowed adjacent to the boundary. In either cases, rigid confinements are inappropriate for element tests.

5.3 Uniqueness of response

Positive second order work implies controllability but not uniqueness of stress in a laboratory test. To show this we consider a constitutive equation of the rate type,

$$\dot{\mathbf{T}} = \mathbf{h}(\mathbf{T}, \mathbf{D}), \quad (5.1)$$

that expresses the stress rate as function of stress \mathbf{T} and stretching \mathbf{D} . This ansatz applies equally to elastoplastic, hypoplastic and barodetic constitutive equations. It can be written also in the form,

$$\dot{\mathbf{T}} = \mathbf{H} \mathbf{D} \quad \text{with} \quad \mathbf{H} := \frac{\partial \mathbf{h}(\mathbf{T}, \mathbf{D})}{\partial \mathbf{D}}, \quad (5.2)$$

with $\mathbf{H}(\mathbf{D})$ being the stiffness matrix. An affine deformation within a sample whose boundary undergoes an affine motion $\mathbf{v}(\mathbf{x}_{\mathcal{B}}) = \mathbf{A} \mathbf{x}_{\mathcal{B}}$ with $\mathbf{A} = \text{const}$ can be obtained under the following condition expressed by Eq. 5.6. Clearly, the affine motion $\mathbf{v} = \mathbf{A} \mathbf{x}$ is a solution of the boundary value problem, if we neglect gravity. We consider whether this solution is unique. Assume that there exists also another solution $\bar{\mathbf{v}} \neq \mathbf{v}$. Denoting differences with the symbol Δ , e.g. $\Delta \mathbf{v} = \mathbf{v} - \bar{\mathbf{v}}$, we observe that $\Delta \mathbf{v}$ vanishes at the boundary. The equilibrium equation reads $\nabla \cdot \mathbf{T} = \mathbf{0}$, and continued equilibrium reads $\nabla \cdot \dot{\mathbf{T}} = \mathbf{0}$. The same equations hold also for the stress difference $\Delta \mathbf{T} := \mathbf{T} - \bar{\mathbf{T}}$: $\nabla \cdot \Delta \mathbf{T} = \mathbf{0}$ and $\nabla \cdot \Delta \dot{\mathbf{T}} = \mathbf{0}$. Now we consider the integral $I := \int_V \nabla \cdot (\Delta \dot{\mathbf{T}} \Delta \mathbf{v}) dV$ and apply the theorem of Gauss. We thus obtain, that this integral vanishes,

$$\int_V \nabla \cdot (\Delta \dot{\mathbf{T}} \Delta \mathbf{v}) dV = \int_S \Delta \dot{\mathbf{T}} \Delta \mathbf{v} \cdot \mathbf{n} dS = 0, \quad (5.3)$$

because $\Delta \mathbf{v} = \mathbf{0}$ on the surface S . Further,

$$I = \int_V \nabla \cdot (\Delta \dot{\mathbf{T}} \Delta \mathbf{v}) dV = \int_V \Delta \mathbf{T} \nabla \cdot \Delta \mathbf{v} dV + \int_V \Delta \mathbf{v} \nabla \cdot \Delta \dot{\mathbf{T}} dV = 0. \quad (5.4)$$

The second integral on the right hand side vanishes due to continued equilibrium. Thus, for non-uniqueness must hold,

$$\int_V \Delta \dot{\mathbf{T}} \cdot \nabla \Delta \mathbf{v} dV \equiv \int_V \Delta \dot{\mathbf{T}} \cdot \Delta \mathbf{D} dV = 0, \quad (5.5)$$

which is impossible if $\Delta \dot{\mathbf{T}} \cdot \Delta \mathbf{D} > 0$ holds everywhere (the notation $\Delta \dot{\mathbf{T}} \cdot \Delta \mathbf{D}$ denotes the same as $\text{tr}(\Delta \dot{\mathbf{T}} \Delta \mathbf{D})$). Hence the condition,

$$\text{tr}(\Delta \dot{\mathbf{T}} \Delta \mathbf{D}) > 0, \quad (5.6)$$

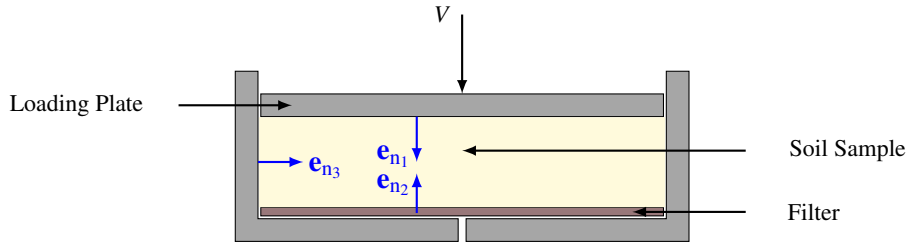


Figure 5.1: Schematic illustration of the oedometric test

implies uniqueness. For the special case $\bar{\mathbf{v}} = \mathbf{0}$ we have: $\text{tr}(\Delta \dot{\mathbf{T}} \Delta \mathbf{D}') = \text{tr}(\dot{\mathbf{T}} \mathbf{D})$. Hence, $\text{tr}(\Delta \dot{\mathbf{T}} \Delta \mathbf{D}) > 0$ implies positive second order work: $\text{tr}(\dot{\mathbf{T}} \mathbf{D}) > 0$, but the latter condition does not imply uniqueness.

Consider for example the oedometric test (Fig. 5.1) whose boundary conditions are kinematic. It is generally assumed that the deformation of a sand sample in the oedometer is homogeneous. However, this is not necessary, as already mentioned, since the tangential velocity along the walls is not prescribed. We decompose the velocity \mathbf{v} in the mean velocity $\bar{\mathbf{v}}$ and its fluctuation \mathbf{v}' :

$$\mathbf{v} = \bar{\mathbf{v}} + \mathbf{v}'. \quad (5.7)$$

With \mathbf{e}_{n_1} , \mathbf{e}_{n_2} and \mathbf{e}_{n_3} being the unit normal vectors at the upper plate, lower plate and side wall, respectively, the boundary conditions read,

$$\mathbf{v} \cdot \mathbf{e}_{n_1} = \bar{\mathbf{v}} \cdot \mathbf{e}_{n_1} = V, \quad \mathbf{v}' \cdot \mathbf{e}_{n_1} = 0, \quad (5.8)$$

$$\mathbf{v} \cdot \mathbf{e}_{n_2} = \bar{\mathbf{v}} \cdot \mathbf{e}_{n_2} = \mathbf{v}' \cdot \mathbf{e}_{n_2} = 0, \quad (5.9)$$

$$\mathbf{v} \cdot \mathbf{e}_{n_3} = \bar{\mathbf{v}} \cdot \mathbf{e}_{n_3} = \mathbf{v}' \cdot \mathbf{e}_{n_3} = 0, \quad (5.10)$$

$$(5.11)$$

where V is the vertical velocity of the piston. Consequently, the velocity fluctuation \mathbf{v}' is tangential to all boundaries. According to a theorem by Kelvin and Helmholtz on the impossibility of irrotational motions in general (cited by Truesdell [55], section 37), the field \mathbf{v}' is in this case either rotational or zero. The latter case corresponds to the homogeneous deformation, which is of course possible.

5.4 Vortices observed in physical tests

Vortices can be observed in laboratory tests with Digital Image Correlation (DIC). The vortices appear in the fields of velocity fluctuations $\mathbf{v}' = \mathbf{v} - \bar{\mathbf{v}}$. In Fig. 5.2 velocity fluctuations in a $1\gamma 2\varepsilon$ -apparatus are demonstrated. In Figs. 5.3 and 5.4 the vortices in a biaxial test in softening regime and critical state, respectively, are presented.

¹Geotechnique Letters by Institution of Civil Engineers (Great Britain) Reproduced with permission of Thomas Telford, Ltd. in the format Republish in a thesis/dissertation via Copyright Clearance Center.

²GRANULAR MATTER by SPRINGER-VERLAG. Reproduced with permission of SPRINGER-VERLAG in the format Thesis/Dissertation via Copyright Clearance Center.

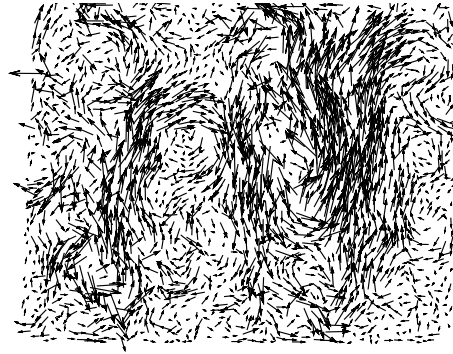


Figure 5.2: Velocity fluctuations obtained with Digital Image Correlation in $1\gamma_2\varepsilon$ -apparatus filled with rods, Richefeu et al. [45]¹

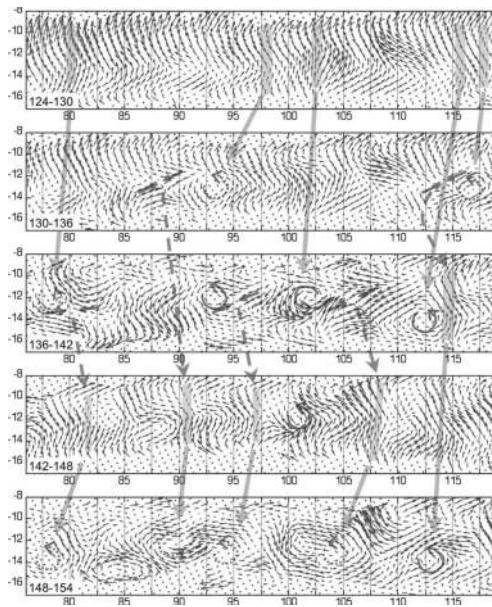


Figure 5.3: Post-peak (softening) sequence of velocity fluctuations within shear bands in biaxial tests with dense sand, obtained with Digital Image Correlation, Abedi et al. [1]²

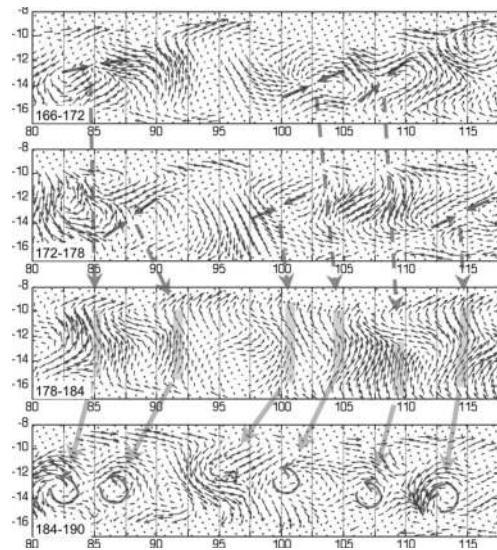


Figure 5.4: Post-peak (residual or critical state) sequence of velocity fluctuations within shear bands in biaxial tests with dense sand, obtained with Digital Image Correlation, Abedi et al. [1]²

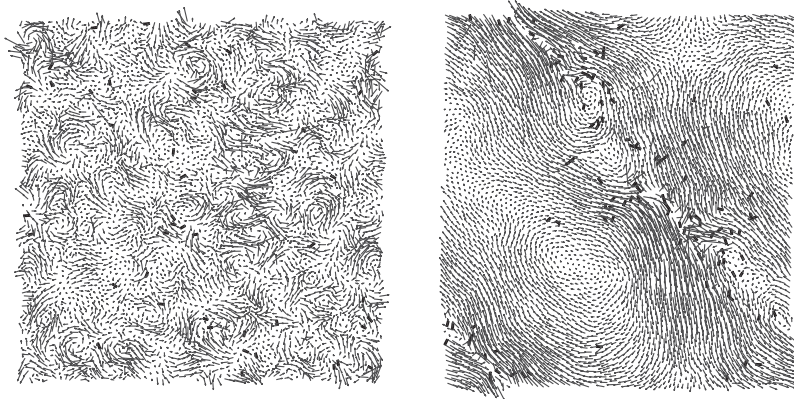


Figure 5.5: Velocity fluctuations in simple shear simulated with DEM by Thornton, left: start of shear, right: at 8% shear strain, Thornton and Zhang [53]³

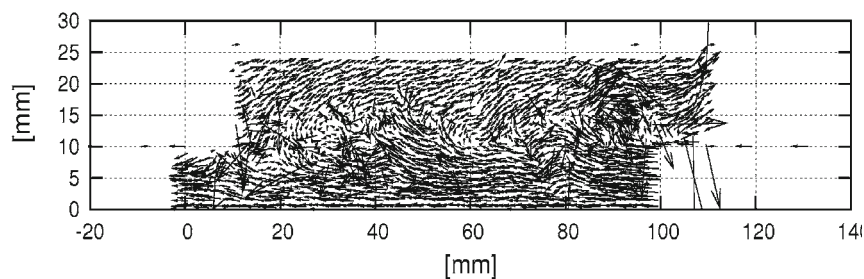


Figure 5.6: Vortex structures obtained with DEM simulation of a direct shear test, Kozicki et al. [32]²

5.5 Vortices obtained with DEM simulations

Admittedly, DEM simulations do not necessarily mirror the reality. However, they often reveal realistic pictures of the deformation. There are several reports on vortices in the fluctuation velocity fields, obtained with DEM, such as the ones shown in Fig. 5.5 for simple shear test, in Fig. 5.6 for direct shear test and in Fig. 5.7 in a triaxial test.

5.6 Numerical simulation of vortices with SPARC

Firstly, the oedometric test is chosen for our demonstrations, because it is generally believed that this test has a homogeneous (affine) deformation, whereas we prove here that this is not necessarily the case. In our numerical simulations we consider lengthy oedometric samples, which are unusual, because the vortices, the diameter of which depends on the dimensions of the container, are there more pronounced.

In order to demonstrate that the formation of vortices is independent from the applied

³Philosophical Magazine Reproduced with permission of Taylor & Francis in the format Thesis/Dissertation

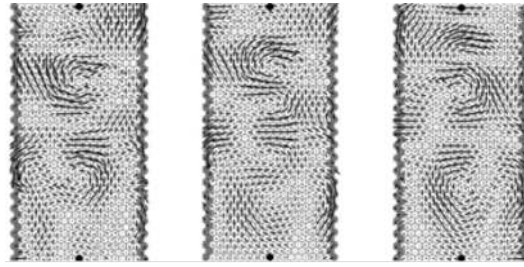


Figure 5.7: Velocities in a triaxial test sample with bender elements, numerical simulations with DEM, O'Donovan et al. [40]²

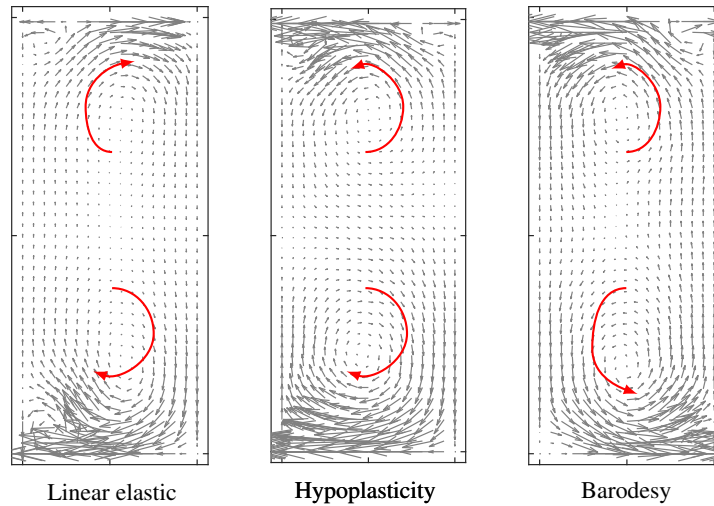


Figure 5.8: Comparison of vortices for three different material models in oedometric test

material model, firstly a comparison of an oedometric test with smooth upper and lower plates with three different material models is shown in Fig. 5.8. The three material models are, (i) linear elastic with $E = 1000$ MPa and $\nu = 0.25$, (ii) hypoplastic material model after von Wolffersdorff 1996 described in Sec. A.2.3 and (iii) barodesy after Kolymbas 2015, described in Sec. A.2.2. The results show that regardless of the selected material model, the vortices follow almost the same pattern. We consider now oedometric, biaxial and simple shear tests simulated with the material model after Kolymbas 2015, described in Sec. A.2.2. The stress-strain relationships of oedometer, true biaxial and simple shear tests with the above mentioned material model is shown in Fig. 5.9. In Fig. 5.10 we show the development of vortices with increasing deformation in an oedometric test with rough upper and lower plates. No particular pattern of the vortices can be detected and the vortices look different with increasing ε_{zz} . Since Fig. 5.10-f, gives the impression of non-vanishing fluctuations adjacent and normal to the upper plate, a zoom of this figure at the upper plate is plotted in Fig. 5.11.

In Fig. 5.12 the development of vortices with increasing deformation in an oedometric test with smooth upper and lower plates is plotted. In contrast to Fig. 5.10 an almost constant pattern of vortices can be detected in this case. The vortices are mainly formed at

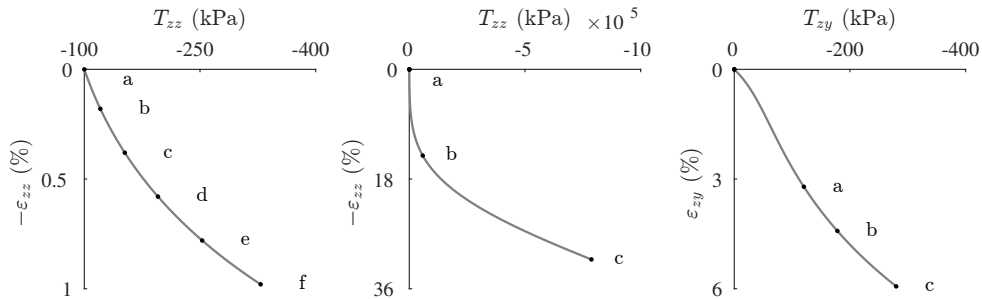


Figure 5.9: Stress-strain curves for oedometer (left), true biaxial (middle) and simple shear simulations (right), respectively

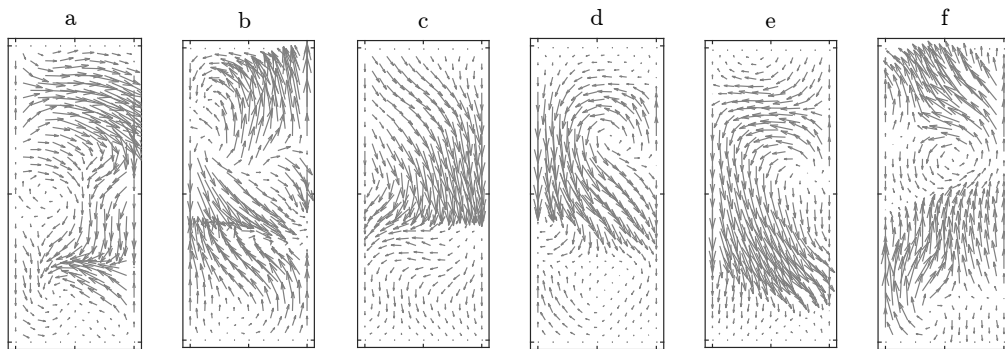


Figure 5.10: Development of vortices with increasing oedometric deformation, at the strains indicated in Fig. 5.9 - left, rough upper and lower plates. Fig. f gives the impression of non-vanishing normal fluctuations adjacent to the upper plate. Therefore, a zoom is plotted in Fig. 5.11

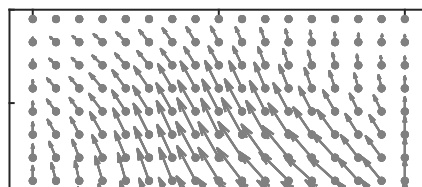


Figure 5.11: Zoom in of Fig. 5.10-f

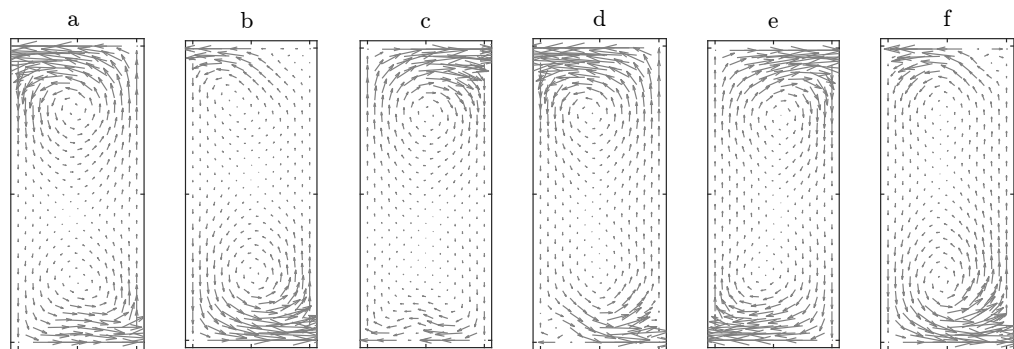


Figure 5.12: Development of vortices with increasing oedometric deformation, at the strains indicated in Fig. 5.9 - with smooth upper and lower plates

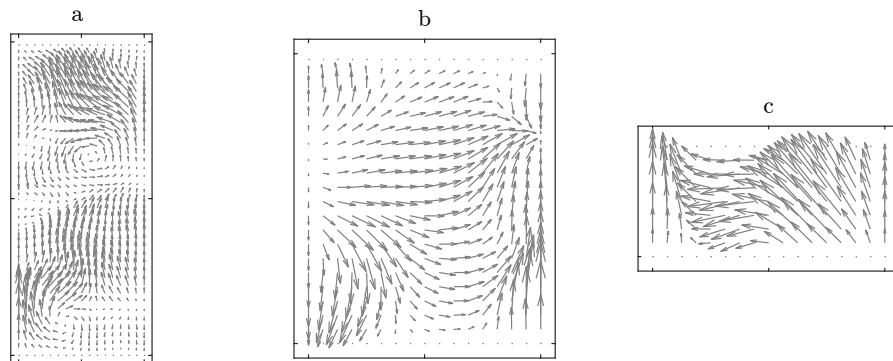


Figure 5.13: Influence of the sample size, a) $h_0/B = 2.5$, b) $h_0/B = 1.25$ and c) $h_0/B = 0.5$ - rough upper and lower plates

the upper and lower plates with a rotational pattern and lose their intensity in the middle of the sample.

In Fig. 5.13 the effect of the dimension of the model on the development of the vortices in an oedometric test with rough upper and lower plates is offered.

In Fig. 5.14 the influence of density of the particles on the vortices is shown. It can be seen that vortices are still detectable for large values of d (less number of particles). However the vortices have a simpler pattern and as the spacing (d) gets smaller and the number of particles increases the vortices become more complex.

In Fig. 5.15 is the development of vortices with increasing deformation in a true biaxial test shown. At the beginning of the deformation, Fig. 5.15-a, the vortices show a simple pattern of rotation. With increasing deformation, the vortices form an almost symmetrical pattern with rotations in opposite directions.

In Fig. 5.16 the development of vortices with increasing deformation in a simple shear test is shown⁴. In Fig. 5.16-a, at the beginning of the deformation, the vortices show a rotational pattern. However with increasing deformation, the rotational shape of vortices disappears and the vortices move to the top left of the sample.

⁴Simulation of simple shear test is conducted by considering the convective acceleration, see Sec. B.7.

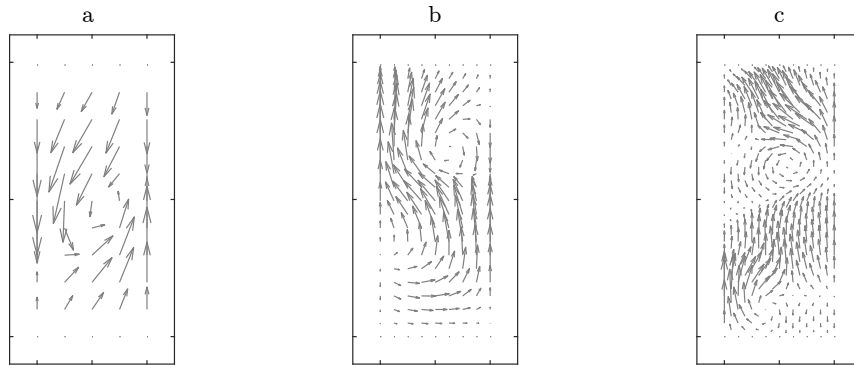


Figure 5.14: Influence of the density of particles (initial spacing size d in the oedometric test simulation) a) $d = 50$ mm, b) $d = 25$ mm and c) $d = 12.5$ mm - rough upper and lower plates

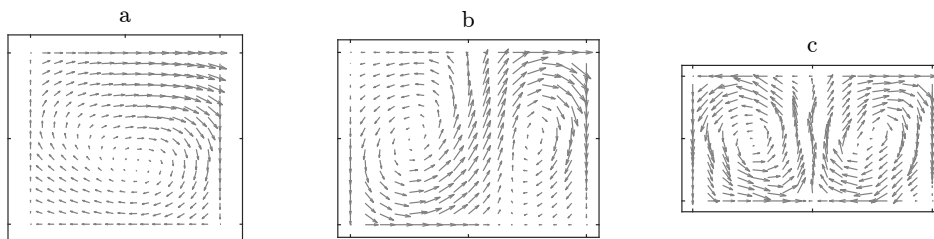


Figure 5.15: Development of vortices with increasing biaxial deformation at the strains indicated in Fig. 5.9 - middle

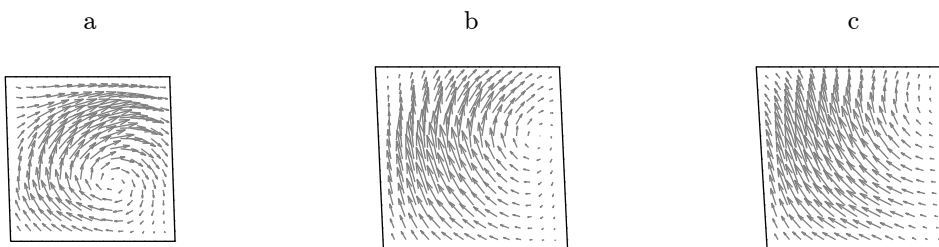


Figure 5.16: Development of vortices with increasing simple shear deformation at the strains indicated in Fig. 5.9 - right

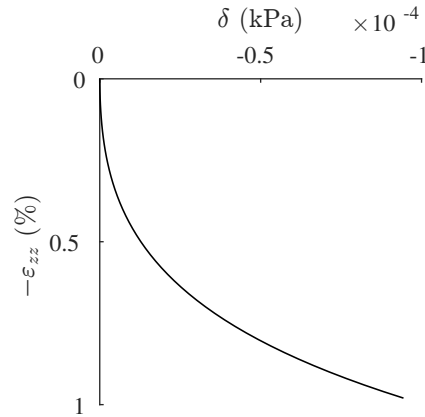


Figure 5.17: Effect of turbulences on the stress-strain relationship - development of difference in T_{zz} with increasing oedometric deformation

5.7 Physical explanation of the vortices

The superposition of vortices to an affine deformation imply a superimposed shear, and this reduces the volumetric stiffness and, consequently, also the overall stiffness of contractant media. In microscopic terms, the irreversible deformation of granulates is related to rearrangement of "rigid" grains, which can hardly occur with affine deformations. Thus, vortices may originate from grain re-arrangement, see also Tordesillas et al. [54].

5.8 Implications for element tests

For an oedometric test, the stress-strain curve obtained from direct integration of the material model is compared with the one from SPARC, by which the state variables are influenced from the turbulences (see Fig. 5.17-a). The mean value of T_{zz} for the simulation with turbulences is calculated as follows,

$$\bar{T}_{zz} = \frac{\int_{y_{\min}}^{y_{\max}} T_{zz} \cdot dy}{y_{\max} - y_{\min}}, \quad (5.12)$$

where y_{\min} and y_{\max} represent the horizontal boundaries of the model. In Fig. 5.17-b, δ demonstrates the difference in the vertical stresses T_{zz} with and without vortices. Obviously, this difference is very small.

5.9 Ptygmatic folds

Ptygmatic folds are a peculiar pattern of folding in rock (see Fig. 5.18). The general assumption is that ptygmatic folds occur when a sheet of stiffer rock (termed as "competent") is confined by a softer host material and undergoes plastic deformation, according

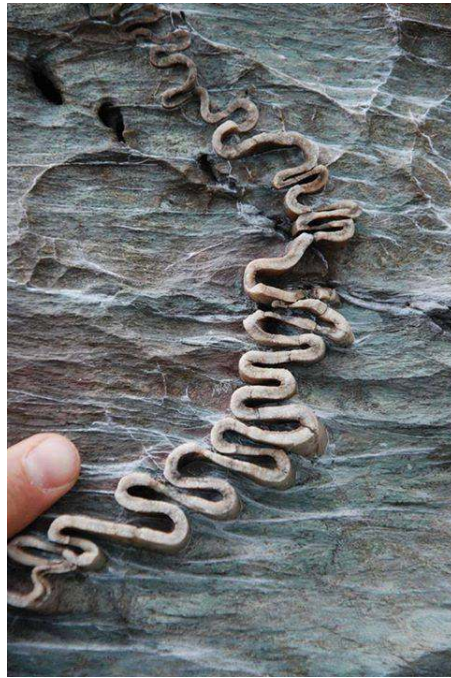


Figure 5.18: Ptygmatic fold in rock⁵

to Godfrey [17]. Here we show that ptygmatic folds can be a consequence of turbulent deformations of geomaterials.

5.9.1 Simulation of ptygmatic folds with SPARC

Ghosh [16] conducted several experiments with plastic materials such as modeling clay for investigation on formation of ptygmatic folds. Ghosh's experiments were mainly conducted in simple shear test. The results of his investigations are demonstrated in Figs. 5.19.

For the simulation of ptygmatic folds with SPARC a model of simple shear test with initial height of 50 cm and width of 10 cm in plane strain condition has been simulated (see Fig. 5.20). The gray particles in Fig. 5.20 have an initial void ratio of $e_0 = 0.5$ and the red ones on the material line at $y = 0.05$ m have an initial void ratio of $e_0 = 0.4$. The lower void ratio for the red particles leads to a more competent behavior of the material line ($y = 0.05$ m) in comparison to the host gray particles. A homogeneous setup is also simulated, by which all particles have the same initial void ratio of $e_0 = 0.5$. The simulation is repeated for a homogeneous setup in order to investigate if the appearance of ptygmatic folds is due to the presence of a competent material confined by less competent host material or not. The material model of barodesy for clay introduced in Sec. A.2.4 with the calibration for Dresden clay (see Tab. A.4) is applied for the simulation.

⁵Outcropedia Reproduced with permission of photographer: Rodolfo Carosi, University of Torino.

⁶Tectonophysics by ELSEVIER BV. Reproduced with permission of ELSEVIER BV in the format Thesis/Dissertation via Copyright Clearance Center.

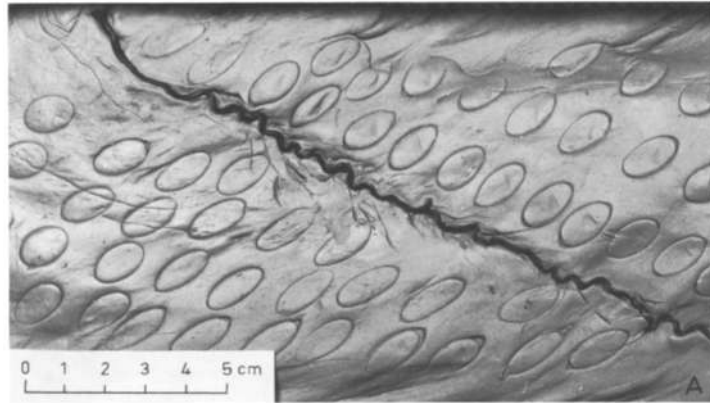


Figure 5.19: Ptygmatic fold in modeling clay under simple shear deformation (adapted from Ghosh [16])⁶

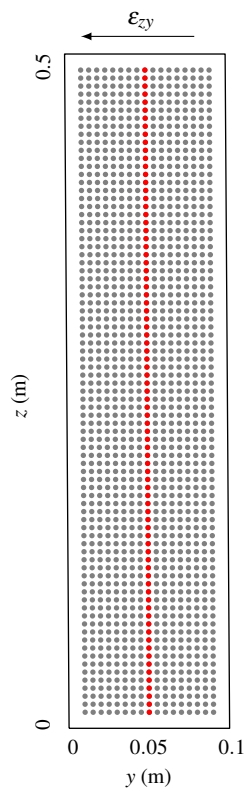


Figure 5.20: Geometry of the model, the red particles in the middle of the model represent the "competent material line" with reduced void ratio of $e_0 = 0.4$, the gray host particles have an initial void ratio of $e_0 = 0.5$

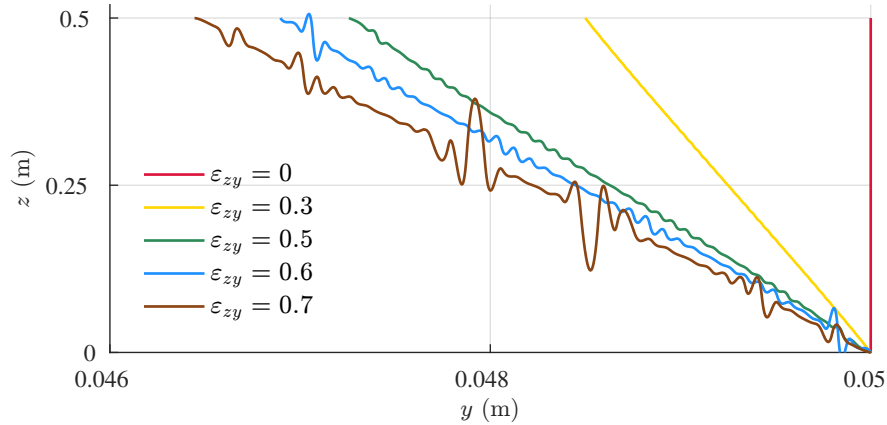


Figure 5.21: Deformation of material line ($y = 0.05$ m) in simple shear test for setup with competent material

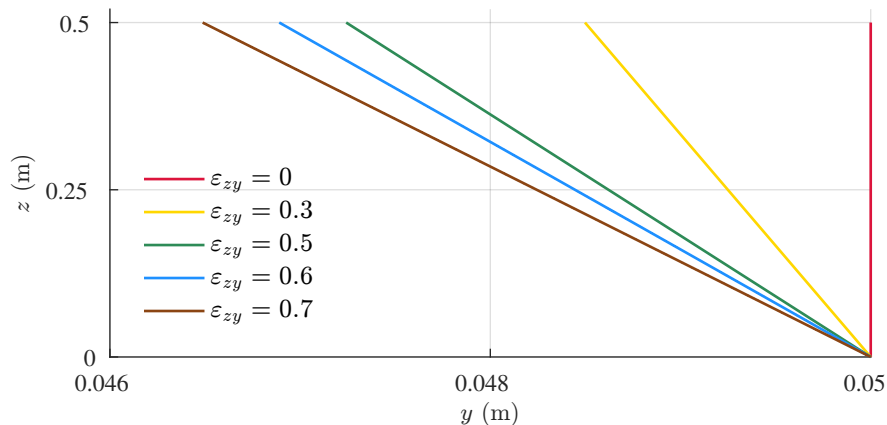


Figure 5.22: Deformation of material line ($y = 0.05$ m) in simple shear test for homogeneous setup

Results

The deformation of the material line ($y = 0.05$ m line in Fig. 5.20) with increasing shear strain (ϵ_{zy}) is plotted in Fig. 5.21. The material shows minute folds at $\epsilon_{zy} = 0.3$. However as the sample is sheared further, the ptygmatic folds along the material line become more apparent until for $\epsilon_{zy} = 0.7$ the fold becomes significant. The obtained ptygmatic fold under simple shear deformation is comparable with the experimental results of Gosh demonstrated in Fig. 5.19.

In Fig. 5.22, the deformation of the material line ($y = 0.05$ m) for homogeneous setup and increasing shear strain is plotted. In contrast to Fig. 5.21, no folds can be detected along the material line and which keeps its initial form throughout the simulation.

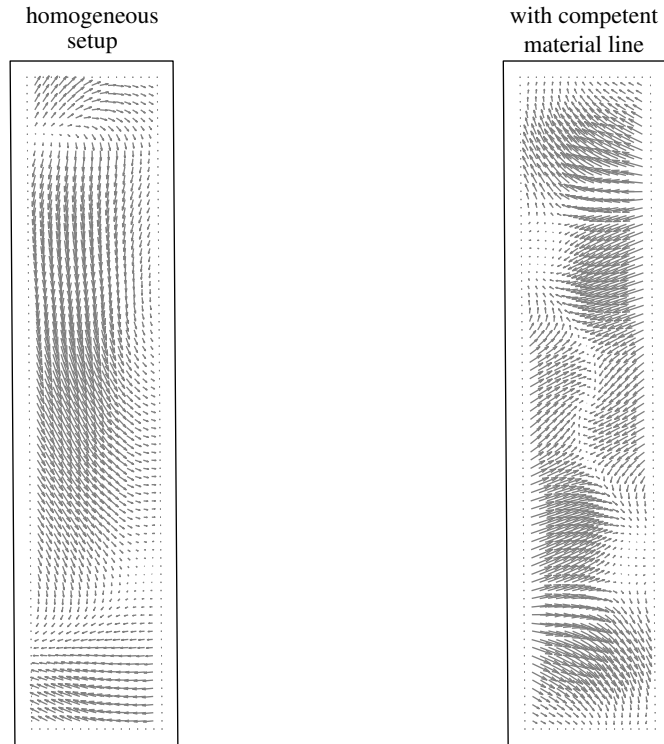


Figure 5.23: Comparison of vortices for homogeneous setup (left) and setup with competent material line (right), $\varepsilon_{z\gamma} = 0.7$

In Fig. 5.23, the vortices at $\varepsilon_{z\gamma} = 0.7$ are compared for the simulation with homogeneous setup and the simulation with the competent material line. The vortices differ from each other clearly and in case of the setup with competent material line, the vortices are in correspondence with the deformed material line in Fig. 5.21.

The question arises why no ptygmatic folds can be detected in Fig. 5.22, although vortices for the homogeneous setup (Fig. 5.23, left) are detectable. This question can be answered by investigating the intensity of vortices. In Fig. 5.24, the norm of turbulence, $|\mathbf{v}'|$, is plotted for different variations in the void ratio of the competent material line, where $\Delta e = 0$ represents the homogeneous setup and $\Delta e = 20\%$ means $e_0 = 0.4$ for the competent material line. As it can be seen, for $\Delta e = 0$, the norm of fluctuation becomes very small ($|\mathbf{v}'| = 1.5 \times 10^{-13}$ m/s) and with increasing Δe , the intensity of fluctuation becomes 4×10^9 times larger and reaches $|\mathbf{v}'| = 6 \times 10^{-4}$ m/s.

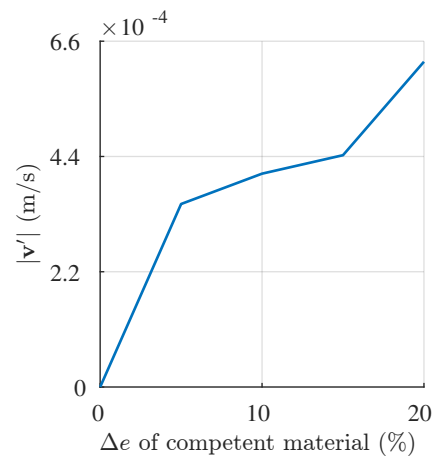


Figure 5.24: Fluctuation (v') in dependence of void ratio of the competent material line, $\Delta e = 0$ represents the homogeneous setup and $\Delta e = 20\%$ means $e_0 = 0.4$ for the competent material line

6 Summary and outlook

6.1 Summary

In the first chapter, the framework of Soft PARTicle Code (SPARC) and its improvements in the scope of this work are presented. The reconditioning of the solution, defining the smooth boundary condition and consideration of the convective acceleration have proved to be effective for the simulations in this work. Concerning the interpolation methods, a comparison of three different interpolation functions has been conducted and the results have been compared with the analytical (exact) solution. It has been shown that first order polynomial without the constant term and with the least number of required neighbors delivers the more accurate and smoother derivatives and has therefore been applied for all the simulations in this study.

In the second chapter, firstly a numerical case study for oedometric and triaxial tests regarding the number of particles and the loading/unloading velocity is presented. It has been shown that the results are in agreement with the element test, as long as the deformations are homogeneous. However, in case of the triaxial test, where the deformations become inhomogeneous, the solver suffers from convergence problems and the successful simulation of the triaxial test is not always possible. In the second part of chapter two, the formation of shear bands in clay is simulated. Results show that SPARC is capable of modeling shear bands and that the number of particles has influence on the shape, thickness and inclination of the shear bands.

In the third chapter, punching into sand is simulated. The two improvements of reconditioning the solution and defining the smooth boundary condition were helpful in successful simulation of punching with SPARC. The results have been validated by comparing them with the experimental results. SPARC has been able to predict the peak of the load-displacement curve at the same penetration depth obtained in the experiments. Furthermore, the shape of the slide planes formed under the foundation are comparable with the experimental and analytical results.

In the fourth chapter, firstly a brief description of former studies on cone and pile penetration is provided. In the second part, it has been attempted to simulate the cone penetration with SPARC. Two different smooth boundary conditions followed by an adherent particle boundary condition have been introduced and the results are compared. The deepest penetration could be achieved with adherent particles. The results show that the proposed boundary conditions are not appropriate for the this problem and further investigations

in this direction are required.

In the fifth chapter, SPARC has been applied for derivation of vortex patterns in deformations which were beforehand believed to be homogeneous. These results are of importance, since it is the first time (to my knowledge) that a numerical method based on continuum mechanics has been employed for this purpose. The effect of turbulent deformations on pygamic folds is studied by simulating a simple shear test with a competent material line and the obtained vortices are compared with the vortices acquired for a homogeneous material.

In appendix A, the basics of barodesy are explained and a list of all the material models which were used in this study with their calibration is presented.

In appendix B, a comprehensive explanation of the unsuccessful attempts for the simulation of cone penetration is provided. Although these attempts have been unsuccessful, they can form a basis for further research going in this direction.

6.2 Outlook

The mediocre simulation of cone penetration with SPARC in the present work prompts motivation for further research. The present research has proved that the problem of cone penetration demands a more advanced boundary condition for the cone. It must be mentioned that contact problems and roughness are of importance in numerical simulation of problems in soil mechanics and extra effort in this direction would be worthy.

A further improvement of the present code would be the incorporation of interpolation methods which are capable of delivering smoother results. A number of attempts were made in this direction (see Secs. B.4, B.5, B.9, and B.10), however, they did not prove to be beneficial. One of the main deficiencies of the current interpolation methods is that they cannot make good approximations when the deformations become large or when the particles change neighbors.

Another relevant research would be in the direction of improving the solution finding procedure in SPARC. It has been shown that e.g. for the problem of punching, the reconditioning of the solution at the peak of the load-settlement curve was helpful and afterwards the solver could continue without reconditioning. Therefore, the author suggests taking into account such provisional improvements for the Newton solver which can be applied over a number of time steps when required (e.g. see Sec. B.8).

Another further development of the code would be to implement an algorithm which continuously checks for the quality of the approximation of spatial derivatives and adds or removes particles accordingly.

SPARC is in its early years of development and it can be improved in many dimensions. A number of modifications have been made based on the above-mentioned suggestions, however due to time limitations, other solutions and ideas could not have been examined.

A Material models

The balance equations and boundary conditions introduced in Chp. 1 are not sufficient for solving the problems of continuum mechanics. Material models, as explained in Sec. 1.5, are required in order to take into account the changes in the stress tensor due to the deformations. In this chapter we explain the basics of hypoplastic material models, especially the barodetic material models. In this work simulations are conducted and compared for sand and clay. For the simulations with sand two versions of barodesy are applied introduced by Kolymbas in [25], [28] and the hypoplastic material model introduced by von Wolffersdorff [58]. Barodesy for clay, as a modification of the original barodesy introduced by Medicus and Fellin [37] is used for simulations with clay.

A.1 Basics of barodesy

Barodesy is based on two fundamental experimental findings for sand, referring to proportional paths. Proportional stress and strain paths are paths that maintain constant ratios of the principal values $T_1 : T_2 : T_3$ and $\varepsilon_1 : \varepsilon_2 : \varepsilon_3$, respectively. The following rules were derived by Goldscheider [18],

- starting from the stress-free state, proportional strain paths lead to proportional stress paths,
- starting from a non stress-free state, while applying a proportional strain path, the stress state leads asymptotically to the proportional stress path obtained from the stress-free state.

In Fig. A.1, the first rule is demonstrated for four different proportional strain paths. The first proportional stress path is the isotropic compression, by which the sample is compressed in both principal directions equally and leads to i stress path in Fig. A.1, right. For the oedometric proportional strain path, the K_0 stress path is obtained. Lastly for the isochoric compression and extension paths the critical state lines, characterized by $+c$ and $-c$ are acquired.

In Fig. A.2, the second rule is demonstrated. For a non stress-free state, the black point in Fig. A.2 right, if a proportional strain path is applied to the sample, e.g. oedometric compression or isochoric extension, the stress state approaches asymptotically the stress path obtained for the stress-free condition.

In barodesy, a tensor which defines the direction of a proportional stress path as a function of the rate of deformation is denoted by \mathbf{R} . However, since the function \mathbf{R} denotes only the direction, therefore it must be a function of the normalized rate of deformation \mathbf{D}^0 .

$$\mathbf{R}(\mathbf{D}) = \mathbf{R}(\mathbf{D}^0) \quad (\text{A.1})$$

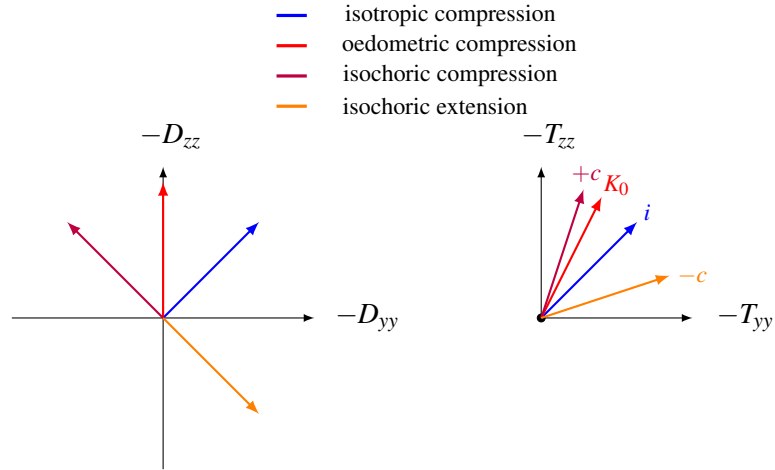


Figure A.1: Illustration of the first rule for isotropic compression, oedometric compression, isochoric compression and isochoric extension - beginning from the stress-free state, proportional strain paths lead to proportional stress paths, D_{zz} and D_{yy} are the components of the stretching tensor \mathbf{D}

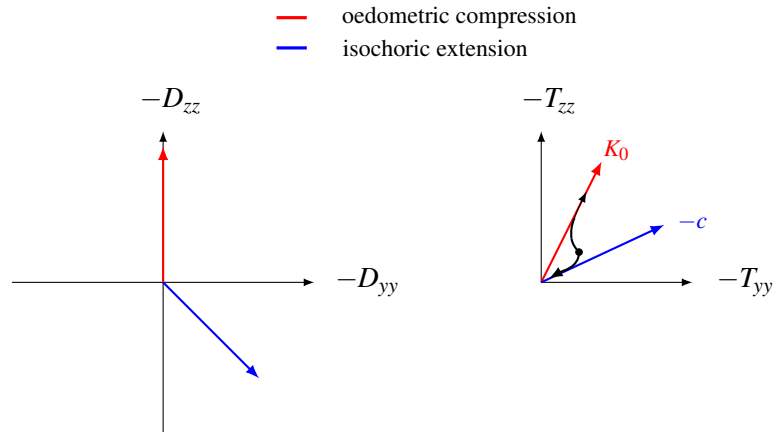


Figure A.2: Illustration of the second rule - starting from a non stress-free state and applying a proportional strain path (e.g. oedometric or isochoric extension), the stress state leads asymptotically to the proportional stress path obtained from the stress-free state

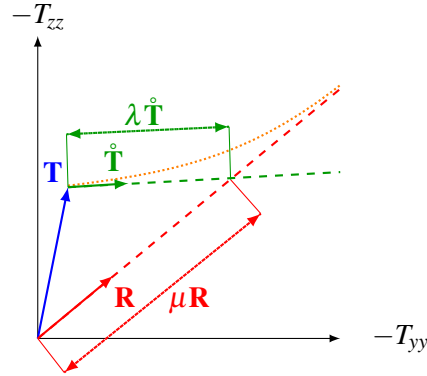


Figure A.3: Mathematical interpretation of the second rule

Fig. A.3 states that from a non-zero stress state, ($\mathbf{T} \neq \mathbf{0}$), changes in the stress ($\dot{\mathbf{T}}$) are so that the stress state asymptotically reaches the proportional stress path predicted by \mathbf{R} . Therefore, if $\dot{\mathbf{T}}$ and \mathbf{R} are multiplied with the scalars λ and μ we can write,

$$\mathbf{T} + \lambda \dot{\mathbf{T}} = \mu \mathbf{R}(\mathbf{D}). \quad (\text{A.2})$$

If we eliminate $\dot{\mathbf{T}}$ from Eq. A.2, a general evolution equation for the stress is obtained,

$$\dot{\mathbf{T}} = v_1 \mathbf{R}(\mathbf{D}) + v_2 \mathbf{T}, \quad (\text{A.3})$$

where v_1 and v_2 are scalar values which are determined in compliance with barotropy (dependence of material behavior on stress $|\mathbf{T}|$) and pyknotropy (dependence of material behavior on density/void ratio). For detailed determination of the scalar values the reader is referred to Kolymbas [28].

The final barodectic equation has the following form,

$$\dot{\mathbf{T}} = h(f\mathbf{R}^0 + g\mathbf{T}^0)|\mathbf{D}|, \quad (\text{A.4})$$

where $h(\mathbf{T})$ is responsible for stiffness and the scalar values f and g , as discussed earlier are so determined to model the mechanical behavior of granular materials. The scalar values f and g are mainly determined so that the material model can reproduce soil behavior at peak and in critical state. As demonstrated in Fig. A.4, at the peak of the stress-strain curve, the rate of stress $\dot{\mathbf{T}}$ vanishes. Furthermore, volume changes are positive, which means that $\text{tr}(\mathbf{D}^0)$ as a measure of dilatancy must be positive and the void ratio is smaller than the critical void ratio e_c . On the other hand, when soil reaches the critical state (see Fig. A.4), the stress state $\dot{\mathbf{T}}$ and volume changes must vanish simultaneously, which requires $\dot{\mathbf{T}}$ and $\text{tr}(\mathbf{D}^0)$ to become equal to zero. Lastly, the void ratio must also reach the value of void ratio at the critical state, i.e. $e = e_c$.

A.2 Applied material models

In Sec. A.1 an insight into the experimental and mathematical principles of the barodectic material models was offered. Interested readers can refer to Kolymbas [27], Kolymbas [25], Kolymbas [30], Kolymbas [26], Kolymbas [28], Fellin [14], Kolymbas [27],

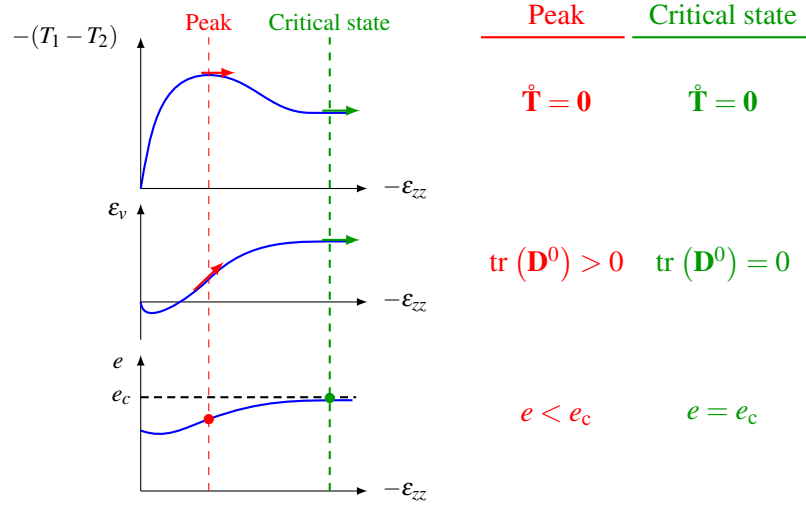


Figure A.4: Demonstration of state variables at peak and critical state for a dense sample

c_1	c_2	c_3	c_4	c_5	c_6	e_{c0}
-0.8	-0.9	0.6	-5000	-3000	1000	0.78

Table A.1: Calibration of barodesy for sand after Kolymbas (2011) for Hostun sand [25]

Medicus [36], Medicus and Fellin [37] for further information about barodesy for sand and clay. In the rest of this chapter, the main equations of the material models used in this study are explained with their calibration. It must be mentioned that the calibration constants are offered for stresses in kPa.

A.2.1 Barodesy: a new hypoplastic approach, Kolymbas (2011)

The barodetic model reads,

$$\dot{\mathbf{T}} = h(\mathbf{T}) \cdot (f\mathbf{R}^0 + g\mathbf{T}^0) \cdot |\mathbf{D}|, \quad (\text{A.5})$$

where,

$$h(\mathbf{T}) = |\mathbf{T}|^{c_3}, \quad (\text{A.6})$$

$$\mathbf{R}(\mathbf{D}) = (\text{tr}\mathbf{D}^0) \mathbf{1} + c_1 \exp(c_2 \mathbf{D}^0), \quad (\text{A.7})$$

$$f = c_4 \text{tr}(\mathbf{D}^0) + c_5(e - e_c) + c_6, \quad (\text{A.8})$$

$$g = -c_6, \quad (\text{A.9})$$

$$e_c = (1 + e_{c0}) \exp\left(\frac{|\mathbf{T}|^{1-c_3}}{c_4(1-c_3)}\right) - 1. \quad (\text{A.10})$$

For the simulations in this study, the calibration of barodesy for Hostun sand is used with the constants summarized in Tab. A.1.

c_1	c_2	c_3	c_4	c_5	e_{c0}	e_{\min}
-1.0246	1	-2.3	465	28	0.87	0.35

Table A.2: Calibration of barodesy for sand after Kolymbas (2015) for Hostun sand [28]

A.2.2 Introduction to Barodesy, Kolymbas (2015)

The barodetic model reads,

$$\dot{\mathbf{T}} = h(\mathbf{T}) \cdot (f\mathbf{R}^0 + g\mathbf{T}^0) \cdot |\mathbf{D}|, \quad (\text{A.11})$$

where,

$$h = -\frac{c_4 + c_5|\mathbf{T}|}{e - e_{\min}}, \quad (\text{A.12})$$

$$f = \text{tr}(\mathbf{D}^0) + c_3 e_c, \quad (\text{A.13})$$

$$\mathbf{R} = -\exp [c_1 \exp (c_2 \cdot \text{tr}(\mathbf{D}^0)) \mathbf{D}^0], \quad (\text{A.14})$$

$$g = -c_3 e, \quad (\text{A.15})$$

$$e_c = \frac{e_{\min} + B}{1 - B}, \quad (\text{A.16})$$

$$B = \frac{e_{c0} - e_{\min}}{e_{c0} + 1} \left(\frac{c_4 + c_5 \cdot |\mathbf{T}|}{c_4} \right)^{-(1+e_{\min})/c_5}. \quad (\text{A.17})$$

A.2.3 Hypoplastic relation of von Wolffersdorff (1996)

$$\dot{\mathbf{T}} = f_b f_e \frac{1}{\text{tr}(\hat{\mathbf{T}}^2)} \left\{ F^2 \mathbf{D} + a^2 \text{tr}(\hat{\mathbf{T}} \cdot \mathbf{D}) \cdot \hat{\mathbf{T}} + f_d \cdot a \cdot F \cdot (\hat{\mathbf{T}} + \hat{\mathbf{T}}^*) \cdot |\mathbf{D}| \right\}, \quad (\text{A.18})$$

$$\hat{\mathbf{T}} = \frac{\mathbf{T}}{\text{tr} \mathbf{T}}, \quad (\text{A.19})$$

$$\hat{\mathbf{T}}^* = \hat{\mathbf{T}} - \frac{1}{3} \mathbf{I}, \quad (\text{A.20})$$

$$a = \frac{\sqrt{3}(3 - \sin \varphi_c)}{2\sqrt{2} \sin \varphi_c}, \quad (\text{A.21})$$

$$F = \sqrt{\frac{1}{8} \tan^2 \psi + \frac{2 - \tan^2 \psi}{2 + \sqrt{2} \tan \psi \cos 3\theta}} - \frac{1}{2\sqrt{2}} \tan \psi, \quad (\text{A.22})$$

$$\tan \psi = \sqrt{3} |\hat{\mathbf{T}}^*|, \quad (\text{A.23})$$

$$\cos 3\theta = -\sqrt{6} \frac{\text{tr}(\hat{\mathbf{T}}^* \cdot \hat{\mathbf{T}}^* \cdot \hat{\mathbf{T}}^*)}{[\text{tr}(\hat{\mathbf{T}}^* \cdot \hat{\mathbf{T}}^*)]^{3/2}}, \quad (\text{A.24})$$

$$f_d = \left(\frac{e - e_d}{e_c - e_d} \right)^\alpha, \quad (\text{A.25})$$

Material	φ_c [°]	h_s [MPa]	n [-]	e_{d0} [-]	e_{c0} [-]	e_{i0} [-]	α [-]	β [-]
Aubram's experiment sand	31.5	76500	0.29	0.48	0.78	0.9	0.13	1
Hostun sand	33.8	1000	0.29	0.61	0.91	1.09	0.13	2

Table A.3: Calibration of hypoplastic material model after von Wolffersdorff (1996) for model test sand in Aubram's experiments [2] and Hostun sand

$$f_b f_e = \frac{h_s}{n} \left(\frac{1+e_i}{e_i} \right) \cdot \left(\frac{e_{i0}}{e_{c0}} \right)^\beta \cdot \left(\frac{e_c}{e} \right)^\beta \cdot \left(-\frac{\text{tr} \mathbf{T}}{h_s} \right)^{1-n} \cdot \left[3+a^2 - \sqrt{3}a \left(\frac{e_{i0}-e_{d0}}{e_{c0}-e_{d0}} \right)^\alpha \right]^{-1}, \quad (\text{A.26})$$

$$\frac{e_i}{e_{i0}} = \frac{e_c}{e_{c0}} = \frac{e_d}{e_{d0}} = \exp \left[- \left(\frac{-\text{tr} \mathbf{T}}{h_s} \right)^n \right]. \quad (\text{A.27})$$

where,

e_i : the loosest void ratio by isotropic compression (pressure dependent)

e_c : critical state void ratio (pressure dependent)

e_d : void ratio at maximum densification (pressure dependent)

A.2.4 An improved version of barodesy for clay, Medicus and Fellin (2017)

$$\dot{\mathbf{T}} = c_3 |\mathbf{T}|^{c_4} \cdot (f \mathbf{R}^0 + g \mathbf{T}^0) \cdot |\mathbf{D}|, \quad (\text{A.28})$$

$$\mathbf{R} = -\exp(\alpha \mathbf{D}^0), \quad (\text{A.29})$$

$$\alpha = \frac{\ln K}{\sqrt{3/2 - \text{tr} \mathbf{D}^0^2/2}}, \quad (\text{A.30})$$

$$K = 1 - \frac{1}{1 + c_1(m - c_2)^2}, \quad (\text{A.31})$$

$$m = \frac{-3 \text{tr} \mathbf{D}^0}{\sqrt{6 - 2 \text{tr} \mathbf{D}^0^2}}, \quad (\text{A.32})$$

$$f = c_6 \cdot \beta \cdot \text{tr} \mathbf{D}^0 - \frac{1}{2}, \quad (\text{A.33})$$

$$g = (1 - c_6) \cdot \beta \cdot \text{tr} \mathbf{D}^0 + \left(\frac{1+e}{1+e_c} \right)^{c_5} - \frac{1}{2}, \quad (\text{A.34})$$

$$e_c = \exp \left(N - \lambda^* \ln \frac{2p}{\sigma^*} \right) - 1, \quad (\text{A.35})$$

$$\beta = -\frac{1}{c_3 \Lambda} + \frac{1}{\sqrt{3}} 2^{c_5 \lambda^*} - \frac{1}{\sqrt{3}}, \quad (\text{A.36})$$

$$\Lambda = -\frac{\lambda^* - \kappa^*}{2\sqrt{3}} \text{tr} \mathbf{D}^0 + \frac{\lambda^* + \kappa^*}{2}. \quad (\text{A.37})$$

c_1	c_2	c_3	c_4	c_5	c_6
0.028	-3.6213	-356.408	1	3.69	0.704

Table A.4: Determination of the constants for Dresden clay with $\varphi_c = 35^\circ$, $N = 0.622$, $\lambda^* = 0.038$ and $\kappa^* = 0.008$, Medicus and Fellin (2017) for Dresden clay

B Unsuccessful attempts

Simulation of the cone penetration was one of the main goals of this study, however, this goal could not be achieved as desired. Meshfree methods are young and still need a lot of trial and error until they are fully developed. SPARC also as one of the youngest meshfree methods, is not an exception. Although the process was despairing, the main supervisor and the author did not surrender and persistently sought for solutions. The attempts did not always work, nevertheless, we believe publishing them in the scope of this study is of importance for further investigations as it can possibly help to avoid these attempts. The attempts can be divided in two categories, the first category consists of general modification of procedure of SPARC. Meanwhile, the second category consists of methods suggested specifically for the problem of cone penetration (e.g. defining different boundary conditions for the penetrating cone), as discussed and explained in Chp. 4. Among the first group of attempts, some are explained in the following sections.

B.1 Axisymmetric SPARC

Since cone penetration test is a problem with axisymmetric conditions, cylindrical coordinates had to be implemented.

B.1.1 Cylindrical coordinates

In cylindrical orthogonal coordinates, the Cartesian coordinates (x, y, z) are mapped into (r, ϑ, z) through the relations:

$$x = r \cos \vartheta, y = r \sin \vartheta, z = z,$$

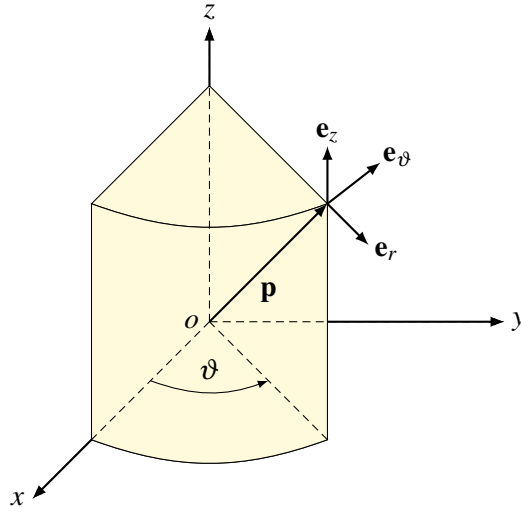
and in case of axisymmetry, where $\frac{\partial}{\partial \vartheta} = 0$, the position vector reads,

$$\mathbf{p} = r \mathbf{e}_r + z \mathbf{e}_z, \tag{B.1}$$

where $\hat{\mathbf{e}}_r$ and $\hat{\mathbf{e}}_z$ are the unit vectors in the direction of increasing r and z , respectively (see Fig. B.1).

Since for the problem of cone penetration can be assumed that the angular velocities (v_ϑ) are equal to zero, the velocity vector can be defined as,

$$\mathbf{v} = v_r \mathbf{e}_r + v_z \mathbf{e}_z. \tag{B.2}$$

Figure B.1: Vector \mathbf{p} in cylindrical coordinates $r\vartheta z$

B.1.2 Velocity gradient

Since we assume that $v_\vartheta = 0$, the velocity gradient can be simplified as,

$$\nabla \mathbf{v} = \begin{bmatrix} \frac{\partial v_r}{\partial r} & 0 & \frac{\partial v_r}{\partial z} \\ 0 & \frac{v_r}{r} & 0 \\ \frac{\partial v_z}{\partial r} & 0 & \frac{\partial v_z}{\partial z} \end{bmatrix}. \quad (\text{B.3})$$

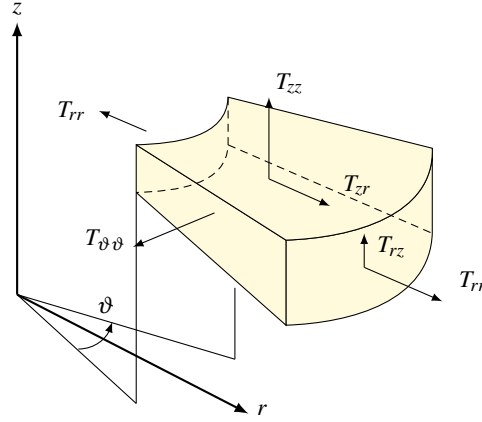
However Eq. B.3 needs to be further considered for particles lying on the symmetry line, since the radial velocity vanishes for these particles and on the other hand for the symmetry line is $r = 0$. Therefore, the component $\nabla \mathbf{v}(2,2)$ of particles lying on the symmetry line is unknown,

$$\text{For } r = 0 \rightsquigarrow \nabla \mathbf{v}(2,2) = \frac{v_r}{r} = \frac{0}{0}.$$

By assuming that the spatial derivative of radial velocities with respect to r vanishes at $r = 0$ and applying the L'Hôpital's rule, we obtain,

$$\lim_{r \rightarrow 0} \frac{v_r}{r} = \frac{\partial v_r}{\partial r} = 0,$$

for particles lying on the symmetry line.

Figure B.2: Stress tensor \mathbf{T} in cylindrical coordinates

B.1.3 Stress tensor and Cauchy equation

The stress tensor \mathbf{T} has the following form in cylindrical coordinate. For the interpretation of each stress component, see Fig. B.2.

$$\mathbf{T} = \begin{bmatrix} T_{rr} & 0 & T_{rz} \\ 0 & T_{\vartheta\vartheta} & 0 \\ T_{zr} & 0 & T_{zz} \end{bmatrix}. \quad (\text{B.4})$$

The Cauchy equation of motion (Eq. 1.1) has the following form in cylindrical coordinate,

$$\frac{\partial T_{rr}}{\partial r} + \frac{\partial T_{zr}}{\partial z} + \frac{1}{r}(T_{rr} - T_{\vartheta\vartheta}) = 0, \quad (\text{B.5})$$

$$\frac{\partial T_{rz}}{\partial r} + \frac{\partial T_{zz}}{\partial z} + \frac{1}{r}T_{rz} + \rho b_z = 0. \quad (\text{B.6})$$

The third term in the Eq. B.5 for particles on the symmetry line ($r = 0$) also needs to be further considered. It is assumed that at the beginning of the simulation $T_{rr} = T_{\vartheta\vartheta}$, therefore,

$$\frac{1}{r}(T_{rr} - T_{\vartheta\vartheta}) = \frac{0}{0}.$$

Again by applying the L'Hôpital's rule, we obtain,

$$\lim_{r \rightarrow 0} \frac{1}{r}(T_{rr} - T_{\vartheta\vartheta}) = \frac{\partial T_{rr}}{\partial r} - \frac{\partial T_{\vartheta\vartheta}}{\partial r} = 0.$$

The condition of $T_{rr} = T_{\vartheta\vartheta}$ holds not only for the first step but also for the rest of the simulations, since for particles on the symmetry line $\nabla \mathbf{v}(1,1) = \nabla \mathbf{v}(2,2) = 0$, which means that for these particles throughout the simulation T_{rr} is equal to $T_{\vartheta\vartheta}$.

The same consideration for particles on the symmetry line is also required for the third term in Eq. B.6. On the symmetry line the shear stresses are equal to zero, therefore,

$$\frac{1}{r}T_{rz} = \frac{0}{0}.$$

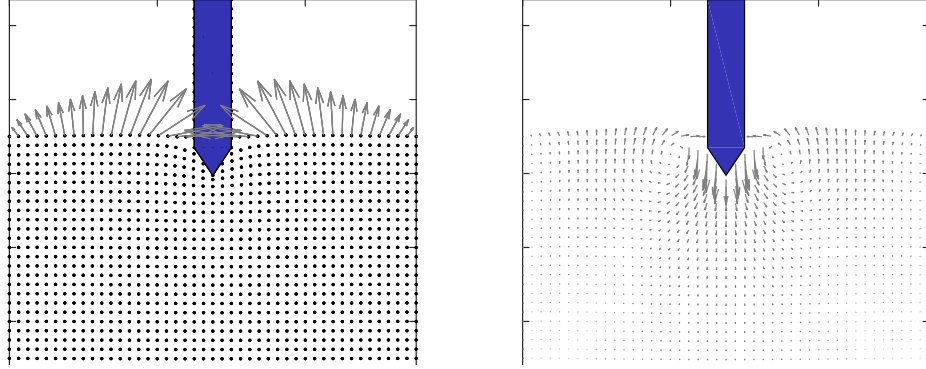


Figure B.3: Determination of velocities on the surface in the first sub-step (left), determination of velocities for field particles in the second sub-step (right)

By means of L'Hôpital's rule, we have

$$\lim_{r \rightarrow 0} \frac{1}{r} T_{rz} = \frac{\partial T_{rz}}{\partial r} = 0.$$

B.1.4 Failure

The obtained velocity field for simulations in axisymmetric condition was not sensible and the oscillations were stronger in comparison to 2D simulations. Furthermore, the particles on the symmetry line in axisymmetric condition are free to move *only* in the vertical direction. Therefore, the outward movement of the symmetry particles cannot be simply simulated. One attempt to deal with this problem was to free the "nearest particle to the tip of the cone" in the radial direction when the tip of the cone comes to the vicinity of the particle. However, after the particle was freed in the radial direction, the Newton solver could not find a solution and the simulation broke.

B.2 Predetermined velocities on the surface

The free boundary surface seemed to be the first volunteer for the problems associated with the simulation of cone penetration. As Chen also mentions in [11], the free boundary condition could be one of the reasons, why the simulation of the "zig-zag" test did not work.

In the procedure of SPARC as explained in Sec. 1.5, the equilibrium equations (Eq. 1.1) for field particles are *simultaneously* solved with the prescribed pressure (traction) boundary condition (Eq. 1.2).

In the proposed method, the velocities of particles are determined in each time step, in *two* "sub-steps". In the first sub-step, the prescribed pressure (traction) boundary condition for particles lying on the surface of the model is solved and the velocities of the particles on the surface are determined (see Fig. B.3-left). In the second sub-step, the velocities of the field particles are determined, while the velocities on the surface from the first sub-step are applied to the surface (see Fig. B.3).

B.2.1 Failure

This procedure did not offer any further advantages in comparison to the standard procedure of SPARC and the obtained relative depth for the simulation of the cone penetration was almost the same as that obtained with the standard procedure.

B.3 Static boundary condition through eigenvalues

In this attempt, the boundary tractions are defined through the eigenvalues of the stress tensor. The conventional procedure of SPARC as introduced in Sec. 1.5 is applied to update the stress tensor to time step $t + \Delta t$. However, instead of solving the boundary condition with prescribed traction in Eq. 1.2, the equilibrium equation (Eq. 1.1) with a modification of the stress state for surface particles is solved. The modification in the stress state is explained here,

- The three eigenvalues (T_1 , T_2 and T_3) of the stress tensor \mathbf{T}^{t+dt} are calculated,

$$\mathbf{T}^i = \begin{bmatrix} T_1 & 0 & 0 \\ 0 & T_2 & 0 \\ 0 & 0 & T_3 \end{bmatrix}.$$

- The first eigenvalue T_1 is set equal to the prescribed traction ($T_1 = p$),

$$\mathbf{T}^{ii} = \begin{bmatrix} p & 0 & 0 \\ 0 & T_2 & 0 \\ 0 & 0 & T_3 \end{bmatrix}.$$

- For the particle, the three orthogonal vectors are calculated as follows,

$$\mathbf{e}_n = \begin{pmatrix} n_1 \\ 0 \\ n_3 \end{pmatrix}, \quad \mathbf{e}_t = \begin{pmatrix} \sqrt{\frac{n_3^2}{n_1^2+n_3^2}} \\ 0 \\ -\frac{n_1\sqrt{\frac{n_3^2}{n_1^2+n_3^2}}}{n_3} \end{pmatrix}, \quad \mathbf{e}_x = \begin{pmatrix} 0 \\ \pm 1 \\ 0 \end{pmatrix},$$

and saved in \mathbf{Q} matrix, where \mathbf{e}_n is the unit normal of the surface and the two unknowns of \mathbf{e}_t are determined by considering the orthogonality of \mathbf{e}_t to \mathbf{e}_n and $|\mathbf{e}_t| = 1$. The vector \mathbf{e}_x remains constant, since the problem is considered in plane strain conditions,

$$\mathbf{Q} = \begin{pmatrix} n_1 & \sqrt{\frac{n_3^2}{n_1^2+n_3^2}} & 0 \\ 0 & 0 & \pm 1 \\ n_3 & -\frac{n_1\sqrt{\frac{n_3^2}{n_1^2+n_3^2}}}{n_3} & 0 \end{pmatrix}.$$

- The new stress state is acquired by rotating the stress tensor \mathbf{T}^{ii} to the Cartesian coordinates,

$$\mathbf{T}_{\text{new}}^{t+dt} = \mathbf{Q}\mathbf{T}^{ii}\mathbf{Q}^{-1}.$$

- $\mathbf{T}_{\text{new}}^{t+dt}$ is used to calculate the equilibrium equation (Eq. 1.1) for the particles which represent the static boundary.

B.3.1 Failure

The convergence of the solver was possible for a number of time steps. However, the oscillations of the obtained velocities on the surface were stronger in comparison to the standard procedure. Therefore, the simulation broke earlier before a noticeable relative depth was reached.

B.4 Rearrangement of particles

The idea is to create a regular arrays of particles (black particles in Fig. B.4). The field values ($\mathbf{v}, \mathbf{T}, e, \rho$) of the new particles are calculated by interpolating from the values of the old particles (the gray particles in Fig. B.4).

The newly created particles are located regularly *around* the pile/cone. The new regular distribution of particles was thought to give SPARC the advantage that in every time step, the particles will have sufficient and appropriate number of neighbors due to the regular distribution and thus the interpolation quality should be improved.

However, the creation of a regular array of particles is only possible if we neglect the deformation of the surface of the model and replace the deformed surface with a horizontal line which e.g. corresponds to the initial height (h_0) of the model at time step $t = 0$.

In the following this procedure is explained in details,

1. At time step t , all the field values ($\mathbf{v}^t, \mathbf{T}^t, e^t, \rho^t$) and position \mathbf{x}^t are known for the current particles.
2. A new regular distribution of particles is created in accordance to the current location of the penetrating cone/foundation (the black particles in Fig. B.4).
These new regular particles are created *around* the pile and on the *initial* height of the model (h_0) and therefore the geometry of the deformed ground surface is replaced with a horizontal line.
3. The field values of the old particles are taken as input data for the interpolation of the field values of the newly created particles.
4. The interpolated field values are assigned to the new regular particles.
5. Neighbors for the new regular particles are searched.
6. Time step $t + \Delta t$ is calculated with the new particles.
7. This procedure could be repeated at every time step.

B.4.1 Failure

The suggested attempt did not offer any particular advantage in comparison to the standard procedure and the obtained relative depth was almost the same as the one obtained by the standard procedure. Furthermore, the obtained solution (velocities) was not smoother as opposed to the one obtained without the rearrangement of particles.

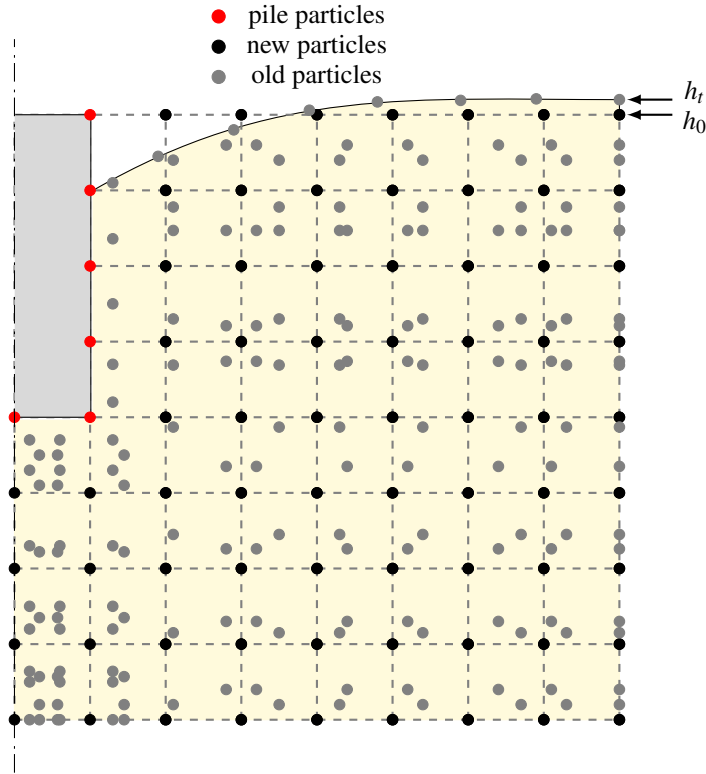


Figure B.4: Rearrangement of particles, black particles are the new regular particles, gray particles are the old particles with irregular distribution and the red particles represent the current location of the cone at time step t

B.5 Regular arrays of interpolation points

In order to improve the quality of interpolation, the following procedure was investigated. Let us assume that at time step t , the spatial derivative of the field value q at particle p (the blue particle in Fig. B.5) is required. q could be a component of velocity field or a component of the stress tensor.

$$\left(\frac{\partial q}{\partial x}\right)_p = ?$$

In the current framework of SPARC, the neighbors of particle P which lie in a fixed circle with radius r are searched and the spatial derivatives are calculated by means of the neighboring particles.

In the suggested procedure, firstly, a set of well-ordered *interpolation points* are created on the circumference of a circle with radius r around particle P (the red points in Fig. B.5). The particle P itself is also one of the interpolation points.

In the next step, the values of neighboring particles (the green particles in Fig. B.5) are used to interpolate the field value q for each interpolation point.

Finally, $\left(\frac{\partial q}{\partial x}\right)_p$ is approximated by means of the well-ordered interpolation points. This procedure was expected to give the advantage to SPARC that for the approximation of

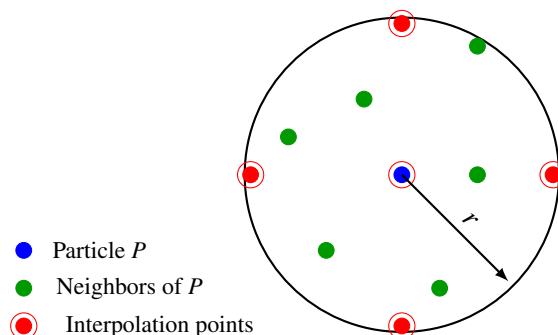


Figure B.5: Demonstration of soft particles and interpolation points

spatial derivatives, always a sufficient number of interpolation points, which are also appropriately located around particle P are available. One can consider applying this procedure only to an area of the continuum where the deformations are large so as to reduce the calculation time.

B.5.1 Failure

The Newton solver could not converge even for the first time step and the norm of the error became too large after the first and the second iteration of the Newton solver.

B.6 Exclusion of boundary particles

In the investigations with adherent boundaries (for walls or the penetrating cone), it was observed that the stress state, void ratio and density of boundary particles reached unreasonable values (see Sec. 4.5.6). For example, the norm of stress tensor for particles adherent to the shaft of the cone reached values 15000 times larger than the initial norm of stress tensor and the void ratio became negative. In the first place, such results prove that adherent boundaries are not appropriate for simulation of large deformations. Furthermore, adherent boundary conditions do not correspond to reality, so that a particle which represents the soil body sticks to the cone and experiences the same displacements like the cone. On the other hand, implementing smooth kinematic boundaries for the cone is not an easy task.

The suggested attempt was to define two groups of neighboring particles. The first group of neighbors, which include adherent boundary particles (see Fig. B.6 - left), are used for interpolation of velocity gradient at particle P . The second group of neighboring particles do not include adherent boundary particles and is used for interpolation of the divergence of stress (see Fig. B.6-right) at particle P . Consequently, the influence of unreasonably large or small values of stress state in the interpolation of the divergence of the stress could be avoided.

B.6.1 Failure

The problem with this idea is that a larger support size needs to be chosen so as to assure that an adequate number of neighbors are available for interpolation of gradient of stress.

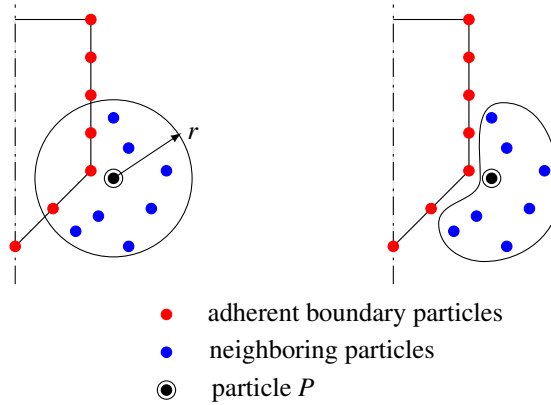


Figure B.6: Left: neighbors for interpolation of velocity gradient - Right: neighbors for interpolation of divergence of stress

However, as it is shown in Sec. 1.9.6, the quality and accuracy of interpolation worsens with increasing support size (r) and consequently the acquired solution (velocities) were not smooth and the simulation broke after a few time steps.

B.7 Convective acceleration

One of the main challenges throughout this study was to deal with oscillations in the obtained solution (e.g. see Fig. B.7-left). Oscillations in the velocities are also reported by Chen [11] for the simulation of "zig-zag" test. SPARC is not the only meshfree method that suffers from oscillations, as it is shown and discussed in I. Michel, I. Bathaeian et al.[38], the meshfree Finite Pointset Method (FPM), whose results are compared with the results of SPARC, has problems with oscillations. Unfortunately, the main cause of oscillations in SPARC is not known to the author. However, it is assumed that the oscillations of velocities can be a culprit that the solver can find no solution or cannot find the right solution after some time steps. Therefore, in order to avoid the oscillations, the convective acceleration was implemented in SPARC with a numerical density ρ_n which can be either chosen equal to the real density of the soil ρ or have a different value. ρ_n can be so long varied until the solver converges. However, it is important to mention that the initial stress state is not calculated with ρ_n and it does not influence the stress state in soil.

The equilibrium equation of motion with consideration of the convective acceleration for a 2D problem reads¹,

$$\frac{\partial T_{yy}}{\partial y} + \frac{\partial T_{yz}}{\partial z} = \rho_n \left(v_y \frac{\partial v_y}{\partial y} + v_z \frac{\partial v_y}{\partial z} \right), \quad (\text{B.7})$$

$$\frac{\partial T_{zy}}{\partial y} + \frac{\partial T_{zz}}{\partial z} + \rho g = \rho_n \left(v_y \frac{\partial v_z}{\partial y} + v_z \frac{\partial v_z}{\partial z} \right). \quad (\text{B.8})$$

¹The problem is considered to be quasi-static and therefore the term $\frac{\partial v}{\partial t}$ is negligible.

B.7.1 Failure and success

The convective acceleration did not prove to help with the simulation of cone penetration and punching. Nevertheless, for the simulation of simple shear test (see Sec. 5.6), implementation of the convective term was helpful. Simulation of simple shear without the convective acceleration was not possible and the Newton solver failed after some time steps.

B.8 Explicit solver

The explicit method was implemented in SPARC for the determination of the unknown velocities at time step $t + \Delta t$. It was intended to be applied either to the whole process of simulation or to be used as an alternative when the Newton solver is not capable of finding a solution.

The *unknown* velocities are set to zero or the solution from the former time step t is used as an initial guess. The *known* velocities on the kinematic boundaries are applied. For each particle, the residuum of governing equations for each degree of freedom (unknown velocities) is calculated and stored in the vector \mathbf{r} . The vector \mathbf{r} contains the residua of governing equations, (\mathbf{r}_1 , \mathbf{r}_2 and r_3) as shown in Fig. 1.7.

If the norm of \mathbf{r} does not fulfill the prescribed tolerance, the unknown velocities will be updated. For this purpose the acceleration of each particle in the y - and z -directions is calculated with Eq. B.9,

$$\mathbf{b} = \frac{\nabla \cdot \mathbf{T}}{\rho} + \mathbf{g}. \quad (\text{B.9})$$

Next the velocities are updated,

$$\mathbf{v}^{t+\Delta t} = \mathbf{v}^t + \mathbf{b} \cdot \Delta t, \quad (\text{B.10})$$

and the densities are also updated with Eq. 1.10 calculated with the update velocities $\mathbf{v}^{t+\Delta t}$. The norm of the residua (\mathbf{r}) is calculated again with the updated velocities ($\mathbf{v}^{t+\Delta t}$) and compared with the prescribed tolerance.

The above procedure is repeated as long as the norm of the residua of the governing equations, $|\mathbf{r}|$, is smaller than the tolerance, which means that the accelerations have vanished and the particles are in quasi-static state.

B.8.1 Fourth-order Runge-Kutta integration

In order to get a more precise estimation of the acceleration, the fourth-order Runge-Kutta integration, according to Butcher [10], was implemented,

$$\mathbf{v}^{t+\Delta t} = \mathbf{v}^t + \mathbf{b} \cdot \Delta t, \quad (\text{B.11})$$

with \mathbf{b} ,

$$\mathbf{b} = \frac{\mathbf{b}_1 + 2\mathbf{b}_2 + 2\mathbf{b}_3 + \mathbf{b}_4}{6},$$

where,

$$\mathbf{b}_1 = f(t, \mathbf{v}^t), \quad (\text{B.12})$$

$$\mathbf{b}_2 = f\left(t + \frac{\Delta t}{2}, \mathbf{v}^t + \mathbf{b}_1 \frac{\Delta t}{2}\right), \quad (\text{B.13})$$

$$\mathbf{b}_3 = f\left(t + \frac{\Delta t}{2}, \mathbf{v}^t + \mathbf{b}_2 \frac{\Delta t}{2}\right), \quad (\text{B.14})$$

$$\mathbf{b}_4 = f\left(t + \Delta t, \mathbf{v}^t + \mathbf{b}_3 \Delta t\right). \quad (\text{B.15})$$

B.8.2 Failure

The explicit solver was implemented for simulation of an oedometer test and the obtained solution showed stronger oscillations in comparison to the standard procedure of SPARC. Besides, the explicit solver needs far more computing time.

B.9 Moving average smoothing

In SPARC, the solution from time step t is used as the first guess of the Newton solver for time step $t + \Delta t$. The solution delivered at time step t is not always smooth, especially after the deformations have become large. In an attempt to improve the first guess for the following time step, a moving average smoothing was implemented in SPARC, by which the smoothed value of each particle is the mean value of this particle and its neighboring particles. If particle i has b_i neighbors, then the field variables are smoothed as follows,

$$\mathbf{v}_i \Leftarrow \frac{1}{b_i} \sum_{j=1}^{b_i} \mathbf{v}_j, \quad (\text{B.16})$$

$$\mathbf{T}_i \Leftarrow \frac{1}{b_i} \sum_{j=1}^{b_i} \mathbf{T}_j, \quad (\text{B.17})$$

$$e_i \Leftarrow \frac{1}{b_i} \sum_{j=1}^{b_i} e_j, \quad (\text{B.18})$$

$$\rho_i \Leftarrow \frac{1}{b_i} \sum_{j=1}^{b_i} \rho_j. \quad (\text{B.19})$$

B.9.1 Failure

This attempt did not prove to be efficient and the Newton solver could not converge with the smoothed solution from the former time step. However, the smoothing method is applied in preparing the figures and final results in this study. In Fig. B.7 the velocity field for simulation of the settlement of shallow foundations into sand before and after application of the moving average smoothing method is compared.

B.10 Smoothing the spatial derivatives

In another attempt to avoid the oscillations in the obtained solution, the moving average smoothing method, introduced in Sec. B.9, was directly applied to the spatial derivatives of velocity field and stress tensor.

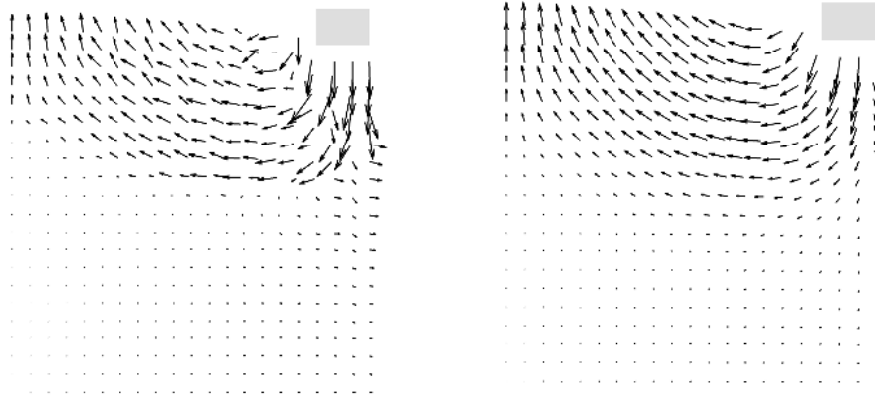


Figure B.7: Left: velocity field without application of moving average smoothing (oscillations in the velocities are apparent)-right: velocity field after application of moving average smoothing

B.10.1 Failure

The convergence of the Newton solver was not possible and the norm of the error became too large after the first or the second iteration of the solver.

Bibliography

- [1] Sara Abedi, Amy L. Rechenmacher, and Andrés D. Orlando. Vortex formation and dissolution in sheared sands. *Granular Matter*, 14(6):695–705, 2012.
- [2] D. Aubram. *An Arbitrary Lagrangian-Eulerian Method for Penetration into Sand at Finite Deformation*. PhD thesis, Technische Universität Berlin, 2013.
- [3] D. Aubram. Development and experimental validation of an arbitrary lagrangian-eulerian (ALE) method for soil mechanics. *geotechnik*, 38(3):193–204, 2015. ISSN 2190-6653. doi: 10.1002/gete.201400030. URL <http://dx.doi.org/10.1002/gete.201400030>.
- [4] G. Bellotti Baldi, R. Ghionna, and V. Jamiolkowski. Interpretation of CPTs and CPTUs; 2nd part: Drained penetration of sands. In *Proceedings of the 4th International Geotechnical Seminar*, pages 143–156, 1986.
- [5] M. M. Baligh. Undrained deep penetration, i: shear stresses. *Geotechnique*, 36(4): 471–485, 1986.
- [6] Mohsen M Baligh. Strain path method. *Journal of Geotechnical Engineering*, 111 (9):1108–1136, 1985.
- [7] Erich Bauer. Calibration of a comprehensive hypoplastic model for granular materials. *Soils and Foundations*, 1996.
- [8] M. Bolton, M.W. Gui, J. Garnier, J.F. Corte, G. Bagge, J. Laue, and R Renzi. Centrifuge cone penetration tests in sand. *Géotechnique, London*, 49(4), 1999.
- [9] M. Budhu. *Soil Mechanics & Foundations*. John Wiley & Sons, INC, University of Arizona, 2000.
- [10] John Charles Butcher. A history of Runge-Kutta methods. *Applied numerical mathematics*, 20(3):247–260, 1996.
- [11] Chien-Hsun Chen. *Development of Soft Particle Code (SPARC)*, volume 21. Advances in Geotechnical Engineering and Tunnelling, Logos Verlag Berlin GmbH, 2015.
- [12] R. Cudmani. *Statische, alternierende und dynamische Penetration in nichtbindigen Böden*. PhD thesis, Karlsruhe, Institute für Bodenmechanik und Felsmechanik, 2001.
- [13] H. Turan Durgunoglu and James K. Mitchell. Static penetration resistance of soils. Prepared for NASA headquarters, University of California, Berkeley, 1973.
- [14] Wolfgang Fellin. Extension to barodesy to model void ratio and stress dependency of the K_0 value. *Acta Geotechnica*, 2013.
- [15] V. Fioravante, M. Jamiolkowski, F. Tanizawa, and F. Tatsuoka. Results of CPTs in Toyoura quartz sand. In *Proceedings of the 1st International Symposium on Calibration Chamber Testing (ISOCCT-1)*, Potsdam, New York, Elsevier, pages 135–146, 1991.

- [16] S. K. Ghosh. Experimental tests of buckling folds in relation to strain ellipsoid in simple shear deformations. *Tectonophysics*, 3(3):169–185, 1966.
- [17] John D Godfrey. The origin of ptygmatic structures. *The Journal of Geology*, 62(4):375–387, 1954.
- [18] M. Goldscheider. *Spannungen in Sand bei Räumlicher Monotoner Verformung*. PhD thesis, Karlsruhe, 1972.
- [19] G. Gudehus. A comprehensive constitutive equation for granular materials. *Soils and Foundations*, 36(1):1–12, March 1996. Japanese Geotechnical Society.
- [20] Chunhua Han and Andrew Drescher. Shear bands in biaxial tests on dry coarse sand. *Soils and Foundations, Japanes Society of Soil Mechanics and Foundation Engineering*, 33(1):118–132, 1993.
- [21] Wolfgang F. Heinz. *Zur Tragfähigkeit von Flachgründungen auf rolligem Boden*. PhD thesis, 1970.
- [22] I. Herle and G. Gudehus. Determination of parameters of a hypoplastic constitutive model from properties of grain assemblies. *Mechanics of Cohesive-frictional Materials*, 4(5):461–486, 1999.
- [23] GT Houlsby and R Hitchman. Calibration chamber tests of a cone penetrometer in sand. *Géotechnique*, 38(1):39–44, 1988.
- [24] P. A. Vermeer J. Derues, B. Zweschper. *Database for Tests on Hostun RF Sand*. Institute of Geotechnical Engineering, University of Stuttgart, 2000.
- [25] D. Kolymbas. Barodesy: a new hypoplastic approach. *International Journal for Numerical and Analytical Methods in Geomechanics*, 36(9):1220–1240, May 2011.
- [26] D. Kolymbas. Barodesy: a new constitutive frame for soils. *Géotechnique Letters*, 2:17–23, April 2012.
- [27] D. Kolymbas. *Barodesy: the next generation of hypoplastic constitutive models for soils*, chapter 2, pages 43–56. Springer, February 2014.
- [28] D. Kolymbas. Introduction to barodesy. *Géotechnique*, 65(1):52–65, 2015.
- [29] Dimitrios Kolymbas. *Geotechnik*. Springer, 2011.
- [30] Dimitrios Kolymbas. Barodesy as a novel hypoplastic constitutive theory based on the asymptotic behaviour of sand. *Geotechnik*, March 2012.
- [31] Dimitrios Kolymbas. *Geotechnik: bodenmechanik, grundbau und tunnelbau*. Springer-Verlag, 2017.
- [32] Jan Kozicki, Maciej Niedostatkiewicz, J. Tejchman, and H-B Muhlhaus. Discrete modelling results of a direct shear test for granular materials versus FE results. *Granular Matter*, 15(5):607–627, 2013.
- [33] G.A. Leonards, editor. *Foundation Engineering*. McGraw-Hill Book Company, INC, 1962.
- [34] G. R. Liu, Y. Li, K. Y. Dai, M. T. Luan, and W. Xue. A linearly conforming radial point interpolation method for solid mechanics problems. *International Journal of Computational Methods*, 03(04):401–428, 2006. doi: 10.1142/S0219876206001132. URL <http://www.worldscientific.com/doi/abs/10.1142/S0219876206001132>.
- [35] Lawrence E. Malvern. *Introduction to the Mechanics of Continous Media*. Prentice-Hall, 1969.
- [36] Gertraud Medicus. *Barodesy and its Application for Clay*. Advantages in Geotechnical and Tunnelling, 21. Logos Verlag Berlin, 2015.

- [37] Gertraud Medicus and Wolfgang Fellin. An improved version of barodesy for clay. *Acta Geotechnica*, 12(2):365–376, 2017.
- [38] I. Michel, S. M. I. Bathaeian, J. Kuhnert, D. Kolymbas, C.-H. Chen, I. Polymerou, C. Vrettos, and A. Becker. Meshfree generalized finite difference methods in soil mechanics—part ii: numerical results. *GEM - International Journal on Geomathematics*, 8(2):191–217, Nov 2017. ISSN 1869-2680. doi: 10.1007/s13137-017-0096-5. URL <https://doi.org/10.1007/s13137-017-0096-5>.
- [39] A. Niemunis and I. Herle. Hypoplastic model for cohesionless soils with elastic strain range. *Mechanics of Cohesive-Frictional Materials*, 2:279–299, October 1997.
- [40] J. O’Donovan, C. O’Sullivan, and G. Marketos. Two-dimensional discrete element modelling of bender element tests on an idealised granular material. *Granular Matter*, 14(6):733–747, 2012.
- [41] I. Ostermann, J. Kuhnert, D. Kolymbas, C-H. Chen, I. Polymerou, V. Šmilauer, C. Vrettos, and D. Chen. Meshfree generalized finite difference methods in soil mechanics—part i: theory. *GEM-International Journal on Geomathematics*, 4(2): 167–184, 2013.
- [42] Iliana Polymerou. *Untersuchung großer Verformungen in der Vertushka*, volume 22. Advances in Geotechnical Engineering and Tunnelling, Logos Verlag Berlin GmbH, 2017.
- [43] Farhang Radjai and Stéphane Roux. Turbulentlike fluctuations in quasistatic flow of granular media. *Phys. Rev. Lett.*, 89, Jul 2002. doi: 10.1103/PhysRevLett.89.064302.
- [44] A. F. Revuzhenko. Odnorodnaya deformatsiya splochnoy sredy. *Prikladnaya Mekhanika i tekhnicheskaya Fysika*, 38(3), 1997.
- [45] V. Richefeu, G. Combe, and G. Viggiani. An experimental assessment of displacement fluctuations in a 2D granular material subjected to shear. *Géotechnique Letters*, 2(3):113–118, 2012. doi: 10.1680/geolett.12.00029. URL <https://doi.org/10.1680/geolett.12.00029>.
- [46] Rodrigo Salgado. *Analysis of penetration resistance in sands*. University of California, Berkeley, 1993.
- [47] Barbara Schneider-Muntau, Chien-Hsun Chen, and S. M. Iman Bathaeian. Simulation of shear bands with Soft PARTICle Code (SPARC) and FE. *GEM - International Journal on Geomathematics*, 8(1):135–151, Apr 2017. ISSN 1869-2680. doi: 10.1007/s13137-016-0091-2. URL <https://doi.org/10.1007/s13137-016-0091-2>.
- [48] Endra Susila and Roman D Hryciw. Large displacement FEM modelling of the cone penetration test (CPT) in normally consolidated sand. *International Journal for Numerical and Analytical Methods in Geomechanics*, 27(7):585–602, 2003.
- [49] Cee-Ing Teh. *An analytical study of the cone penetration test*. PhD thesis, University of Oxford, Hertford College, 1987.
- [50] J. Tejchman and E. Bauer. Numerical simulation of shear band formation with a polar hypoplastic constitutive model. *Computers and Geotechnics*, 19(3):221–244, 1996.
- [51] J. Tejchman and W. Wu. Numerical simulation of shear band formation with a hypoplastic constitutive model. *Computers and Geotechnics*, 18(1):71–84, 1996.

- [52] Karl Terzaghi and Ralph B Peck. *Die Bodenmechanik in der Baupraxis*. Springer-Verlag, 1961.
- [53] C. Thornton and L. Zhang. A numerical examination of shear banding and simple shear non-coaxial flow rules. *Philosophical Magazine*, 86(21-22):3425–3452, 2006.
- [54] Antoinette Tordesillas, Sebastian Pucilowski, David M. Walker, John F. Peters, and Laura E. Walizer. Micromechanics of vortices in granular media: connection to shear bands and implications for continuum modelling of failure in geomaterials. *International Journal for Numerical and Analytical Methods in Geomechanics*, 38(12):1247–1275, 2014.
- [55] Clifford Truesdell. *The kinematics of vorticity*. Indiana University Press Bloomington, 1954.
- [56] Peter van den Berg, Rene de Borst, and Han Huetink. An Eulerean finite element model for penetration in layered soil. *International Journal for Numerical and Analytical Methods in Geomechanics*, 20(12):865–886, 1996. URL <http://doc.utwente.nl/71291/>.
- [57] P. A. Vermeer. The orientation of shear bands in biaxial tests. *Geotechnique*, 40(2): 223–236, 1990.
- [58] P.-A. von Wolffersdorff. A hypoplastic relation for granular materials with a predefined limit state surface. *Mechanics of Cohesive-Frictional Materials*, 1:251–271, March 1996.
- [59] Jianfeng Wang and Budi Zhao. Discrete-continuum analysis of monotonic pile penetration in crushable sands. *Canadian Geotechnical Journal*, 51(10):1095–1110, 2014.
- [60] D. J. White and M. D. Bolton. Displacement and strain paths during plane-strain model pile installation in sand. *Géotechnique*, 54(6):375–397, 2004.
- [61] David John White. *Investigation into the behaviour of pressed-in piles*. PhD thesis, University of Cambridge, Churchill College, 2002.
- [62] H.S. Yu and G.T. Houlsby. Finite cavity expansion in dilatant soils: loading analysis. *Géotechnique*, 1991.
- [63] D. Zöhrer. *Laboratory Experiments and Numerical Modelling of Cone Penetration Tests into various Martian Soil Analogue Materials*. PhD thesis, Technische Universität Graz, Institut für Bodenmechanik und Grundbau, 2006.

Verpflichtungs- und Einverständniserklärung

Ich erkläre, dass ich meine Dissertation selbständig verfasst und alle in ihr verwendeten Unterlagen, Hilfsmittel und die zugrunde gelegte Literatur genannt habe.

Ich nehme zur Kenntnis, dass auch bei auszugsweiser Veröffentlichung meiner Dissertation die Universität, das/die Institut/e und der/die Arbeitsbereich/e, an dem/denen die Dissertation ausgearbeitet wurde, und die Betreuerin/nen bzw. der/die Betreuer zu nennen sind.

Ich nehme zur Kenntnis, dass meine Dissertation zur internen Dokumentation und Archivierung sowie zur Abgleichung mit der Plagiatssoftware elektronisch im Dateiformat pdf ohne Kennwortschutz bei der/dem Betreuer/in einzureichen ist, wobei auf die elektronisch archivierte Dissertation nur die/der Betreuerin/Betreuer der Dissertation und das studienrechtliche Organ Zugriff haben.

Innsbruck am

.....

Iman Bathaeian, MSc